Manipulation of Coherent Light and Coherent Light Manipulation of Atoms

By

Deepak Pandey

A thesis submitted to the Jawaharlal Nehru University
for the degree of Doctor of Philosophy

Department of Light And Matter Physics
Raman Research Institute
Bangalore 560 080
January 2016

© Deepak Pandey, 2016.

Typeset in LaTeX 2_ε.

Declaration:

I hereby declare that the work reported in this thesis is entirely original. This thesis is composed independently by me at Raman Research Institute under the supervision of Prof. Hema Ramachandran. I further declare that the subject matter presented in this thesis has not previously formed the basis for the award of any degree, diploma, membership, associateship, fellowship or any other similar title of any university or institution.

Prof. Hema Ramachandran

Deepak Pandey

Light And Matter Physics Group
Raman Research Institute
Bangalore 560 080
India

Certificate:

This is to certify that the thesis entitled **"Manipulation of Coherent Light and Coherent Light Manipulation of Atoms"** submitted by Deepak Pandey for the award of the degree of Doctor of Philosophy of Jawaharlal Nehru University is his original work. This has not been published or submitted to any other University for any other Degree or Diploma.

Prof. Ravi Subrahmanyan
(Centre Chairperson)
Director
Raman Research Institute
Bangalore 560 080
India

Prof. Hema Ramachandran
(Thesis Supervisor)

Acknowledgements

Firstly, I would like to thank my supervisor Hema Ramachandran for giving me the opportunity to work in the cold atom laboratory and also giving me complete independence in setting up a new cold atom experiment. I appreciate her encouragement and help during the difficult times in my thesis days.

I extend my heartfelt thanks to my senior Nandan Satpathy who has been a great friend and colleague, and an important source of all the information about the current trends in scientific world. His innovative analytic and critical thoughts were always a source of inspiration and a learning experience for me.

I thank Shafi for his great help during thesis writing and his ever positive attitude in the lab. His optimistic and enthusiastic nature was a driving force of my work. Surya who joined the lab during my final stages of Ph.D. has been an extremely helpful colleague.

I thank Meena for her always encouraging attitude and all her help regarding any issues related to electronics in the lab. She has helped me in many difficult times of my Ph.D. days without which I could have not finished my thesis so smoothly.

I thank Dhanalakshmi, Anup, Arun, Smitha, Shreekant, Jitender, Shahid and Sourish who have been a great help at various stages in the lab. I especially thank Dhanalakshmi for giving me important inputs during the beginning of my Ph.D. days and being a great friend throughout. I also thank all the other project students throughout the years for their help.

I thank Antoine Browaeys for hosting me for a few months in the University of Paris, Orsay, France and giving me the opportunity to work in his lab during which I learnt many things critical

for my experiment.

I thank Tridib and Arijit from the neighbouring lab for their help with various things during the course of my Ph.D. work and also being good friends.

I thank Solomon for providing valuable insights into the quantum optics theory during his tenure as a post doc in RRI. It also led to an interesting collaboration work with him and an important part of my thesis.

I thank Andal, Sadiq and Reji for their valuable comments regarding my thesis work and also for all the instruments that I borrowed from their lab.

I thank Sam, Supurna and Poonam for an interesting collaboration work which became a part of my thesis work.

I thank the people of the mechanical workshop and the Radio Astronomy lab for their help. I especially thank Girish for building the FPGA based correlation detection module.

I thank all the LAMP group staff especially Shivu and Manju for all their help.

I thank all the library staff for maintaining such a useful and good library over the years despite the growing age of electronic media. I have spent many peaceful hours in the library writing my thesis.

I thank the administrative, purchase, E & B, gardening, security, canteen and transportation staff of RRI for providing so many facilities which led to a smooth stay over the years

I thank the computer section for a lot of help over the years regarding various computing and hardware issues.

I thank all my friends at RRI especially Chaitra and Amrita for being good friends throughout.

Lastly, but of course not the least I thank my parents and my siblings for believing in me and for providing invaluable support and inspiration during all these years. It is due to them that I have completed my thesis today after overcoming many obstacles. Final thanks goes to Chandreyee for supporting me always in all my decisions.

List of Publications

I. Articles in journals/Unpublished eprints:

[1] Deepak Pandey, Nandan Satapathy, Meena M. S. and Hema Ramachandran.
Quantum walk of light in frequency space and its controlled dephasing.
Phys. Rev. A, **84**, 042322, 2011.

[2] Nandan Satapathy, Deepak Pandey, Poonam Mehta, Supurna Sinha, Joseph Samuel and Hema Ramachandran.
Classical light analogue of the nonlocal Aharonov-Bohm effect.
EPL, **97**, 50011, 2012.

[3] Nandan Satapathy, Deepak Pandey, Sourish Banerjee and Hema Ramachandran.
Optical phase noise engineering via acousto-optic interaction and its interferometric applications
JOSA A, **30**, 910, 2013.

[4] Deepak Pandey, Nandan Satapathy, Buti Suryabrahmam, J. Solomon Ivan and Hema Ramachandran.
Classical Light Sources with Tunable Temporal Coherence and Photon Number Distribution
arXiv:1210.1403.

Preface

The study of light and of light-matter interaction are two of the most fundamental topics of interest in science that have enriched our knowledge and understanding of the various phenomena in the universe. This understanding has led the generation of controlled quantum states both for light (photons) as well as for matter (atomic systems). The generation and manipulation of quantum states have become a vibrant topic of interest due to their promise towards quantum computation and quantum information processing. Generation of non-classical states of light has been realised in different systems [1]. One of the simpler methods is of generation of heralded single photon states in paramateric down conversion in a nonlinear crystal. Over the past few years the experimental techniques for photon addition and substraction on coherent and thermal light states have been demonstrated. This opens up the possibility of generating non-classical states with desired features. In the first part of this thesis, the manipulation of coherent light by acousto-optic interaction to generate classical state is demonstrated. This method for generating tunable classical light states with desired coherence properties and photon number distribution can be used in conjunction with photon addition techniques to generate tunable non-classical states. The polarization rotation of the classical incoherent light generated this way, over the polarization sphere (Poincare sphere), shows the geometric phase effects in a polarized Hanbury-Brown-Twiss (HBT) setup and can be used to modulate the bunching properties of light.

In atomic systems, single isolated particles have usually been the focus for the exploration of quantum features. The unprecedented control over the manipulation of the external as well as internal states of atomic systems have been possible only by coherent laser light. In this thesis, the coherent light manipulation of atoms is concerned towards single atom trapping in an optical

dipole trap. The basic requirement for this is the cold atom reservoir which is a magneto-optical-trap (MOT). Aiming towards the single atom trap and the study of the coherence properties of the photons emitted from the atom, a construction of MOT of ^{87}Rb, and the characterization of its different parameters are presented. A photon coincidence circuit is built for second order photon correlation measurement of the emitted light from the laser cooled and trapped atoms.

This thesis is divided into two parts:

1) Manipulation of coherent light.

2) Manipulation of atoms using coherent light.

The first two chapters of the thesis are related to part 1 and later two chapters to part 2. The chapter-wise break of the thesis is as follows

Chapter-1: Manipulation of Coherent Light

This chapter presents an interesting method of creating tunable classical states of the light by manipulation of the input coherent laser light. Acousto-optic interaction is used to modulate the phase and the intensity of the continuous coherent light to generate classical light states with predetermined photon number distributions and coherence properties. The efficacy of the method shown here is that, this can be used to generate any desired classical state, as an example a particular classical non-Gaussian state is generated here. Theoretical calculations are given to analyze the non-classical behaviour of single photon addition on the non-Gaussian classical state generated in the experiment.

Chapter-2: Classical Light Analogue of the non-local Aharnov-Bohm Effect

This chapter demonstrates an interesting analogue of the quantum mechanical multiparticle Aharnov-Bohm effect using classical phase incoherent light in a polarized Hanbury-Brown-Twiss interferometer [2]. The cyclic change in the polarization for a coherent light accumulates an additional phase due to the geometry of the path over the polarization sphere and is known as Pancharatnam's geometric phase. For the case of incoherent classical light, this additional phase acquired can be extracted in the second order cross correlation between the detectors of the HBT interferometer. A possible application of this effect, as a two photon wavefront deflector in a

phase gradient plate is proposed.

Further the cascaded version of these kind of polarized interferometer can be used to generate light with a zero delayed second order correlation value, $\mathcal{G}^2(0) > 2$ by only means of phase fluctuation. In a two stage cascaded interferometric system, modulation of $\mathcal{G}^2(0)$ is shown with a comparison between the experimental results and the theoretical predicted values.

Chapter-3: Coherent Light Manipulation of Atoms

This chapter describes the basic theoretical and experimental aspects of laser cooling and trapping techniques. The Magneto-Optical-Trap (MOT), which is a workhorse in the experiments with ultra-cold atoms, is built for ^{87}Rb aiming towards a single atom dipole trap.

A detailed description of the MOT that is constrcuted and the characterization of the cold ensemble of ^{87}Rb are presented. This involves the design of a vacuum chamber and its assembling to achieve an ultra-high vacuum, setting up the laser system with hyperfine resolving saturation absorption spectroscopy, and the optical alignment for MOT and detection system. The various parameters like the number of atoms, density, loading and decay rates, and temperature of the vapour loaded MOT are presented.

Chapter-4: Towards Single Atom dipole Trap and Photon Correlation Measurement

This chapter is divided into two parts. The first part of the chapter gives a brief literature survey about the single atom dipole trapping due to collisional blockade [3] mechanism followed by a description of the progress in the experiment towards single atom trapping and its detection until the writing of the thesis.

The second part of the chapter is related to the photon correlation measurement using a second order correlation function. The second order correlation function is an important parameter to study the coherence properties of the light sources, as important information about the light source can be obtained from this. Light states with non-classical characteristics can be identified in a coincidence measurement on two detectors of HBT interferometer. The anti-bunching behaviour of the light emitted from a single atom can also be observed in the HBT experiment. In this part of the chapter, a description of the photon coincidence unit that is designed and

built, is given. This FPGA (Field Programmable Gate Array) based coincidence detection unit is developed for photon correlation measurements and has a coincidence timing resolution of 5 ns.

Contents

1

Chapter 1

1.1 Manipulation of Coherent Light

Introduction

Understanding light-matter interactions and mechanisms of light generation are of vital importance in elucidating many physical processes. While for most processes, a combination of a statistical approach along with Maxwell's classical theory of electromagnetism suffices, several optical processes demand a quantum mechanical approach to the electromagnetic field [4–6]. The quantum theory of light makes a clear distinction between different sources of radiation such as coherent, thermal, and single photon sources [7]. Radiation from the former two sources may be explained classically, while light from the latter can only be explained quantum mechanically. In other words, the former two states are deemed classical, and the latter non-classical. Due to their quantum nature, non-classical sources of light display several counter-intuitive features evoking

considerable interest in them. Non-classical sources of light have been generated experimentally by several techniques [1] and their possible applications in different fields, especially quantum information, are well explored [8]. However, recent years have witnessed an emergence of interest in *classical* sources of light [2, 9–14]. These have been used in intriguing applications like ghost imaging [9–12], and interferometry based experiments as in Refs. [2, 13], and have also formed an ingredient in the creation of non-classical states of light [14–16].

In this chapter a method of creating tunable classical incoherent light sources by manipulating coherent continuous laser light is demonstrated and some of its possible applications in quantum optics are discussed. The tunable classical incoherent light generated this way can be tailored to mimic light from a thermal source or can be made to emit light with desired features. Utilizing the fact that an acousto-optic modulator (AOM) may be effectively used to introduce phase and intensity fluctuations to light rapidly and accurately [17–19], we create incoherent light having the desired coherence times and intensity statistics, or photon-number distributions, from the input coherent light.

The motivations for creating such sources are several. This technique offers an alternative to the current standard method of using a rotating ground glass plate [20, 21] to generate pseudo-thermal light. Further, the electronic control of fluctuations provides a robust and flexible procedure for producing tailored classical light sources with predetermined photon emission rates. Several interesting applications may be possible with this. For example, it is known that non-classical states can be generated by combining classical light, both coherent and thermal, with single photons (Fock state) in photon addition experiments [14]-[16] ,[22]-[23]. The ability to tailor classical states of light to have Gaussian or non-Gaussian state with tailored photon number distributions, as demonstrated in this chapter, can be used in photon addition experiments to generate the non-classical states of light with tailored characteristics. In addition, classical non-Gaussian states with tailored photon number distributions (PND) may, in turn, be used to produce states with tailored non-Gaussian entanglement. This is of importance in the quantum information theoretic context, where recent findings suggest non-Gaussian entanglement to be advantageous over Gaussian entanglement [24–26].

1.2 Theoretical Background

In this section a brief description of some fundamental concepts like light sources and the theory of optical coherence, quantum state representation of different type of light states, and some quantum mechanical operations on single photon states are presented.

1.2.1 Light sources and Coherence

A majority of light sources emit electromagnetic radiation due to de-excitation from an excited energy state (say E_i) to a lower energy state (say E_k) in a molecular or atomic system. The finite life time of the excited state (Γ) of the radiating atom, which is a consequence of Heisenberg uncertainty principle $\Delta E \Delta t \sim \hbar$, gives a Lorentzian line shape with a width (FWHM=Γ) around the central transition frequency $\omega_{ik} = \frac{E_i - E_k}{\hbar}$, in the frequency spectrum [27],

$$I = I_0 \; L(\omega - \omega_{ik}), \tag{1.1}$$

where

$$L(\omega - \omega_{ik}) = \frac{\Gamma^2}{[(\omega - \omega_{ik})^2 + \Gamma^2]} \tag{1.2}$$

This is known as natural broadening.

In a collection of many such radiators, the de-excitation process can be stimulated or spontaneous. Lasers are the examples where a coherent light with very narrow spectral bandwidth, is emitted by stimulated emission of radiation by a group of atoms or molecules, confined within a resonant cavity and radiating synchronously in a well ordered and highly dependent fashion. In contrast to lasers, there are another natural classes of light sources classified as thermal light or chaotic light sources where a large collection of atoms or molecules, excited to high energy states by thermal, electrical, or any another means, randomly and independently de-excites and results in chaotic radiation. Light from a high pressure gas discharge lamp, incandescent bulbs, and sun are the examples of a thermal light source. Thermal light has a broad frequency spectrum. There are two additional broadening mechanism which can be attributed for the large spectral width in thermal light sources.

1) Collisional Broadening:- The radiating atoms in a thermal light source, like a gas discharge lamp, move randomly and collide with each other after a random time interval of free flight. The

time interval of these free flights are distributed exponentially about a mean free time interval τ_c, which depends on the temperature of the system,

$$p(\tau_i) = \exp(-\tau/\tau_i).$$

The magnitude of the collisional broadening depends on the frequency of the collisions which is inverse of the mean time interval τ_c. These collisions cause an abrupt change in the phase of the wave train emitted by the atoms.

$$E = E_0 \exp(-i\omega_0 t + i\phi(t))$$

where $\phi(t) = \phi_n$ for $t_0 < t < t_0 + \tau_i$. For a collection of identical atoms, the overall effect is reflected in the emission line shape of the source as a broadened Lorentzian line shape. The expression for $L(\omega - \omega_{ik})$ given in Eq. 1.2, modifies as follows

$$L'(\omega - \omega_{ik}) = \frac{\Gamma'^2}{[(\omega - \omega_{ik})^2 + \Gamma'^2]},$$

where $\Gamma' = \Gamma + 2/\tau_c$.

2) Doppler Broadening:- Due to thermal motion of the atoms, there is a corresponding Doppler shift in the frequency spectrum of the emitted light. This broadens the spectrum by imprinting the effect of Maxwellian distribution of velocity component of the gas in the emitted frequency spectrum and depends on the temperature T. The overall line shape is a Gaussian [27],

$$I(\omega) = I_0 \exp\left[\frac{-(\omega - \omega_{ik})^2}{0.36(\Delta\omega_d)^2}\right],$$

where

$$\Delta\omega_d = \frac{(2\omega_{ik}\sqrt{2RTln2/M})}{c}$$

is the full width at half maximum of the resultant line shape.

The combined effect of all these broadening mechanisms in the frequency spectrum and their interference, governs the coherence properties of these light sources where coherence of light beam refers to the stability of the phase of a light beam over time and space. In general there are two types of coherence parameters for a light beam : *temporal coherence* and *spatial coherence*.

While considering the temporal coherence of a light beam, the concern is about the ability of the light beam to interfere with a delayed version of itself, without any spatial shift. This kind of division of a light beam is called amplitude splitting and is used in Michelson (see Fig. 1.1) or Mach-Zehnder interferometer. On the other hand, the spatial coherence is the ability of a light beam to interfere with a spatially shifted version of itself, without having any relative time delay between them. This type of division of light beam is called wavefront splitting and is used for example in Young's double slit kind of experiment (Fig. 1.2).

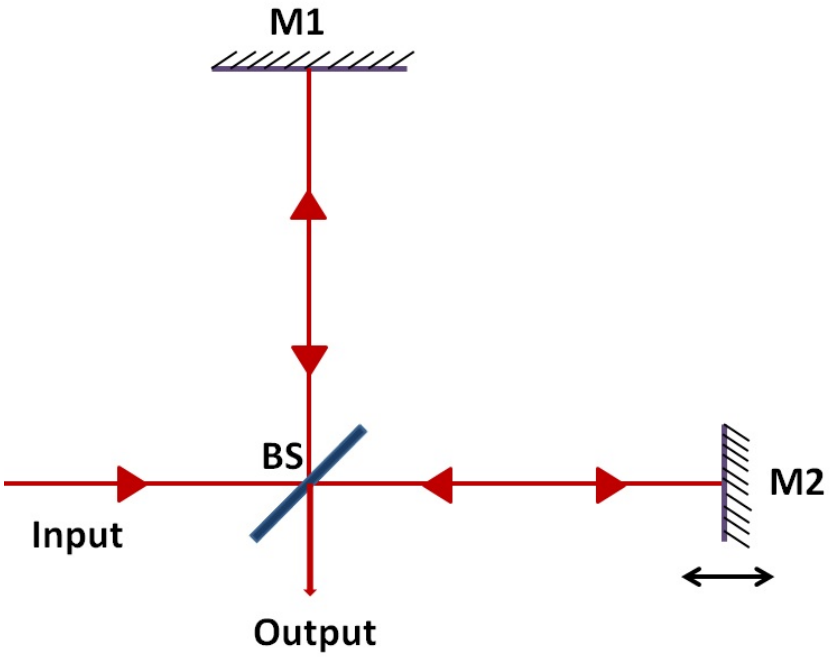

Figure 1.1: Measurement of temporal coherence for a light source by using Michelson interferometer. BS is the 50:50 beam splitter, M1 and M2 are two mirrors. If the path difference between the two arms, Δl is small enough to yield the interference fringes at the output port and if the time delay between the two arms Δt and the bandwidth of light $\Delta \nu$ satisfies $\Delta l = c\Delta t \sim \frac{c}{\Delta \nu}$, then Δl is a measure of longitudinal coherence length with Δt as coherence time.

Coherence Function

The degree of coherence of the light field can be quantified in more precise way in terms of the coherence function. Two different types of correlation function in two different types of interferometric setups can be used to study the coherence properties of a radiation field.

1)First order coherence function [28] :-

In its most generalized form the first order coherence function is the correlation of field amplitudes at two different space and time points.

$$g^{(1)}(r_1,t_1:r_2,t_2)=\frac{\langle E^*(r_1,t_1)E(r_2,t_2)\rangle}{(\langle(|E(r_1,t_1)|)^2\rangle\langle(|E(r_2,t_2)|)^2\rangle)^{1/2}},$$

where $\langle ...\rangle$ represents the average over a long time interval T, here as well as for further discussions, that is,

$$\langle E^*(r_1,t_1)E(r_2,t_2)\rangle=\frac{1}{T}\int_T E^*(r_1,t_1)E(r_2,t_2)dt.$$

The first order coherence function is a measure of the sharpness of the interference fringes and is therefore related to the visibility of the fringes formed on the plane of observation (screen) of a Young's double slit interferometer, when the two slits are illuminated with radiation fields. From the laws of interference the resultant irradiance at any point on the screen can be written as

$$I_R=I_1+I_2+2\sqrt{I_1I_2}Re\left[\gamma_{12}(\tau)\right], \tag{1.3}$$

where $\tau=t_1-t_2$, I_1 and I_2 are the time averaged illumination at observation point due to two pinholes respectively and,

$$\gamma_{12}(\tau)=\frac{\langle E_1(t+\tau)E_2^*(t)\rangle}{(\langle|E_1(t)|^2\rangle\langle|E_2(t)|^2\rangle)^{1/2}}=g^{(1)}(\tau), \tag{1.4}$$

is called the complex degree of coherence. The extreme values, $|\gamma_{12}(\tau)|=1$ and 0 describes interference of two mutually completely coherent and completely incoherent waves respectively. For $0<|\gamma_{12}(\tau)|<1$ we have partial coherence. The first order coherence function can be related with the visibility of the fringes at a given point p, $V(p)$, as follows

$$V(p)=\frac{I_{max}-I_{min}}{I_{max}+I_{min}}=\frac{2\sqrt{I_1(p)}\sqrt{I_2(p)}}{I_1(p)+I_2(p)}|\gamma_{12}(\tau)| \tag{1.5}$$

where I_{max} and I_{min} refers to maximum and minimum intensity at point p as the phase of $\gamma_{12}(\tau)$ oscillates between 0 and 2π. For the case of equal irradiance through the two pinholes of the interferometer, at point p,

$$V(p)=|\gamma_{12}(\tau)| \tag{1.6}$$

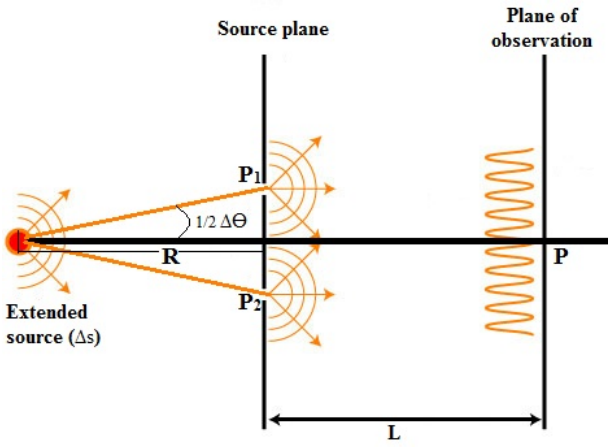

Figure 1.2: The transverse spatial coherence of an extended source can be measured by Young's double slit experiment. Fringes form on the screen when $\Delta\theta\Delta s \leq \bar{\lambda}$, which in turn defines the coherence area for limiting condition, $\Delta A \sim (R\Delta\theta)^2 \sim \frac{R^2\bar{\lambda}^2}{s}$. Here $\Delta\theta$ is the angular separation between the slits, R is the distance between the slits and source, Δs is the dimension of the slit with area $S = (\Delta s)^2$ and $\bar{\lambda}$ is the wavelength of light. The square root of the coherence area gives the transverse coherence length.

2)Second order coherence function:- Second order coherence function or intensity correlation function is the fourth order correlation function of the electric field amplitudes at two different space time points. The formal expression can be written as follows

$$G^{(2)}(r_1,t_1:r_2,t_2) = \frac{\langle E^*(r_1,t_1)E^*(r_2,t_2)E(r_2,t_2)E(r_1,t_1)\rangle}{(\langle(|E(r_1,t_1)|)^2\rangle\langle(|E(r_1,t_1)|)^2\rangle)}$$

$$G^{(2)}(r_1,t_1:r_2,t_2) = \frac{\langle \overline{I}(r_1,t_1)\overline{I}(r_2,t_2)\rangle}{(\langle(\overline{I}(r_1,t_1))\rangle\langle(\overline{I}(r_2,t_2))\rangle)} \tag{1.7}$$

In classical coherence theory, second order coherence function measures the correlation between the intensity fluctuations at two different space time points rather than the correlation between the fields. The setup used to measure the second order coherence function is known as Hanbury-Brown and Twiss (HBT) interferometer. When exploited for measuring intensity-intensity correlation for photons, $G^{(2)}$ can reveal the quantum nature of light sources, which may not be seen in Young's double slit interference experiment (Section 1.2.7). Due to its wide applicability in quantum optics, a brief description is given for HBT interferometry in the next section 1.2.2.

1.2.2 HBT Interferometry

In 1950 Hanbury-Brown and Twiss developed a new technique, based on the intensity-intensity correlation of two detectors located at two different space time points, to reveal information about the spatial as well as temporal coherence properties of the light sources in stellar interferometry. Classically this was explained in terms of superposition of waves because the wavefield incident on the detectors is a classical superposition of many independent realizations of Gaussian random processes. Due to this, the intensity fluctuations of the two detectors are correlated, if the observation is within coherence time and detectors are located within coherence volume, are correlated. This technique of intensity interferometry provides the possibility of measuring the magnitude of the normalized coherence function by means of correlation between the intensity fluctuation at two different points instead of correlation between the fields. The correlation between the intensity fluctuations recorded by the two detectors, for a thermal source, is related to the first order and the second order coherence function as follows,

$$|g^{(1)}(r_1, r_2, \tau)|^2 = \frac{\langle \Delta I(r_1, t) \Delta I(r_2, t+\tau) \rangle}{\langle I(r_1, t) \rangle \langle I(r_2, t) \rangle} = G^{(2)}(r_1, r_2, \tau) - 1 \tag{1.8}$$

The HBT experiment is used to analyse the coherence properties of light sources. In its simplest form, HBT interferometer has a 50:50 beam splitter dividing the light beam into two parts which are analysed by two photomultiplier tubes or photon counting detectors (Fig. 1.3). The correlation between the currents of the two detectors as a function of delay between them quantifies the second order coherence function of the source given in Eq. 1.7. The function $G^2(\tau)$ can also be used to find the photon statistics of different kinds of light sources and to classify them according to second order correlation function (section 1.2.7) which may not be possible in a Young's double slit experiment. In fact HBT experiment is one of the first experiments which has laid down the basic foundation of quantum optics. It has reached a wide range of applications. A few of which are, the measurement of two identical particle correlation in particle physics[30, 31], determination of collisional volume in heavy ion collision experiment [32], conformation of the presence of a single atom/ion in a single particle traps [33, 34]. It also finds applications in experiments related to condensed matter systems and in ultra-cold atom experiments[35–38].

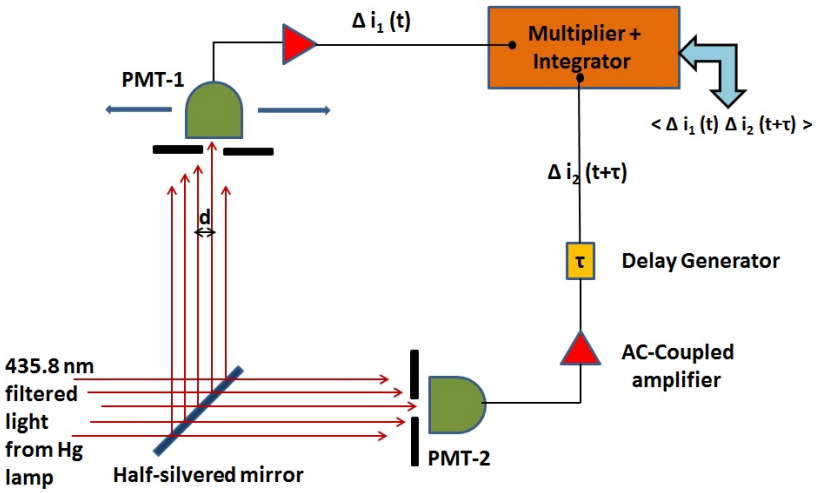

Figure 1.3: The schematic of the original HBT experimental setup. Spectrally filtered light at 435.8 nm from a Hg lamp is divided by a half-silvered mirror and incident on two photomultiplier tubes PMT-1 and PMT-2. The signals from PMTs are amplified and filtered using AC-coupled amplifiers to get fluctuation signals $\Delta i_1(t)$ and $\Delta i_2(t+\tau)$. These signals are fed to an electronic multiplier-integrator circuit to generate output which is proportional to $\langle \Delta i_1(t) \Delta i_2(t+\tau) \rangle$. The translation of PMT-1 can be used to investigate spatial coherence of the light source.[29]

1.2.3 Quantum representation of the light states

There are different formalisms to represent the quantum mechanical state of a light field. The most frequently used representations in quantum optics are in terms of field quadratures, density operators or Wigner functions.

Density Operator

In this representation the quantum state of light $|\psi\rangle$ is described in terms of its density operator which, for an ensemble of quantum states, is defined as follows

$$\hat{\rho} = \sum_i p_i \, |\psi_i\rangle\langle\psi_i|, \tag{1.9}$$

where $\Sigma_i \, p_i = 1$ and p_i is the probability of i^{th} state $|\psi_i\rangle$ in the complete system. A pure state in this representation is a state $|\psi\rangle$ with only one contribution $p_i = 1$, all others being zero ($p_{j\neq i} = 0$). Some of the properties of the density matrix can be seen by expanding density

operator in some basis $\{|\phi_k\rangle|$ as follows

$$\hat{\rho} = \sum_{j,k} \rho_{jk} \, |\phi_j\rangle\langle\phi_k|, \quad \rho_{jk} = \langle\phi_j|\hat{\rho}|\phi_k\rangle \tag{1.10}$$

where ρ_{jk} is the $(j,k)^{th}$ element of the density matrix ρ. Now some of the properties of the operator $\hat{\rho}$ follows directly from this.

$$tr\{\hat{\rho}\} = 1 \tag{1.11}$$

This follows from the normalization condition of Eq. 1.9. If the state is pure then $tr\{\hat{\rho}^2\} = 1$.

Once the density operator of the quantum state is known, the expectation value of any observable can be written as

$$\langle\hat{A}\rangle = \sum_i p_i \, \langle\psi_i|\hat{A}|\psi_i\rangle = tr\left[\hat{\rho}\hat{A}\right] \tag{1.12}$$

Field Quadratures

In this approach, a single mode of the electromagnetic field is quantized in terms of the annihilation operator $\hat{a}$ and the creation operator $\hat{a^\dagger}$. For a multi-mode field, each mode (degree of freedom) is described in terms of an independent harmonic oscillator with its own set of creation and annihilation operators and the field itself is a collection of such harmonic oscillators. The Hamiltonian for the single mode of the field is given by

$$\hat{H} = \hbar\omega \left(\hat{a^\dagger}\hat{a} + \frac{1}{2}\right), \quad [\hat{a}, \hat{a^\dagger}] = 1 \tag{1.13}$$

The observables in quantum mechanics are Hermitian operators. For electromagnetic fields, Hermitian operators defined in terms of non-Hermitian operators $\hat{a}$ and $\hat{a^\dagger}$ are

$$\hat{q} = \frac{\hat{a} + \hat{a^\dagger}}{\sqrt{2}}, \qquad \hat{p} = \frac{\hat{a} - \hat{a^\dagger}}{i\sqrt{2}} \tag{1.14}$$

with a setting $\hbar = 1$. $\hat{p}$ and $\hat{q}$ are known as field quadrature operators and are analogous to position and momentum operator of a quantum harmonic oscillator. Now the Hamiltonian in terms of field quadrature operator reads as follows

$$\hat{H} = \frac{1}{2}\omega \left(\hat{q^2} + \hat{p^2}\right), \qquad [\hat{q}, \hat{p}] = i. \tag{1.15}$$

The generalized quadrature operator is written as

$$\hat{q}_\theta = \frac{1}{\sqrt{2}}\left(\hat{a}e^{-i\theta} + \hat{a}^\dagger e^{i\theta}\right) = \hat{q}\cos\theta + \hat{p}\sin\theta. \tag{1.16}$$

The generalized quadrature spans out the operators from $\hat{p}$ to $\hat{q}$ or anything in between, for θ going between 0 and 2π. The eigen state basis of the generalized quadrature operator is orthogonal and complete. If $|q_\theta\rangle$ is the eigen state such that $\hat{q_\theta}|q_\theta\rangle = q_\theta|q_\theta\rangle$ then

$$\langle q_\theta|q_{\theta'}\rangle = \delta(q_\theta - q_{\theta'}), \quad \int |q_\theta\rangle\langle q_\theta| dq_\theta = 1. \tag{1.17}$$

The field quadratures obey the uncertainty principle, that is,

$$\Delta\hat{q}\Delta\hat{p} \geq \frac{1}{2} \tag{1.18}$$

A quantum states following the equality of the uncertainty principle is called a minimum uncertainty state.

Wigner function

Wigner function was introduced by Eugene Wigner in 1932 as a link between the wavefunction in Schrodinger equation for a quantum state and the phase-space probability distribution function. This quasi-probability distribution function is a real valued function which represents a quantum state in quadrature phase-space. The most important point related to Wigner function is its negativity being a strong indication of a non-classical state [39]. The Wigner function representation in terms of quadrature variables q and p is given by [28]

$$W(q,p) = \frac{1}{2\pi}\int_{-\infty}^{\infty} e^{ip\zeta}\langle q - \zeta/2|\hat{\rho}|q + \zeta/2\rangle d\zeta, \tag{1.19}$$

Normalization for probability distribution is taken care by

$$\int\int_{-\infty}^{\infty} W(q,p)dpdq = 1, \quad \text{with} \quad |W(q,p)| \leq \frac{1}{\pi} \tag{1.20}$$

It can be seen that Wigner function contains the full information about the state and has a one to one relation to the density matrix. The true probability distribution which is called the marginal distribution for a set of quadratures q and p can be written as follows

$$pr(q) = \int_{-\infty}^{\infty} W(q,p)dp = \langle q|\hat{\rho}|q\rangle \tag{1.21}$$

$$pr(p) = \int_{-\infty}^{\infty} W(q,p)dp = \langle p|\hat{\rho}|p\rangle \tag{1.22}$$

$$\tag{1.23}$$

For generalized quadrature q_θ, the marginal probability distribution is

$$pr(q_\theta) = \int_{-\infty}^{\infty} W(q\cos\theta - p\sin\theta, q\cos\theta + p\sin\theta)dp \tag{1.24}$$

The expectation value of an operator $\hat{A}$ can be evaluated from its Wigner function

$$\langle\hat{A}\rangle = 2\pi \int\int_{-\infty}^{\infty} W(q,p)W_A(q,p)dqdp, \tag{1.25}$$

where Wigner function of the operator $\hat{A}$ is defined as

$$W_A(q,p) = \frac{1}{2\pi}\int_{-\infty}^{\infty} e^{ip\zeta}\langle q-\zeta/2|\hat{A}|q+\zeta/2\rangle d\zeta \tag{1.26}$$

1.2.4 Different States of Light

Fock or Number State

The Hamiltonian in Eq. 1.13 has eigen values $\hbar\omega_k(n_k + \frac{1}{2})$ where n_k is an integer. Eigen states $|n_k\rangle$ are called number or Fock states and are the eigenstates of the number operator $N_k = a_k^\dagger a_k$

$$a_k^\dagger a_k|n_k\rangle = n_k|n_k\rangle \tag{1.27}$$

where a_k and $a_k^\dagger$ represents the annihilation and the creation operators of a photon with wave vector **k**. The operation of the creation and the annihilation operators to the number states is given as follows

$$a_k|n_k\rangle = n_k^{1/2}|n_k-1\rangle, \quad a_k^\dagger|n_k\rangle = (n_k+1)^{1/2}|n_k+1\rangle. \tag{1.28}$$

The state vector for the higher excited states may be obtained from the vacuum by successive application of the creation operator

$$|n_k\rangle = \frac{(a_k^\dagger)^{n_k}}{(n_k!)^{1/2}}|0\rangle, \quad n_k = 0,1,2..... \tag{1.29}$$

The number states are orthogonal and form a complete set of basis vectors for a Hilbert space

$$\langle n_k|n_k\rangle = 1, \quad \sum_{n_k=0}^{\infty}|n_k\rangle\langle n_k| = 1. \tag{1.30}$$

The Wigner function of the number state $|n\rangle$ is given by [28]

$$W_n(q,p) = \frac{1}{\pi}e^{-q^2-p^2}(-1)^n L_n^{(0)}\left[2(q^2+p^2)\right]. \tag{1.31}$$

where $L_n^{(0)}[x]$ is the ordinary Laguerre polynomial evaluated at x. This has a non-Gaussian form except for vacuum state $|0\rangle$.

Coherent State

These are the states of the quantized radiation field which have properties similar to those of a classical electromagnetic field in the limit of large amplitudes. That is the reason these are considered as one of the "most classical" quantized states of the radiation field. The light emerging out of a laser is an example of a coherent state.

The coherent state is represented by $|\alpha\rangle$ and it is the eigen state of the annihilation operator of a harmonic oscillator. If $\hat{a}$ is the annihilation operator

$$\hat{a}|\alpha\rangle = \alpha|\alpha\rangle, \quad \text{and} \quad \langle\alpha|\hat{a^{\dagger}} = \langle\alpha|\alpha^{*} \tag{1.32}$$

where α is any complex number. The product of uncertainty in the amplitude and the phase for a coherent state is the minimum allowed by the uncertainty principle. This has a variance of $1/2$ (setting $\hbar = 1$) which is independent of phase and amplitude. The coherent state is therefore a state with minimum uncertainty and its variance is often referred as the standard quantum limit. It can be expanded in the number state basis as follows

$$|\alpha\rangle = e^{-|\alpha|^2/2} \sum_{n=0}^{\infty} \frac{\alpha^n}{\sqrt{n!}}|n\rangle. \tag{1.33}$$

It can be seen from the above form that coherent states form an over complete basis set, therefore they are non-orthogonal but complete,

$$\langle\alpha|\alpha\rangle = \exp\left(-|\alpha|^2\right) \sum_{n} \frac{\alpha^{*n}\alpha^n}{n!} = 1, \quad \text{but} \tag{1.34}$$

$$\langle\alpha|\beta\rangle = \exp\left(-\frac{1}{2}|\alpha|^2 - \frac{1}{2}|\beta|^2 + \alpha^{*}\beta\right) \tag{1.35}$$

The Wigner function of the coherent state is written as [28]

$$W_{\alpha}(q,p) = \frac{1}{\pi} e^{-(q-q_0)^2-(p-p_0)^2}, \tag{1.36}$$

It is clearly a Gaussian form. Therefore the coherent state is classified as Gaussian state.

Thermal State

The classical state of light obtained from a black body radiation at temperature T is termed as a thermal state. It is an example of mixed state and its density matrix can be represented as a

statistical-mixture of coherent states or weighted sum of number states given as follows

$$\hat{\rho} = \int_{-\infty}^{\infty} \mathcal{P}(\alpha)|\alpha\rangle\langle\alpha|\, d^2\alpha = \sum_{n=0}^{\infty} p(n)\,|n\rangle\langle n| \tag{1.37}$$

where $\mathcal{P}(\alpha)$ is Glauber-Sudarshan's P function [28]. $p(n)$ for the thermal state reads as follows

$$p(n) = \exp\left(-\beta\, n\, \hbar\omega\right)\left\{1 - \exp\left(-\beta\, \hbar\omega\,\right)\right\} \tag{1.38}$$

where $\beta = 1/k_B T$. The average photon number of a thermal field is given by

$$\bar{n} = \langle\hat{n}\rangle = \mathrm{tr}[\hat{\rho_{th}}\, \hat{a}^{\dagger}\, \hat{a}] = \left(\exp\{\beta\, \hbar\omega\} - 1\right)^{-1}, \tag{1.39}$$

also called as Bose-Einstein distribution. The $\mathcal{P}(\alpha)$ for the thermal state in terms of the average photon number can be written as,

$$\mathcal{P}(|\alpha|) \equiv \mathcal{P}_{\mathrm{th}}(|\alpha|) = \frac{1}{\bar{n}\pi} \exp(-|\alpha|^2/\bar{n}). \tag{1.40}$$

The Wigner function of the thermal state is [28]

$$W_{th} = \frac{1}{2}\frac{1}{2\langle\hat{n}\rangle + 1} \exp\left(-\frac{q^2 + p^2}{2\langle\hat{n}\rangle + 1}\right) \tag{1.41}$$

The thermal state is a Gaussian state as its Wigner function has a Gaussian form.

Squeezed State

These are the states within the class of the states with minimum uncertainty and in general may have less noise in one of the quadrature compared to the coherent state. To satisfy the condition of minimum uncertainty state the noise in the other quadrature is greater than that of a coherent state. Coherent state can be considered a specific case of this class of state with equal uncertainty in both quadratures.

Single-mode squeezing

Single mode squeezed state may be generated by using unitary squeeze operator defined as

$$S(\varepsilon) = \exp\left(\frac{1}{2}\varepsilon^* a^2 - \frac{1}{2}\varepsilon a^{\dagger 2}\right) \tag{1.42}$$

where $\varepsilon = re^{2i\phi}$. The squeeze operator obeys the following relations

$$S^{\dagger}(\varepsilon) = S^{-1}(\varepsilon) = S(-\varepsilon) \tag{1.43}$$

The action of the squeezed operator on creation and annihilation operator as defined earlier is,

$$S^{\dagger}(\varepsilon)\,\hat{a}\,S(\varepsilon) = \hat{a}\cosh r - \hat{a}^{\dagger}e^{i\phi}\sinh r, \tag{1.44}$$

and similar for its Hermitian adjoint. The squeeze operator has the following transformation properties

$$S^{\dagger}(\varepsilon)\,(\hat{Q}_1 + i\hat{P}_1)\,S(\varepsilon) = Q_1 e^{-r} + P_1 e^{r}, \tag{1.45}$$

where $Q_1 + iP_1 = (q_1 + ip_1)e^{-i\phi}$ is a rotated complex amplitude. It can be seen from here that the squeeze operator attenuates one component of the complex amplitude and amplifies the other. $r = |\varepsilon|$ determines the attenuation or amplification and called as *squeeze factor*. A squeezed state $|\alpha, \varepsilon\rangle$ is written as a displacement of a squeezed vacuum state,

$$|\alpha, \varepsilon\rangle = \hat{D}(\alpha)S(\varepsilon)|0\rangle \tag{1.46}$$

where displacement operator is defined as follows

$$\hat{D}(\alpha)|0\rangle = e^{\alpha\hat{a}^{\dagger} - \alpha^{*}\hat{a}}|0\rangle = |\alpha\rangle. \tag{1.47}$$

A squeezed state has the following expectation value and uncertainty in quadrature components

$$\Delta Q_1 = e^{-r}, \quad \Delta P_1 = e^{r}, \tag{1.48}$$

$$\langle N\rangle = \sinh^2 r, \tag{1.49}$$

$$\langle q_1 + ip_1\rangle = \langle Q_1 + iP_1\rangle e^{i\phi} = 2\alpha \tag{1.50}$$

It can be noted from above that increasing the squeezing amplitude r will increase the mean photon number. Even squeezing the vacuum will have a non-zero mean photon number.

1.2.5 Gaussian and non-Gaussian Quantum states

Quantum states are sometime classified according to their Gaussian and non-Gaussian nature of the Wigner function in quadrature space. Coherent states, squeezed states and thermal states

are the examples of states with Gaussian Wigner function. The distinct feature of these states is that being Gaussian states they can be characterized by their covariance matrices with the first and second order moments of canonical quadrature variables.

Gaussian states are important in describing the basic nature of the quantum mechanical phenomenon in quantum optics and quantum information science, in the discrete variable approach. Non-Gaussian resources are necessary to implement a universal quantum computation, based on continuous variable schemes. This motivates towards the generation of non-Gaussian non-classical states.

1.2.6 Photon Added thermal state

As a theoretical proposal, Agarwal and Tara in 1991-92 defined new types of non-classical states by photon addition on a classical field like a thermal state [22] or a coherent state [40]. This was shown analytically that repeated application of photon addition operation on a radiation state $\hat{\rho}$ can generate states with non-classical feature. As an example the calculation for a single photon added thermal state is presented below. This technique is used later in the section 1.5.1.

The single photon addition operation on a thermal state, given by Eq. 1.40 can be written as follows

$$\hat{\rho}_{\rm th}^{1} = \frac{1}{N_1}\,\hat{a}^{\dagger}\,\hat{\rho}_{\rm th}\,\hat{a} \tag{1.51}$$

Here the superscript 1 indicates that we have added one photon, and N_1 is an appropriate normalization constant. The Glauber-Sudarshan's diagonal weight functions [5] of the single photon-added thermal (SPATS) state can be calculated as follows [22]. The density matrix for SPATS is

$$\hat{\rho}_{\rm th}^{1} \propto \int e^{-|\alpha|^2/\bar{n}} a^{\dagger}|\alpha\rangle\langle\alpha|\,a\,d^2\alpha \tag{1.52}$$

using the property (see Appendix:-A)

$$a^{\dagger}(|\alpha\rangle e^{|\alpha|^2/2}) = \frac{\partial}{\partial\alpha}(|\alpha\rangle e^{|\alpha|^2/2}), \tag{1.53}$$

The density matrix reads as

$$\hat{\rho}_{\rm th}^{1} \propto \int e^{-|\alpha|^2(1+\frac{1}{\bar{n}})}\frac{\partial}{\partial\alpha}(|\alpha\rangle e^{|\alpha|^2/2})\frac{\partial}{\partial\alpha^*}(\langle\alpha|e^{|\alpha|^2/2})\,d^2\alpha \tag{1.54}$$

Now integrating by parts and using the boundary condition for $|\alpha\rangle$, we get,

$$\hat{\rho}^1_{\rm th} \propto \int \left[e^{|\alpha|^2} \frac{\partial^2}{\partial\alpha\partial\alpha^*} e^{-|\alpha|^2(1+\frac{1}{\bar{n}})} \right] |\alpha\rangle\langle\alpha| \, d^2\alpha. \tag{1.55}$$

Comparing Eq. 1.55 to the Eq. 1.37, the distribution function $\mathcal{P}(\alpha)$ for SPATS can be written as

$$\mathcal{P}^1_{\rm th}(|\alpha|) \propto (|\alpha|^2(1+\bar{n}) - \bar{n}) \, \exp[-|\alpha|^2/\bar{n}], \tag{1.56}$$

After Normalization, the final expression for Glauber-Sudarshan diagonal weight function for SPATS is

$$\mathcal{P}^1_{\rm th}(|\alpha|) \;\; = \;\; \frac{1}{\pi\,\bar{n}^3} \, (|\alpha|^2(1+\bar{n}) - \bar{n}) \, \exp[-|\alpha|^2/\bar{n}], \tag{1.57}$$

Mandel Parameter

Non-classicality for a quantum state of light can be quantified in terms of the degree of squeezing [22] or quantifying its sub-Poissonian character. The sub-Poissonian character can be examined by the Mandel parameter Q which can be defined in terms of creation and annihilation operator for a single mode field as follows

$$Q = \frac{\langle \hat{a}^{\dagger 2}\hat{a}^2\rangle - \langle \hat{a}^\dagger\hat{a}\rangle^2}{\langle \hat{a}^\dagger\hat{a}\rangle} \tag{1.58}$$

where [22, 41],

$$\langle \hat{a}^{\dagger n}\hat{a}^n\rangle = \int \mathcal{P}(|\alpha|)|\alpha|^{2n} d^2\alpha \; . \tag{1.59}$$

In our case of single photon added states, we evaluate $\langle \hat{a}^{\dagger n}\hat{a}^n\rangle$ for state $\hat{\rho}^1_{th}$ with the following standard procedure.

$$\langle \hat{a}^{\dagger 2}\hat{a}^2\rangle = \int \mathcal{P}(|\alpha|)|\alpha|^4 d^2\alpha \tag{1.60}$$

From Eq. 1.59, and converting the equation into polar co-ordinates with $|\alpha| = |re^{i\theta}| = r$

$$\langle \hat{a}^{\dagger 2}\hat{a}^2\rangle = \frac{1}{\pi\bar{n}^3} \left[2\pi \left((1+\bar{n}) \int_0^\infty r^7 e^{-\frac{r^2}{\bar{n}}} dr - \bar{n} \int_0^\infty r^5 e^{-\frac{r^2}{\bar{n}}} dr \right) \right] \tag{1.61}$$

where the factor 2π comes from the integration over θ. Substituting the values of definite integrals, Finally Eq. 1.61 takes the following form

$$\langle \hat{a}^{\dagger 2}\hat{a}^2\rangle = \left[6\bar{n}^2 + 4\bar{n} \right] \tag{1.62}$$

Similarly one can calculate $\langle \hat{a}^\dagger \hat{a} \rangle$ to get,

$$\langle \hat{a}^\dagger \hat{a} \rangle = (2\bar{n} + 1). \tag{1.63}$$

The Mandel parameter from Eq. 1.58 can be written as

$$Q = \frac{2\bar{n}^2 - 1}{2\bar{n} + 1} \tag{1.64}$$

1.2.7 Light source characterization at the photon level

One of the methods of characterizing the quantum state of a light source, is a photon coincidence measurement (intensity correlation measurement) using a Hanbury Brown-Twiss intensity interferometer. The second order coherence function is written in terms of the photon creation and annihilation operator [28]

$$G^{(2)}(\tau) = \frac{\langle a^\dagger(0) a^\dagger(\tau) a(\tau) a(0) \rangle}{\langle a^\dagger(0) a(0) \rangle}. \tag{1.65}$$

Here the light source is assumed to be time-invariant (stationary). In terms of photon number operator $n(t) = a^\dagger(t)a(t)$, the expression for $G^{(2)}(\tau)$ can also be written as follows

$$G^{(2)}(\tau) = \frac{\langle : n(\tau) n(0) : \rangle}{\langle n(0) \rangle^2}, \tag{1.66}$$

where : denotes normal ordering of the operators.

$G^{(2)}(\tau)$ is an important parameter as it can give the information about photon number distribution indirectly. $G^{(2)}(\tau) = 1$ refers to poissonian, while $G^{(2)}(\tau) > 1$ and $G^{(2)}(\tau) < 1$ refers to a superpoissonian and subpoissonian light sources respectively. The bunching and antibunching behaviour of photons generated from a thermal light source and a single photon source can be observed by $G^{(2)}(\tau)$ values at zero time delay between the two detectors. $G^{(2)}(0) = 2$ represents bunching of photons which is the characteristic of a thermal light source while $G^{(2)}(0) = 0$ is a signature for antibunched photon indicating a single photon source. It should be noted that for very long time differences between the two detectors, there is no correlation i.e. $G^{(2)}(\tau \to \infty) = 1$.

The zero time delay correlation values for different states of light is given below:-

$$G^2(0) = 1, \quad \text{for coherent laser light} \tag{1.67}$$

$$G^2(0) = 2, \quad \text{for thermal light} \tag{1.68}$$

$$G^2(0) = 1 - \frac{1}{n}, \quad \text{for number state} \tag{1.69}$$

$$G^2(0) = 3 + \frac{1}{\langle n \rangle}, \quad \text{for single mode squeezed vacuum state} \tag{1.70}$$

where $\langle n \rangle = \sinh^2 r$ with r defined as squeezing parameter.

1.3 Tunable classical light sources

1.3.1 Pseudo Thermal light using ground glass plate

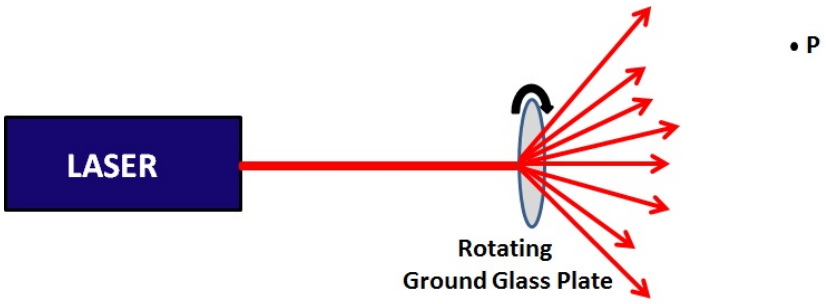

FIGURE 1.4: The coherent light from a narrow linewidth laser incident on a rotating ground glass plate which has randomly distributed scatters on its surface. It scatters light mimicking a chaotic light source with many independent radiators.

Generating Gaussian light sources with coherence characteristics similar to that of a thermal radiation but with a tunable coherence was first introduced by Martienssen and Spiller[20]. This is the most conventional method to create a pseudo-thermal light by diffusing a coherent laser light through a rotating diffuser, for example a ground glass plate (Fig. 1.4). The moving diffuser introduces extremely complex and irregular deformation of the incident wavefront. At a distant point P, the light can be considered as consisting of many independent contributions from different "correlation areas" on the diffuser and due to large ensemble of possible diffusers varying

in time due to rotation of the ground glass plate. The resultant intensity at point P fluctuates randomly in time, obeying negative exponential statistics as for a polarized thermal light. The complex field may be regarded as resulting from a random phaser sum with complex Gaussian statistics.

In their original work Martienssen and Spiller used a rotating diffuser plate in front of a thermal light source with short coherence time to generate a pseudo thermal light with longer and tailored coherence time. Later on Arecchi [21] demonstrated the complete characterization of the pseudo thermal light generated by scattering of coherent photons from a rotating ground glass (diffuser) plate.

1.3.2 Generation of tunable classical light sources using Acousto-Optic-Modulator

Acousto-Optic-Modulator

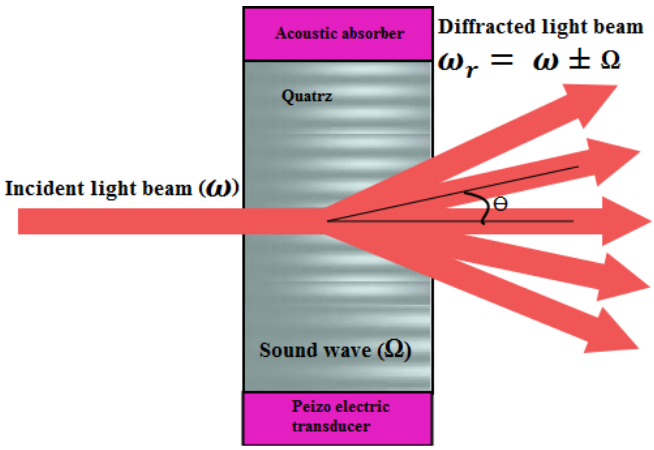

FIGURE 1.5: Acousto-Optic-Modulator diffracts the incident beam into different orders which are phase and frequency shifted with respect to the zeroth order diffracted beam. The shift in the phase and frequency is governed by the phase and frequency of rf electrical signal which is fed to the piezo electric transducer.

Acousto-Optic-Modulators (AOM), also known as Bragg cell, are the devices used to modulate the phase, frequency or the intensity of the light via acousto-optic interactions. As shown in the Fig. 1.5 a radio frequency (rf) electrical signal generates the acoustic waves in the transducer

attached to the crystal, which in turn modifies the refractive index of the crystal corresponding to the acoustic wave. This sets a moving diffraction grating inside the crystal. The light passing through such a moving grating gets diffracted in different orders with a modulation in its phase, frequency and intensity according to the rf signal. Thus sound waves control the properties of the diffracted light through the AOM crystal.

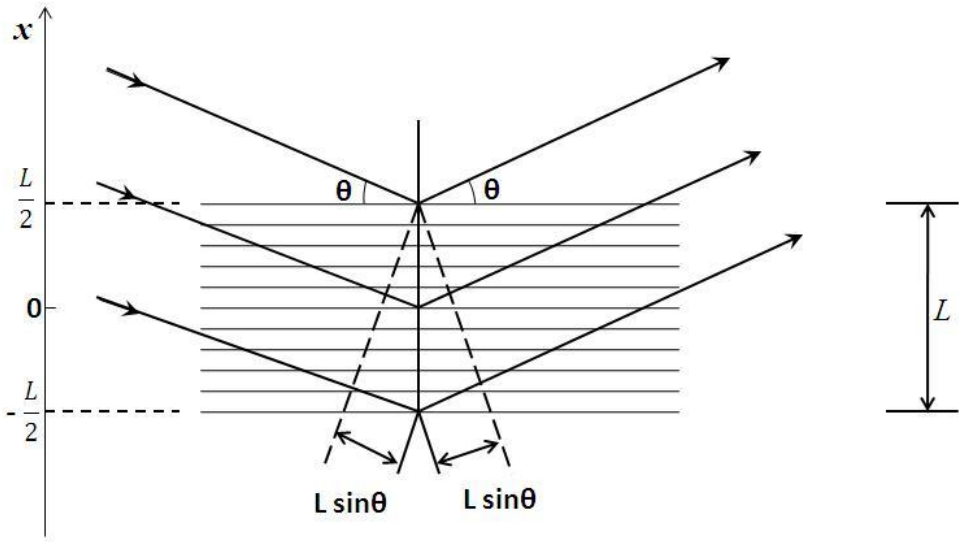

FIGURE 1.6: Light reflected from different layers of the inhomogeneous medium interferes resulting in intensity maxima and minima according to Bragg's condition.

In the Bragg's diffraction regime, the optical wave gets partially reflected from the stratified parallel planes set by the acoustic plane wave due to refractive index variation (Fig. 1.6). At one particular incidence angle θ, only one diffraction order is produced satisfying the Bragg's condition of constructive interference,

$$\sin\theta = \frac{\lambda}{2\Lambda} \tag{1.71}$$

where Λ is the wavelength of acoustic wave and λ is the wavelength of light in the medium.

The Bragg's condition in a crystal of sufficiently large dimension (L) compared to wavelength of sound waves (Λ) and for small incidence angle (θ) of incident wave vector of optical wave ($\boldsymbol{k}$), the Eq. 1.71 in terms of wave vectors is

$$\boldsymbol{k}_r = \boldsymbol{k} \pm \boldsymbol{q}, \tag{1.72}$$

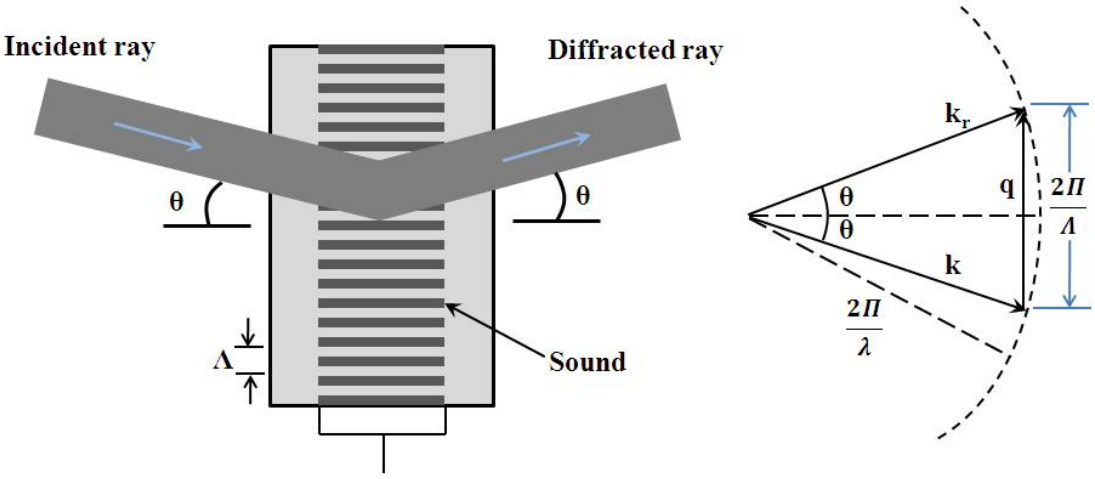

FIGURE 1.7: Figure shows the equivalence between Bragg's diffraction condition, $2k\sin\theta = q$ and the vector relation $\boldsymbol{k_r} = \boldsymbol{k} + \boldsymbol{q}$

.

where $\boldsymbol{k}_r$ is the wave vector of the diffracted optical wave and $\boldsymbol{q}$ is the wave vector for the sound wave (Fig. 1.7). The frequency of the output diffracted optical wave is Doppler shifted due to reflection from the moving grating. If Ω is the frequency of sound and ω of the input optical wave, then the frequency of reflected optical wave is

$$\omega_r = \omega \pm \Omega \tag{1.73}$$

The intensity of the light diffracted through the AOM crystal depends on the rf power fed to the AOM and expressed in terms reflectance

$$\mathcal{R} = 2\pi^2 n^2 L^2 \frac{\Lambda^2}{\lambda_0^4} \mathrm{M} I_s \tag{1.74}$$

n is the refractive index of the medium, λ_0 is the wavelength of the light, I_s is the intensity of the acoustic wave which is proportional to rf power and M is the material parameter.

1.3.3 Incoherent Light Generation by controlled phase randomization in a Mach-Zehnder setup

Experimental Setup

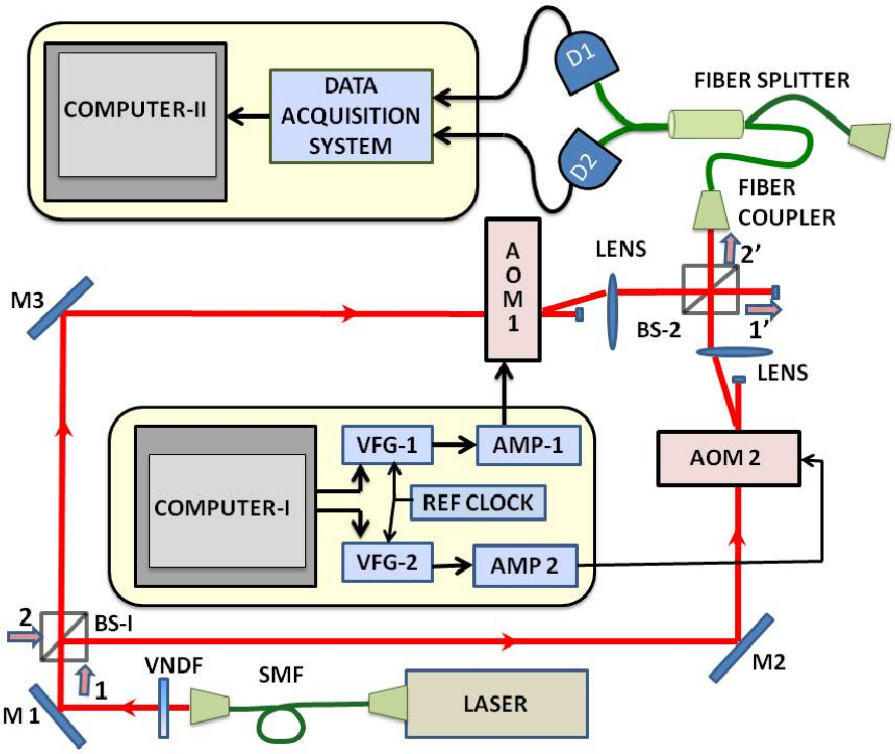

Figure 1.8: Schematic of the experiment. AMP - amplifier, AOM - acousto-optic modulator, BS - beam splitter, D1,D2 - detectors, M1 - M3 - mirrors, SMF - single mode fiber, VFG - versatile function generator, VNDF - variable neutral density filter.

The schematic of the experiment is given in Fig. 1.8. Coherent cw laser light from an external cavity diode laser (Toptica, 767 nm, linewidth < 5 MHz) was fiber coupled through a single mode polarization maintaining fiber. The light was then passed through a variable neutral density filter (VNDF) (to control the intensity of the beam) onto beam splitter BS1 where it was amplitude divided into two parts. These two beams traversed along the two arms of a Mach-Zehnder interferometer (MZI), which had an AOM in each of the two arms, arranged such that the first order diffracted light proceeded further on, while the undiffracted light was blocked. After traversing the two arms of the interferometer, the beams were combined at BS2, that is, the diffracted light beams of the two arms of the MZI interfered at BS2. Light emerging from one

of the exit ports of BS2 was directed into an input of a 50:50 fiber-splitter, and then onto two detectors, D1 and D2.

The two AOMs were driven by individual Versatile Function Generators (VFG, Toptica) which operated at 80 MHz radio frequency (rf); they were both referenced to a common 10 MHz clock. Using a LabVIEW interface we could tailor any distribution of phase and intensity fluctuations in the rf electrical signal being fed to the AOM on time scales ranging from few hundreds of nanoseconds to seconds. These fluctuations were transferred to the diffracted light by the acousto-optic interaction thus providing fine electronic control over the phase and intensity of the light. Measurements at the two detectors were used to determine the second order correlation (intensity-intensity correlation) function. For the case of continuous light intensity measurements, the laser was operated at a power of around $30\,\mathrm{m}$W and D1 and D2 were two fast photodiodes (Thorlabs PD10A-EC). For the case of photon coincidence detection, the laser light was strongly attenuated and photodiodes D1 and D2 were avalanche photo-diode (APD) based single photon counting modules (SPCM-AQR-15 Perkin Elmer) where an incident photon results in a TTL pulse with a detection efficiency of 65 % at 767 nm [1]. The outputs of D1 and D2 were stored in a PC using data acquisition systems. In the case of classical detectors, a digital storage oscilloscope was employed, while for photon counting, two counters on a data acquisition card (NI M-series PCI-6259) were used.

1.3.4 Generation of Incoherent Light by only phase modulation in an MZI setup

In this Section, we describe the creation of incoherent sources of light by imparting phase jumps to light by means of the AOMs in the MZI (Fig. 1.8). The use of a Mach-Zehnder interferometer was motivated by the facts that, i) phase changes imparted to light can be discerned only in an interferometric setup, and ii) it enables the creation of a source with intensity fluctuations even though only phase jumps are imparted to light.

[1] SPCM-AQR-15 is an avalanche photodiode based single photon counting module with a dead time of 50 ns. The quantum efficiency of the detector is 90 % at 767 nm. The dark count rate is less than 50 counts per second(cps)

Theory

The action of the MZI shown in the Fig.1.8 may be mathematically represented by the transformation matrix $M = B.\Phi.B$ where B (the operation of a beam splitter) and Φ (the action of the two AOMs) are given by

$$B = \frac{1}{\sqrt{2}} \begin{pmatrix} 1 & 1 \\ -1 & 1 \end{pmatrix} \quad \text{and} \quad \Phi = \begin{pmatrix} e^{i\phi_1(t)} & 0 \\ 0 & e^{i\phi_2(t)} \end{pmatrix} \tag{1.75}$$

Here $\phi_1(t)$ and $\phi_2(t)$ are the phase shifts imparted to light at AOMs 1 and 2, respectively. Thus, in terms of the scalar wave field, E_1 which enters at one of the ports of $BS1$ (and with no input at its other port), the output at $BS2$ is given by

$$\begin{pmatrix} E_{1'} \\ E_{2'} \end{pmatrix} = M. \begin{pmatrix} E_1 \\ 0 \end{pmatrix} \tag{1.76}$$

where 1, 2 represent the input ports of BS1 and 1', 2' the output ports of BS2. It is clear that the second order intensity self-correlation at the output ports is given by

$$G^2_{ii}(\tau) = \frac{\langle E_i^\star(t) E_i(t) E_i^\star(t+\tau) E_i(t+\tau) \rangle_t}{\langle E_i^\star(t) E_i(t) \rangle_t \langle E_i^\star(t+\tau) E_i(t+\tau) \rangle_t} \tag{1.77}$$

where i takes values 1', 2'. In terms of field operators $G^2_{ii}(\tau)$ is given by

$$\frac{\langle \psi | A_i{}^\dagger(t) A_i{}^\dagger(t+\tau) A_i(t+\tau) A_i(t) | \psi \rangle_t}{\langle \psi | A_i{}^\dagger(t+\tau) A_i(t+\tau) | \psi \rangle_t \langle \psi | A_i{}^\dagger(t) A_i(t) | \psi \rangle_t} \tag{1.78}$$

where

$$\begin{pmatrix} \hat{A_{1'}} \\ \hat{A_{2'}} \end{pmatrix} = M. \begin{pmatrix} \hat{a_1} \\ \hat{a_2} \end{pmatrix}, \tag{1.79}$$

with $|\psi\rangle$ being the input state, $\hat{a_1}$, $\hat{a_2}$ the annihilation operators of the input modes, and $\hat{A}_{1'}, \hat{A}_{2'}$ those of the output modes, and M is as defined earlier. In our setup, $|\psi\rangle = |E_1\rangle \otimes |0\rangle$, where

$|E_1\rangle$ is a coherent state. Simplification of Eqs. 1.77 and 1.78, for the case of complete phase noise, (i.e., uniformly distributed noise, with phase spanning the entire circle) both yield

$$G^2_{ii}(\tau) = 1 + \langle \cos(\delta\phi(t)) \cos(\delta\phi(t+\tau)) \rangle_t \tag{1.80}$$

where $\delta\phi = \phi_1(t) - \phi_2(t)$. Note that we have adjusted the MZI to match the dynamical paths in both arms and, therefore, the phase difference is the difference in the phases imparted at the two AOMs.

The temporal coherence of light, emerging out of the port 2', was determined by intensity correlation technique in a standard correlation setup developed by Hanbury-Brown and Twiss [29]. Equation (1.80) can be easily cast into the form

$$G^2_{2'2'}(\tau) \;\; = \;\; 1 + 0.5\xi(\tau), \tag{1.81}$$

where $\xi(\tau)$ represents the probability of temporal overlap of $\delta\phi(t)$ and $\delta\phi(t+\tau)$. In general, for complete phase noise given to AOM 1 and 2 and phase jumps occurring at time intervals t given by independent distributions $P_1(t)$ and $P_2(t)$ respectively, we have

$$\xi(\tau) = \frac{\int_\tau^\infty (t-\tau) P_1(t) d(t)}{\int_0^\infty t P_1(t) d(t)} . \frac{\int_\tau^\infty (t-\tau) P_2(t) d(t)}{\int_0^\infty t P_2(t) d(t)} \tag{1.82}$$

For the special case where one of the phases, say $\phi_2(t)$, is held constant Eq. 1.82 reduces to

$$\xi(\tau) = \frac{\int_\tau^\infty (t-\tau) P_1(t) d(t)}{\int_0^\infty t P_1(t) d(t)} \tag{1.83}$$

Experimental Results

We now present our experimental results. Initially, random phase jumps were imparted to AOM1 only and at regular intervals, that is, $P_1(t) = \delta(t - \tau_c)$. For this case, we see from Eq. 1.83 and Eq. 1.81,

$$\begin{aligned} G^2_{2'2'}(\tau) &= 1 + 0.5\left(1 - \frac{\tau}{\tau_c}\right) \quad \text{for} \quad \tau \le \tau_c \\ &= 1 \qquad\qquad\qquad\quad \text{for} \quad \tau \ge \tau_c \end{aligned} \tag{1.84}$$

Thus it is clear from here that, on imparting phase noise one expects photon-bunching with a zero-delay second-order correlation value 1.5, that falls to 1 for long delays. In the experiment,

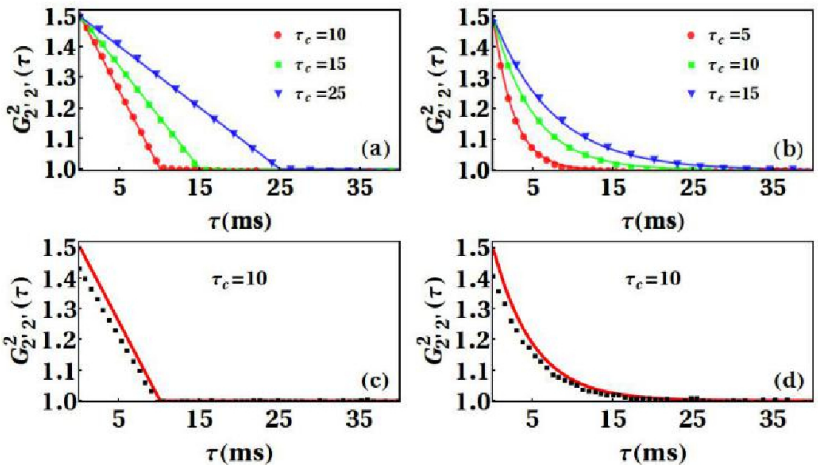

FIGURE 1.9: Intensity-intensity correlation function, $G^2_{2'2'}(\tau)$ of the light exiting port 2' of BS2 in Fig. 1.8, as function of τ for (a) constant dwell time noise to rf of one AOM, and with classical light detection; (b) exponential distribution of dwell times of noise in both AOMs, and with classical light detection; (c) same as (a), but in photon counting regime; (d) same as (b), but in photon counting regime.

at constant time intervals, τ_c, the rf electrical signal to AOM1 was given a random phase jump, distributed uniformly in the interval $(-\pi, \pi)$. The experimentally determined values of $G^2_{2'2'}(\tau)$ are shown as discrete points in Fig. 1.9 (a) for three different values of coherence time, τ_c. The continuous curves are $G^2_{2'2'}(\tau)$ as obtained from Eq. 1.84.

Next, AOMs 1 and 2 were driven with rf voltages with independent, random phase jumps uniformly distributed in the interval $(-\pi, \pi)$, and at time intervals that had independent exponentially falling distributions, $P(t) = [\exp(-t/\tau_c)]/\tau_c$, with $1\,\mathrm{ms} \leq t \leq 100\,\mathrm{ms}$ and with a mean, $\sim \tau_c$. The results for this case are presented in Fig. 1.9(b), for three values of τ_c. As in the previous case, the agreement between theory and experiment is very good.

The above measurements, which utilized classical detection of intensities with photodetectors, were repeated in the photon counting regime using APD based single-photon counting modules (SPCM). The laser light was strongly attenuated, so that, on an average, every $30\,\mu$s, there was a 10% probability of detecting a photon. Thus, there was, on an average, less than one photon in the interferometer at any instant of time. The output pulses from D1 and D2 (APD based SPCMs) were fed to two counters operating at a time bin of $30\,\mu$s, that was shorter than the mean interval between phase jumps that ranged from $1\,\mathrm{ms}$ to $100\,\mathrm{ms}$. The values of $G^2(\tau)$ obtained

from the experiments for the two cases (phase jumps to one AOM only at constant intervals and phase jumps to both AOMs with exponential distribution of interval between jumps) are shown in Figs. 1.9(c) and 1.9(d), along with theoretically expected values. The agreement is fair. In order to obtain sufficient statistics at single photon detection level, data had to be acquired over long durations. Mechanical instability of the interferometer and dark counts are believed to have contributed to the deviation from the theoretical curves in the photon counting regime.

From the above, it is amply clear that classical light sources exhibiting bunching and with the desired temporal coherence characteristics may be created from continuous coherent laser light. The results also confirm the equivalence between classical intensity-intensity correlation and coincidence detection for $G^2(\tau)$ measurement for classical states of light. In the present experiment, the phase fluctuations are on the milliseconds time scales due to restriction of the data acquisition card. The setup allows for a temporal variation from $50\,\mathrm{ns}$ (currently limited to $500\,\mathrm{ns}$ by USB 2.0 communication) to few seconds depending upon the stability of the interferometer. This provides an easy way of creating bunched light with long coherence times. Further the bunching can be enhanced and higher values of $G^2_{2'2'}(0)$ can be obtained by using engineered partial phase noise in this interferometric setup [18].

1.4 Tailoring Photon Number Distribution by Intensity Modulation of Light

In this Section, we demonstrate the creation of classical incoherent states with desired photon number distributions (PND), starting from an input coherent state. This was achieved by modulating the diffraction efficiency of a single AOM by the addition of calibrated amplitude noise with the desired characteristics to the input rf electrical signal. This, in effect, modulates the transmittivity of the coherent state through the AOM according to the chosen probability distribution function, thereby providing a source of classical light with a tailored photon number distribution.

1.4.1 Theory

Consider the coherent state $|\alpha\rangle$ being diffracted by an AOM where the transmittivity into the diffracted order (amplitude of the coherent state) is modulated in time, in the from of $\mathcal{P}(|\alpha|)$. The modulated coherent state and its expansion in terms of number (Fock) states can be written as

$$\begin{aligned} \hat{\rho} &= \int_0^{|\alpha_0|} \mathcal{P}(|\alpha|)|\alpha\rangle\langle\alpha|\, d^2|\alpha| = \sum_{n=0}^{\infty} p(n)|n\rangle\langle n|, \quad \text{with} \\ p(n) &= \int_0^{|\alpha_0|} d^2|\alpha|\, \mathcal{P}(|\alpha|)\, e^{-|\alpha|^2}\, \frac{|\alpha|^{2n}}{n!}. \end{aligned} \tag{1.85}$$

where $p(n)$ is the photon number distribution function and $|\alpha_0\rangle$ is the diffracted coherent state at maximal transmittivity, and $\{|n\rangle\}$ is the Fock basis. The ensemble in Eq. (1.85) is practically realized by appropriately modulating the transmittivity of the input coherent state over a sufficient amount of time. The upper limit of $\hat{\rho}$ can be taken as infinity if $|\alpha_0|$ is chosen to be much larger than the mean $|\alpha|$.

We experimentally generate light sources with two specific PNDs as examples. The first is the thermal state with an average of $\bar{n}$ photons, namely, $\hat{\rho}_{\rm th}(\bar{n})$ [5] with

$$\mathcal{P}(|\alpha|) \equiv \mathcal{P}_{\rm th}(|\alpha|) = \frac{1}{\bar{n}\pi} \exp(-|\alpha|^2/\bar{n}), \tag{1.86}$$

for which the probabilities

$$p_{\rm th}(n) = (1 - e^{-\lambda})e^{-\lambda n} \quad \text{with} \quad \mathrm{e}^{-\lambda} = \bar{\mathrm{n}}/(\bar{\mathrm{n}} + 1), \tag{1.87}$$

define the PND. The second is the state $\hat{\rho}_\zeta$ corresponding to

$$\mathcal{P}(|\alpha|) \equiv \mathcal{P}_\zeta(|\alpha|) = \zeta^2|\alpha|^2 \exp[-\zeta|\alpha|^2], \tag{1.88}$$

with an average number of photons $\bar{n}$ and a PND specified by the probabilities

$$p_\zeta(n) = \left(\frac{\zeta}{\zeta+1}\right)^2 \frac{n+1}{(\zeta+1)^n}. \quad \text{with} \quad \zeta = \frac{2}{\bar{\mathrm{n}}}. \tag{1.89}$$

Note that the state $\hat{\rho}_\zeta$ is manifestly non-Gaussian.

The temporal coherence characteristics of the incoherent light with tailored PNDs, as generated above, is described by the second-order correlation function $G^2(\tau)$, given by

$$G^2(\tau) = 1 + (G^2(0) - 1)\xi(\tau) \tag{1.90}$$

where $\xi(\tau)$ is as given in Eq. (1.83). $G^2(0) = 2$ for $\mathcal{P}_{\rm th}(|\alpha|)$, $G^2(0) = 1.5$ for $\mathcal{P}_{\zeta}(|\alpha|)$ and $G^2(0) = 1$ for a coherent state.

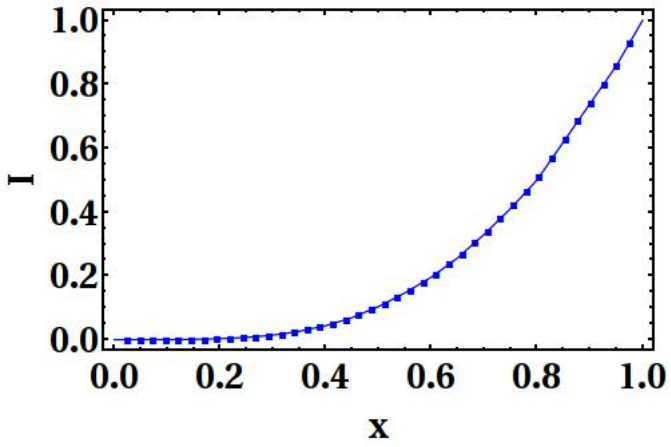

FIGURE 1.10: Calibration curve for AOM transmittivity in the first order diffracted beam w.r.t. RF power fed to the AOM. I in the y-axis is normalized transmittance i.e. ratio of transmitted intensity at a given RF power to maximum transmitted intensity at maximum RF power, ($I = I/I_{max}$). X along the x-axis is normalized RF power i.e. $X = P/P_{max}$

1.4.2 Experimental Results

For this part of the experiment AOM1 of Fig. 1.8 was switched off and BS2 was removed. Thus, only the light emerging from AOM2 could reach the detectors, which in this case were APD based SPCMs, as described previously. The input laser beam was attenuated using neutral density filters to produce at most 94000 counts per second (cps) on the APD, suitable for measurement in the photon counting regime [2]. The transmittivity of the AOM2 is calibrated for different rf power fed to the AOM. Fig. 1.10 shows the calibration curve for normalized transmittance of the AOM (for the 1^{st} order) w.r.t. normalized input rf power.

For the photon number distribution measurement in this section a time bin of $450\,\mu$s is set for the counter. The size of the time bin, which determines the average photon number, was so chosen for the PND measurements to clearly bring out the distinction between coherent and

[2] It may be noted that at these count rates the probability of two or more photons generating a single avalanche signal (including the dead time) is negligible, and thus we could reconstruct theoretically expected PNDs for strongly attenuated continuous laser light

incoherent states of various parameters. Once chosen, this time bin was fixed for all PND determinations. All measurements lasted for a period of at least 30 minutes, and multiple runs were carried out to obtain good statistics.

Initially, no noise was added to the rf signal and the maximum rf power was fed to the AOM; the $+1^{st}$ order diffracted light in this situation constitutes the maximally transmitted coherent state $|\alpha_0\rangle$. The PND for this light, as obtained from our measurements, is as shown in Fig. 1.11(a).

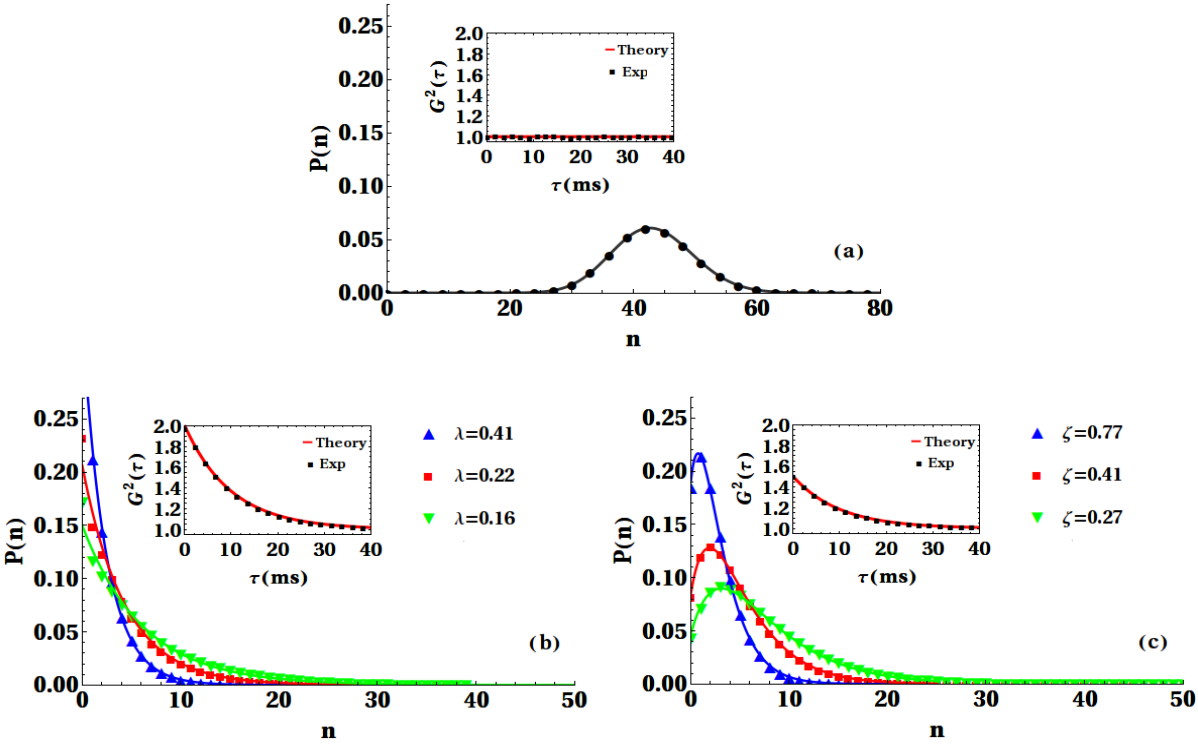

Figure 1.11: Photon number distributions, p(n) vs n, as determined from the experiment, with a time bin of 450μs, for (a) maximally diffracted laser light, in absence of input fluctuations; (b) light obtained with Gaussian amplitude noise (Eq. 1.86) applied to the rf, for different values of λ; (c) light obtained with non-Gaussian amplitude noise (Eq. 1.88) applied to the rf, for different ζ. Insets show the corresponding $G^2(\tau)$ as function of τ.

It has a Poissonian distribution with a mean photon number of 42 with an estimated average dark counts 2.25×10^{-2} per time bin, which is three orders of magnitude smaller than the average photon number in any of our experimental observations. The second-order correlation function, $G^2(\tau)$ for this case is shown in the inset; it is clearly that of a coherent state with $G^2(\tau) = 1$ for all τ. This was calculated directly from the recorded time series of the counter operating at $30\,\mu$s.

Using the calibration of the AOM transmittivity into the $+1^{st}$ order versus the rf power, and the experimentally determined value of $\bar{n}$ for the maximally transmitted coherent state $|\alpha_0\rangle$, we generate, by appropriate modulation of rf power, light with the desired photon number distribution function. The rf power was fluctuated at random time intervals in the range 1 to 100 ms with a mean time of ~ 10 ms, with the distribution of time intervals falling exponentially.

Then the rf power fed to the AOM was varied such that the transmitted coherent state $|\alpha\rangle$ was modulated to realize $\mathcal{P}_{\rm th}(|\alpha|)$ of Eq. 1.86, for three different values of $\bar{n}$ (1.91, 3.85 and 5.67) [3]. The emergent light was found to have the PNDs as shown in Fig. 1.11(b). These are in good agreement with the theoretically expected curves given by Eq. 1.87 for $p_{\rm th}(n)$. The second-order correlation function for this case is shown in the inset. The zero-delay second-order correlation has a value 2, as expected for thermal light. This shows that temporal modulation of intensity of coherent light leads to the bunching of photons. On similar lines, the rf power fed to the AOM was varied such that the transmitted coherent state $|\alpha\rangle$ was modulated to realize the non-Gaussian function $\mathcal{P}_{\zeta}(|\alpha|)$ of Eq. 1.88 for three different values of $\bar{n}$ (2.60, 4.88 and 7.41) [4]. The PNDs obtained for the emergent light are shown in Fig. 1.11(c), along with the theoretically expected curves given by Eq. 1.89 for $p_{\zeta}(n)$. The second order correlation function is shown in the inset. The zero-delay second-order correlation has a value 1.5, as expected for this case. The good agreement between theory and experiment for all measurements, both Gaussian and non-Gaussian, underlines the reliability and efficacy of this method in generating tailored classical light sources with desired PND and temporal coherence characteristics. Generation of classical non-Gaussian states with desired PND in a predetermined manner promises to be useful in various contexts as discussed in the next section.

1.5 Application of classical non-Gaussian state in quantum optics

As our method offers complete flexibility of providing phase and/or intensity fluctuations with different desired probability distributions and on different time scales, the AOMs can be used

[3] $e^{-\lambda} = \frac{\bar{n}}{\bar{n}+1}$
[4] $\zeta = \frac{2}{\bar{n}}$

to generate classical incoherent light having properties quite different from the existing light sources, opening up new fields for exploration. For example it is a simple matter to produce light with temporal incoherence but spatial coherence. This is a crucial requirement in experiments involving photon addition/subtraction to incoherent light[15] and this AOM-based technique is likely to find immediate application here. Another feature, likely to prove useful, is the ability to control the mean photon number with ease, even during the course of a measurement, by electronic means. This has been illustrated in Fig. 1.11(b) and 1.11(c), where we have changed the parameters λ and ξ to alter the mean photon number.

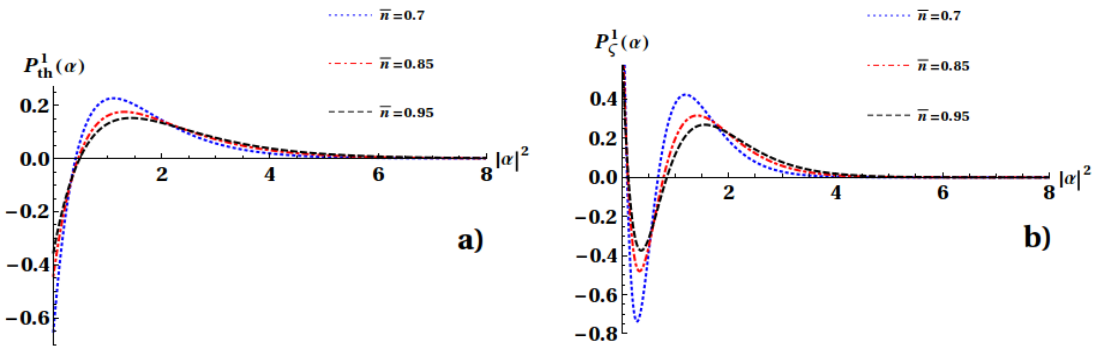

FIGURE 1.12: The distribution function $\mathcal{P}(|\alpha|)$ for photon added thermal state, ρ^1_{th}, (Fig. a)) and photon added classical non-Gaussian state, ρ^1_{ζ} (Fig. b)) given by Eq. 1.88. The plots for three different values of average photon number are given for each case. Note the qualitative difference between the two states for same average photon number.

1.5.1 Non-classical behaviour of photon added classical non-Gaussian state

A significant application of the tailored classical non-Gaussian states generated by this method is in the creation of tailored non-classical non-Gaussian states, for example when used in conjunction with the photon addition technique. As shown for thermal state in the section 1.2.6, we now consider the photon-addition on the non-Gaussian classical state given by Eq. 1.88. The photon added state can be represented by $\hat{\rho}^1_{\zeta} = \frac{1}{N_2}\,\hat{a}^{\dagger}\,\hat{\rho}_{\zeta}\,\hat{a}$, where the superscript 1 indicates that we have added one photon, and N_2 is an appropriate normalization constant. The non-classical properties

of the photon added non-Gaussian state can be analysed in terms of Glauber-Sudarshan's diagonal weight functions [5]. The diagonal weight function of this state can be calculated by using the technique described in section 1.2.6. The single photon addition operation on the non-Gaussian state, given by Eq. 1.88 can be written as follows

$$\hat{\rho}_{\zeta}^{1} = \frac{1}{N_2}\, \hat{a}^{\dagger}\, \hat{\rho}_{\zeta}\, \hat{a} \tag{1.91}$$

Here the superscript 1 indicates that we have added one photon, and N_2 is an appropriate normalizations. The density matrix of photon added non-gaussian state is

$$\hat{\rho}_{\zeta}^{1} \propto \int a^{\dagger} \left[\zeta^2 |\alpha|^2 e^{-\zeta|\alpha|^2} |\alpha\rangle\langle\alpha|\right] a\, d^2\alpha \tag{1.92}$$

using the property (see Appendix:-A)

$$a^{\dagger}(|\alpha\rangle e^{|\alpha|^2/2}) = \frac{\partial}{\partial\alpha}(|\alpha\rangle e^{|\alpha|^2/2}), \tag{1.93}$$

density matrix reads as

$$\hat{\rho}_{\zeta}^{1} \propto \int \zeta^2 |\alpha|^2 e^{-\zeta|\alpha|^2} \frac{\partial}{\partial\alpha}(|\alpha\rangle e^{|\alpha|^2/2}) \frac{\partial}{\partial\alpha^*}(\langle\alpha| e^{|\alpha|^2/2})\, d^2\alpha \tag{1.94}$$

Now integrating by parts and using the boundary condition for $|\alpha\rangle$

$$\hat{\rho}_{\zeta}^{1} \propto \int \left[e^{|\alpha|^2} \frac{\partial^2}{\partial\alpha\partial\alpha^*} \zeta^2 |\alpha|^2 e^{-\zeta|\alpha|^2}\right] |\alpha\rangle\langle\alpha|\, d^2\alpha. \tag{1.95}$$

Comparing Eq. 1.95 to the Eq. 1.37, the distribution function $\mathcal{P}(\alpha)$ for single photon added non-Gaussian state is

$$\mathcal{P}_{\zeta}^{1}(|\alpha|) \propto \left[\bar{n}^2 - 3\bar{n}(\bar{n}+2)|\alpha|^2 + (\bar{n}+2)^2|\alpha|^4\right] e^{-\frac{2}{\bar{n}}|\alpha|^2} \tag{1.96}$$

After normalization, the final expression for Glauber-Sudarshan diagonal weight function is

$$\mathcal{P}_{\zeta}^{1}(|\alpha|) = \frac{4}{\pi\, \bar{n}^4(1+\bar{n})} \left[\bar{n}^2 - 3\bar{n}(\bar{n}+2)|\alpha|^2 + (\bar{n}+2)^2|\alpha|^4\right] e^{-\frac{2}{\bar{n}}|\alpha|^2}, \tag{1.97}$$

Therefore the diagonal weight function for photon added thermal and photon added non-Gaussian states are as follows

$$\begin{aligned} \mathcal{P}_{\rm th}^{1}(|\alpha|) &= \frac{1}{\pi\, \bar{n}^3} \left(|\alpha|^2(1+\bar{n}) - \bar{n}\right) \exp[-|\alpha|^2/\bar{n}], \\ \mathcal{P}_{\zeta}^{1}(|\alpha|) &= \frac{4}{\pi\, \bar{n}^4\,(1+\bar{n})} \left(\bar{n}^2 - 3\bar{n}(\bar{n}+2)|\alpha|^2 + (\bar{n}+2)^2|\alpha|^4\right) \times \\ &\quad \exp[-2|\alpha|^2/\bar{n}], \end{aligned} \tag{1.98}$$

with $\zeta = \frac{2}{\bar{n}}$ for the latter. As is well known, any state with a point wise non-positive diagonal weight function is nonclassical (quantum). Clearly, both the weight functions in Eq. (1.98) correspond to the nonclassical states, and this is made manifest in Figs. (1.12). Further the nonclassicality (quantumness) of the states $\hat{\rho}^1_{\rm th}$ and $\hat{\rho}^1_\zeta$ are qualitatively different. To make this observation quantitative, we now evaluate the Mandel parameter Q for these states with respect to the mean number of photons. The Mandel parameter Q of a state $\hat{\rho}$ is defined as $Q = (\mathrm{Tr}(\hat{\rho}\,\hat{a}^{\dagger 2}\hat{a}^2) - (\mathrm{Tr}(\hat{\rho}\,\hat{a}^\dagger\hat{a}))^2)/\mathrm{Tr}(\hat{\rho}\,\hat{a}^\dagger\hat{a})$ [41].

Mandel parameter for $\hat{\rho^1_\zeta}$

For single photon added non-Gaussian state, $\hat{\rho^1_\zeta}$, Q can be calculated as follows.

$$\langle \hat{a}^{\dagger 2}\hat{a}^2\rangle = \int \mathcal{P}(|\alpha|)|\alpha|^4 d^2\alpha \tag{1.99}$$

From Eq. 1.99, and converting the equation into polar co-ordinates with $|\alpha| = |re^{i\theta}| = r$

$$\langle \hat{a}^{\dagger 2}\hat{a}^2\rangle = \frac{4}{\pi\bar{n}(1+\bar{n})}[2\pi(\bar{n}^2\int_0^\infty r^5 e^{-\frac{2r^2}{\bar{n}}}dr - 3\bar{n}(\bar{n}+2)\int_0^\infty r^7 e^{-\frac{2r^2}{\bar{n}}}dr + (\bar{n}+2)^2\int_0^\infty r^9 e^{-\frac{2r^2}{\bar{n}}}dr)] \tag{1.100}$$

where the factor 2π comes from the integration over θ. Using the value of definite integration,

$$\int_0^\infty r e^{-\frac{2r^2}{\bar{n}}}dr = \frac{\bar{n}}{4} \tag{1.101}$$

and taking the partial derivative of this with respect to $\bar{n}$ all other integrals can be evaluated, to obtain

$$\langle \hat{a}^{\dagger 2}\hat{a}^2\rangle = \left(\frac{\bar{n}}{\bar{n}+1}\right)\left[3\bar{n}^2 + \frac{15}{2}\bar{n} + 4\right] \tag{1.102}$$

Similarly one can calculate $\langle \hat{a}^\dagger\hat{a}\rangle$ to get,

$$\langle \hat{a}^\dagger\hat{a}\rangle = \frac{1}{1+\bar{n}}\left[\frac{3}{2}\bar{n}^2 + 3\bar{n} + 1\right] \tag{1.103}$$

The Mandel parameter from Eq. 1.58 can be written as

$$Q = \frac{0.75\bar{n}^4 + 1.5\bar{n}^3 - 0.5\bar{n}^2 - 2\bar{n} + 1}{(1+\bar{n})(1.5\bar{n}^2 + 3\bar{n} + 1)} \tag{1.104}$$

As any state with $Q < 0$ is definitely non-classical (quantum), it is clear from Fig. (1.13) that both $\hat{\rho}^1_\zeta$ and $\hat{\rho}^1_{\rm th}$ show non-classical behaviour for certain range of values $\bar{n}$. More interestingly, there are physical situations in which Q of $\hat{\rho}^1_\zeta$ is < 0 while Q of $\hat{\rho}^1_{\rm th} > 0$ for the same mean no. of photons. This suggests tailoring the non-Gaussianity of a classical state can have a direct bearing on the quantum features that may emerge when such a state is subject to further quantum processing.

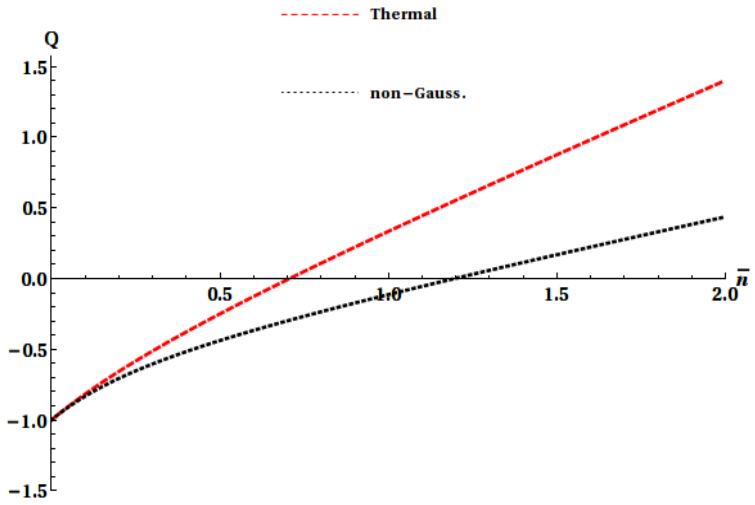

FIGURE 1.13: The figure shows the difference in the non-classicality behaviour ($Q < 0$) for the two different photon added states, one with thermal ρ^1_{th} and other with non-Gaussian state ρ^1_ζ. For the same mean photon number ρ^1_ζ shows more negativity compared to state ρ^1_{th}. Even more interestingly for mean photon numbers where ρ^1_{th} is classical ($Q > 0$), ρ^1_ζ still continues to be non-classical even upto average photon number $\bar{n} = 1$.

1.5.2 Generation of non-Gaussian Entanglement

Here we show how the tailored PNDs of the kind generated above may be used for producing novel forms of entanglement.

As is well known, a beamsplitter preserves non-Gaussianity [42], and non-classicality [5, 43]. It also generates entanglement of input non-classical states [44]. These features of the beamsplitter

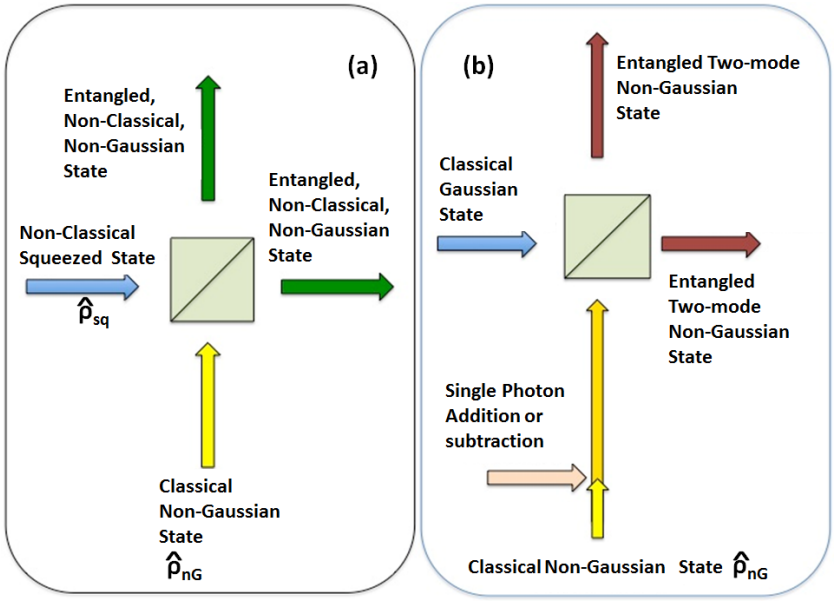

FIGURE 1.14: Two possible scenarios for the generation of tailored (a) entangled non-classical non-Gaussian state by mixing tunable classical non-Gaussian state with non-classical squeezed state or (b)entangled non-classical non-Gaussian state by mixing tunable single photon added non-Gaussian state with a classical Gaussian state on a beam splitter.

may be utilized to create non-Gaussian entangled states [24] of the form

$$\hat{\rho}_{\rm out}^{\rm nG} = U_{bs}\left(\hat{\rho}_{\rm G} \otimes \hat{\rho}_{\rm nG}\right) U_{bs}^{\dagger}, \tag{1.105}$$

by appropriately choosing a Gaussian state $\hat{\rho}_{\rm G}$ and a tailored non-Gaussian state $\hat{\rho}_{\rm nG}$. Here U_{bs} is the beamsplitter unitary.

Consider the situation shown in the Fig. 1.14 where a single-mode squeezed state $\hat{\rho}_{\rm sq}$ enters one port of a 50:50 beamsplitter and a tailored non-Gaussian state $\hat{\rho}_{\rm nG}$ enters the other. Note that here we may also tailor the non-classicality of $\hat{\rho}_{\rm nG}$ through processes such as photon-addition Fig. 1.14 (b). Let $V = \text{diag}\,\frac{1}{2}(e^{\mu}, e^{-\mu})$ denote the variance matrix of the squeezed state with squeezing parameter μ, and $\hat{\rho}_{\rm nG}$ the tailored non-Gaussian state with average photon number $\bar{n}$. The resultant state at the output of the beamsplitter is definitely entangled when $2\bar{n}+1 < e^{\mu}$ [45], while also remaining non-Gaussian. Clearly, this a realization of a non-Gaussian entangled state. The method is effective even if the initial non-classicality were to purely reside in $\hat{\rho}_{\rm nG}$. For instance, say $\mu = 0$ ($\hat{\rho}_{\rm G}$ is the ground state), and $\hat{\rho}_{\rm nG}$ is a photon-added tailored non-Gaussian

PND, the resulting $\hat{\rho}_{\rm out}^{nG}$ is definitely non-Gaussian entangled [46]. In other words, we may choose the initial non-classicality to reside either in $\hat{\rho}_{\rm G}$ or in $\hat{\rho}_{\rm nG}$, or in both of them, while simultaneously tuning the non-Gaussianity of $\hat{\rho}_{\rm nG}$, to generate the desired non-Gaussian entanglement.

1.6 Conclusion

To conclude, we have experimentally demonstrated a method for the creation of incoherent classical light using AOMs where the temporal characteristics, coherence time, photon number distribution function and the mean photon number are electronically tuned. Pseudo-thermal light and non-Gaussian classical light have been created from coherent laser light, as illustrative examples. Possible applications of such tailored light sources, like the generation of tailored non-Gaussian non-classical state as well as tailored non-Gaussian entanglement, have been discussed. The present proof-of-principle experiments, which display fluctuations on the milliseconds timescales, may be easily augmented with currently available technology to higher speeds (nanosecond timescales) and may be combined with techniques of photon addition, to create novel forms of non-classical light.

2

Chapter 2

2.1 Classical Light Analogue of the non-local Aharonov-Bohm effect :

This chapter is devoted for the experimental demonstration of non-local geometric phase also known as Pancharatnam phase for classical incoherent light in the intensity-intensity correlations. Existence of nonlocal Pancharatnam phase in two-photon interferometry was proposed by Mehta et. al. [47], for a pair of bunched or correlated photons in a Hanbury-Brown-Twiss experiment. When light from two thermal light sources with different circular polarization states is allowed to fall on two detectors which have polarizers in front of them, they show a geometric phase effect for correlated photons only in the cross correlation measurement of the two detectors but a null effect for local measurements on individual detectors[13]. Interestingly we demonstrate this effect with tailored classical phase-incoherent light. This effect for a classical incoherent light can be

thought of as a classical light analogue of the non-local Aharonov-Bohm effect [2].

In the experiment two independent phase incoherent light sources are generated by imparting phase noise to continuous coherent light, using acousto-optic interaction. The two-photon Pancharatnam phase was observed and modulated in a Mach-Zehnder interferometer.

2.1.1 Introduction

Two classic interference experiments are Young's double-slit experiment and the Hanbury Brown and Twiss (HB-T) experiment. The former measures the amplitude-amplitude correlation and demonstrates the interference of a photon with itself. The latter experiment measures the intensity-intensity correlation and is a demonstration of the interference of a pair of photons with itself. While the HB-T intensity-interferometry experiment was historically important in leading to our present understanding of quantum optics and coherence, one does not need to invoke quantum mechanics to understand it; it can quite simply be understood entirely in terms of classical electric field fluctuations. In recent times, with the development of different types of light sources and detection techniques, intensity-interferometry has, once again, become a topic of great interest. It has led to many tantalizing ideas and interesting applications[48–52]. There has been enormous debate [53–56] on the similarities and differences between bi-photon interferometry and two-photon interferometry. Bi-photon interferometry [57–59] uses entangled photon pairs that are related due to a conservation principle, for example, product photons in parametric down-conversion. Two-photon interferometry [60], on the other hand, involves photons that are statistically correlated, as from a thermal source; the experiment presented in this chapter belongs to this category. Intensity-interferometry with classical light is regaining importance with the demonstration of ghost imaging with thermal light [9, 55, 61].

A classical HB-T experiment consists of two slits, each illuminated by an independent, incoherent light source. Two detectors measure the intensity of light falling on them; at each detector, the intensity has contributions from both slits. The cross correlation of the intensities at the two detectors varies in a sinusoidal fashion as a function of separation between the detectors. In the conventional HB-T experiment, the appearance of these fringes was a purely dynamical effect, arising from the change in the path difference of the two detectors from the two slits. Recently

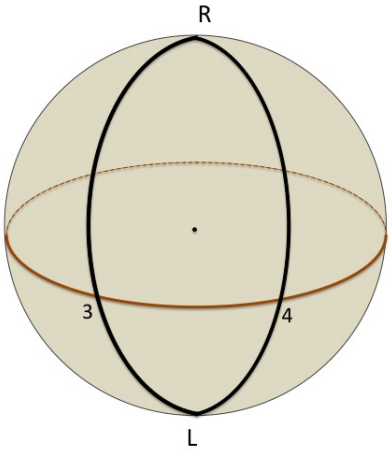

Figure 2.1: The Poincaré sphere. Figure shows four points on the Poincaré sphere representing two circular polarization states (R, L) and two linear polarization states of the two polarizers in front of the two detectors $(3, 4)$. The geometric phase is given by half the solid angle subtended at the center, by the geodesic polygon R-4-L-3-R.

it was shown theoretically [62] that even with fixed detectors, one can have such fringes if the sources and detectors are polarized and the polarization is varied. This effect is purely a geometric or Pancharatnam phase effect [63, 64] and arises due to the closed trajectory of polarized light on the Poincaré sphere. While such geometric phase effects are well known in amplitude interferometry, their counterparts in intensity interferometry have been less studied. The geometric phase is given by half the solid angle subtended by a closed path traced out by polarizing elements on the Poincaré sphere (see Fig. 2.1). Unlike the dynamical phase shift that is restricted by the spatial and temporal coherence of the sources, the geometric phase, is achromatic and unbounded, as later discussed in the chapter.

In this chapter, the following points are conveyed. We have used a classical phase incoherent light with exactly tailored characteristics. This is achieved by creating radio-frequency electrical signals of the desired features and imprinting this onto light via acousto-optic interaction. We show that a small modification to the HB-T intensity interferometry experiment leads to an optical analogue of the multiparticle Aharonov-Bohm effect [65]. This manifests as a non-local geometric phase in the intensity-intensity correlations of classical incoherent light, that is not seen in the lower order correlation. Finally, we show that this non-local two-photon cross-correlation

can be modulated via the geometric phase. This suggests a way of deflecting the cross-correlated photon pairs.

The Aharonov-Bohm effect for a pair of electrons has been considered theoretically by Samuelsson *et al* [65] and experimentally observed by Neder *et al*[66]. The experiment was essentially quantum in nature, as electrons, being fermions, do not admit the limit of large particle numbers. A pair of electrons together enclosed an Aharonov-Bohm flux due to an applied magnetic field, which was then used to modulate the two particle cross correlation via coupling to the orbital degree of freedom of electrons while the spin remained frozen. The effects of the flux were absent in the individual currents and in their self correlations while the cross correlation between electron currents revealed the dependence on the Aharonov-Bohm flux. In contrast to fermions, bosons permit macroscopic occupancy of a single state, admitting a classical limit and permitting a classical field theory description. The experiment that we report here uses classical light and is the classical bosonic analogue of the two-particle Aharonov Bohm effect. Here role of the Aharonov-Bohm flux is played by the geometric phase induced by polarization changes. As in the quantum case, the effect of the geometric phase is not seen in the individual intensities, nor the self-correlated intensities, but is seen only in the cross-correlation of intensities. Apart from the sign differences owing to the different statistics of the particles involved, the two effects are conceptually similar.

2.2 Aharonov-Bohm effect

Aharonov-Bohm effect which deals with fundamental properties of the electromagnetic field in quantum domain and the significance of the electromagnetic potentials in the quantum theory, was first theoretically suggested by Aharonov and Bohm in 1959 [67]. According to this there is a change in the phase of the wavefunction of a charge particle in a region where electromagnetic fields are absent but the electromagnetic potentials are non-zero. The effect of this phase change can be seen by a shift in the interference pattern of the *coherent* electron beam passing through the double-slit experiment or a Mach-Zehnder interferometer as shown in the Fig 2.2. During the traverse of the electron through the interferometer, electromagnetic potentials are non-zero but fields are absent.

The two most simple forms of the AB-effect are the magnetic AB-effect and the electric AB-effect. For the case of magnetic AB effect, a coherent electron beam passes through the two different paths in a region where there is no field and only a non-zero vector potential is present. The two beams acquire different phases in their wavefunction. This effect is observed in the interference of these two beams, which shows a fringe shift in their interference pattern Fig 2.2.

The wave function of the electron can be written as

$$\Psi = |\Psi| \exp(\frac{i}{\hbar} \overrightarrow{p} \cdot \overrightarrow{r}) \tag{2.1}$$

Here $\overrightarrow{p}$, which is momentum of the charge particle, in the presence of electromagnetic field is

$$\overrightarrow{p} = \overrightarrow{p} - e\overrightarrow{A} \tag{2.2}$$

The change in phase over the trajectories is given by

$$\begin{aligned} \Delta\delta = \frac{e}{\hbar} \oint_{2\to 1} \overrightarrow{A} \cdot \overrightarrow{r} \\ = \frac{e}{\hbar} \Phi, \end{aligned} \tag{2.3}$$

where $\Phi = \int \overrightarrow{B}.\overrightarrow{ds}$. Therefore the fringe shift is

$$\Delta x = \frac{L\lambda}{d} \Delta\delta$$

The electric AB effect can be observed in a Mach-Zehnder interferometer, where the two arms of the interferometer carry the electrons through conducting cylinders (Fig 2.2) that shield the electron from electric field (Faraday Cage). First experimental demonstration of this effect was shown by Chambers et. al.[68] . Potentials V_1 and V_2 are applied to the two conductors in a time delayed arrangement such that the electron is in a time varying potential without being in a field. This is because electric field lines doesn't penetrate far from the edges of the tube, and nonzero potentials are applied only when electron is deep inside the cylinders (Fig 2.2). The Hamiltonian of the electron when its is inside the cage is

$$H = H_0 + V(t) \tag{2.4}$$

H_0 is the Hamiltonian when $V(t) = 0$ and H is the total Hamiltonian when time dependent potentials are applied to the cylinders given by $V(t) = e\phi(t)$.

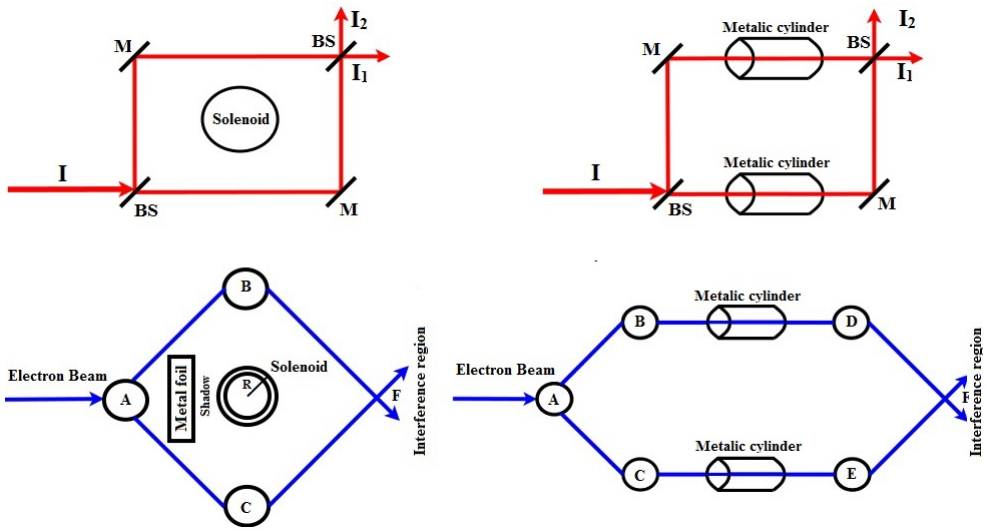

FIGURE 2.2: Schematic of the experiment to demonstrate AB-effect for coherent electron beam in a time-dependent vector potential due to solenoid and time-dependent scalar potential due to metallic cylinder. Two different but equivalent experimental geometries are shown for both the cases. A, B, C, D, E are suitable devices to split or divert the beams as required.

If the wavefunction of the electron is $\Psi(x,t)$, when potentials are zero, then

$$\Psi(x,t) = \Psi_1^0(x,t) + \Psi_2^0(x,t)$$

In the presence of time dependent potentials the wave function evolve as

$$\Psi(x,t) = \Psi_1^0(x,t)e^{-\frac{i\xi_1}{\hbar}} + \Psi_2^0(x,t)e^{-\frac{i\xi_2}{\hbar}} \tag{2.5}$$

where $\xi_1 = e\int \phi_1\, dt$ and $\xi_2 = e\int \phi_2\, dt$. It is obvious that interference at any point on the screen will depend on the phase difference $\propto \frac{\xi_1 - \xi_2}{\hbar}$.

This remarkable effect of electromagnetic potentials in a field free region, substantiated the reassessment of the importance of the electromagnetic field potentials in quantum physics, which in the case of classical mechanics was considered as a mathematical construct for more physical quantities E and B. Even though AB effect is purely a quantum mechanical phenomenon because the effect of phase shift is seen for a quantum wave, there are well known similar shift in the interference pattern of classical wave when an additional phase shift, in one of the slit is introduced, in a double slit interference setup.

The non-local nature of the AB effect :- The AB effect is seen for the electron even though it experiences no local classical Maxwell field parameter, because the Hamiltonian

$$H = \frac{1}{2m}(\overrightarrow{p} + \frac{e}{c}\overrightarrow{A})^2 - eV$$

contains the gauge field V and $\overrightarrow{A}$ which have non-zero values at some point of the closed circuit [69]. Ignoring the spin degree of the electron, the equation of motion for the observable is

$$\dot{\overrightarrow{r}} = \overrightarrow{v},\ m\dot{\overrightarrow{v}} = 0$$

This is of a free particle, containing no electromagnetic fields. So it is clear that in quantum mechanics the equation of motion alone doesn't determine the dynamics. Also in this case, electron doesn't experience force , exchanges no momentum, energy or angular momentum with the electromagnetic field. Thus the AB effect doesnot arise due to some local effect on electron's wave function but entirely a non-local effect arising due to presence of potentials in a closed trajectory.

Topological Effect:- The effect is topological because it depends upon the topology of the path with reference to the enclosed magnetic flux. If the electron is confined to a multiply connected region with non-zero field potentials, the shift in the fringe is the signature of the AB-effect. But there is no way to relate the phase shift to a particular place or the arm of the interferometer and the phase shift between two Feynman amplitudes depends only upon the difference between the topological winding numbers n of their paths [69],

$$\delta\phi = (\delta n)\frac{e\Phi}{\hbar C} \tag{2.6}$$

2.2.1 Multiparticle Aharonov-Bohm effect

In the previous section, the AB effect was described for a single quantum particle i.e. a coherent beam of electron was considered at the input. For input single particle states, which on the average are statistically uncorrelated and exhibit no direct interference, the AB effect couldn't be observed . Buttiker however had shown that a two-particle state can still be sensitive to a

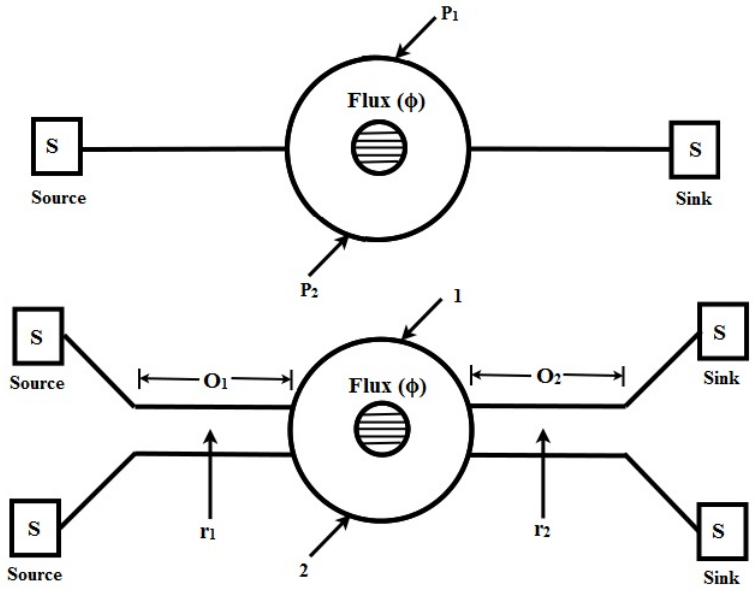

FIGURE 2.3: First figure shows direct interference when electron wave transmitted from source to sink is split into partial waves encircling the flux. Second figure shows the exchange interference when electron waves from two sources are transmitted from sources to sink without encircling the flux but with an overlap in regions O_1 and O_2.

magnetic flux and can exhibit two-particle AB effect even though single particle correlations are absent [70]. Consider an experimental set up as shown in the Fig 2.3, at the input the single particle wave function

$$\begin{aligned} \psi_1(r_1) &= e^{ik_1x_1}\chi_1(y_1) \\ \psi_2(r_1) &= e^{ik_2x_1}\chi_2(y_1) \end{aligned} \tag{2.7}$$

where $\chi_1(y)$ and $\chi_2(y)$ are the wave functions of the transverse motion which are quantized. At the output the wave function is

$$\begin{aligned} \psi_1(r_2) &= e^{ik_1x_2}\chi_1(y_2)e^{i\phi_1}e^{i\Theta_1} \\ \psi_2(r_2) &= e^{ik_2x_2}\chi_2(y_2)e^{i\phi_2}e^{i\Theta_2} \end{aligned} \tag{2.8}$$

where phase factor $\phi_{1,2}$ takes care for the extra path traveled along the arcs and

$$\Theta_{1,2} = \frac{e}{\hbar c}\int_{r_1}^{r_2} ds_{1,2}.A \tag{2.9}$$

is the phase due to AB flux. From above expressions it is clear that $|\psi_1|^2$ and $|\psi_2|^2$ are independent of the flux. However two particle wave function

$$\begin{aligned}\psi(r_1, r_2) &= \psi_1(r_1)\psi_2(r_2) - \psi_1(r_2)\psi_2(r_1) \\ &= e^{i\phi_0}[\chi_1(y_1)\chi_2(y_2) - \chi_1(y_2)\chi_2(y_1)e^{i\phi}] \end{aligned} \tag{2.10}$$

where

$$\phi_0 = k_1x_1 + k_2x_2 + \phi_2 + \Theta_2 \tag{2.11}$$

$$\phi = (k_1 - k_2)(x_2 - x_1) + (\phi_1 - \phi_2) + \Theta \tag{2.12}$$

It can be seen from here that single particle wave functions $|\Psi_{1,2}|^2$ are independent of flux $\Theta_{1,2}$ but two particle wave function depends on the flux through ϕ. The measure of correlation not contained in single particle correlation i.e. $\Delta W = |\Psi(r_1, r_2)|^2 - |\Psi_{1,2}|^2$ is given by

$$\Delta W\left(r_1, r_2\right) = -2\chi_1\left(y_1\right)\chi_2\left(y_2\right)\chi_1\left(y_2\right)\chi_2\left(y_1\right)\cos\phi \tag{2.13}$$

which depends on the flux due to exchange effect because in the two particle state one cannot distinguish between the charge carries which passes either upper or lower arc.

Further if the two sources are statistical mixture instead of well defined k_1 and k_2 , then it can be shown that the exchange interaction terms still survives under statistical averaging. Therefore in an HBT kind of detection system, the cross correlation between the two detectors shows modulation of the correlation function in the presence of magnetic flux. But the self correlations of the detector on either path doesnot show any correlation.

An analogue of the multi-particle AB-effect can be observed for bunched photons or incoherent light coming out of two independent sources with no first order correlation but with a modulation in the second order correlation value with a change in the geometry of the closed path over the Poincaré sphere, in a polarized HBT intensity-intensity interferometry [47]. This arises due to the extra geometric phase acquired by the correlated pair of photons over the closed cycle. Here the geometric phase induced by polarization changes plays the role of AB flux.

2.2.2 Geometric Phase and AB-effect

Berry phase or the geometric phase is the change in the phase of quantum state vector when the system after undergoing a sequence of adiabatic changes in the state vector space, comes

back to the original state. The phase acquired in the process depends on the geometry of the path and is therefore a geometric phase. AB-effect observed for charge particles like electrons is a special case of more general concept of Berry's phase [71]. Similar to the geometric phase, the phase acquired by light when it undergoes a sequence of changes in its polarization over the Poincaré sphere, was suggested in 1955 by Pancharatnam [63]. If a light beam is made to go through a closed cycle on the Poincaré sphere, which is the space of polarization states of light, it acquires a geometric phase which depends on the geometry of the closed cycle.

2.3 Interference Experiments: Polarization Interferometry and Pancharatnam phase

In a prominent work published by Pancharatnam in 1955 [63], he showed the non-trivial phase acquired by the light, in addition to *dynamical phase* from the accumulated path lengths, if it made to go through a cyclic changes in the state of its polarization. The amount of this extra phase shift depends upon the geometry of the cyclic path over the Poincaré sphere as shown in Fig. 2.1. Remarkably this was the earliest example of geometric phase in the context of light which was later developed by Berry [71, 72] in the context of quantum states. Pancharatnam's work is now seen as an early precursor to geometric phase in quantum mechanics [47].

For a completely polarized light, the state of the polarization is specified by the form of the ellipse traced by the tip of the displacement vector and can be represented in terms of the angular co-ordinates of a point over the three dimensional sphere known as Poincaré sphere. However a given state of polarization on the Poincaré sphere doesn't specify the phase of the vibration i.e. all states related by a phase factor maps to the same point on the sphere. Therefore phase is an extra quantity to be fixed to the points on the sphere. The specification of relative phase of the two coherent light beams, when they are in the two different state of elliptical polarization, is very crucial to predict the resultant interference of the two Beams. Pancharatnam developed a very powerful method based on axioms and theorems of spherical trigonometry and basic wave theory of light to calculate any kind of complicated interference of light beams.

Firstly the total phase difference between two coherent light beams, which are in different state

of polarization, is given by Pancharatnam connection. This phase difference is the total phase change applied to one of the beam to maximize the intensity of their superposition. If $|a\rangle$ and $|b\rangle$ are two different state of polarization then

$$\phi_T = \arg\langle a|b\rangle$$

Further he showed, if a state A is in phase with state B, and B is in phase with a third state C, then C need not be in phase with A. In fact if C is in phase with state A' represented by the same point A on the sphere then the phase factor accumulated after this cycle of polarization states, is the phase difference between A and A' and is given by [63]

$$\Delta\phi = \exp(-\frac{1}{2}\Omega_{abc})$$

where Ω_{abc} represents the solid angle subtended by the closed path on the sphere and depends on the geometry of the closed cyclic path.

2.4 Classical Light Analogue of the non-local Aharonov-Bohm effect:-

In this section a detailed description of our work [2] is presented.

2.4.1 Experimental setup

The experiment employs two phase-incoherent sources $S1$ and $S2$ in a Mach-Zehnder setup with birefringent elements and two polarized detectors $D3$ and $D4$ (see Fig. 2.4).

A variation of the relative polarization angle of the detectors introduces a geometric phase equal to half the solid angle enclosed by the two interfering paths on the Poincaré sphere (see Fig. 2.1). Light from a diode laser at 767nm was incident on a non-polarizing beam-splitter depicted as BS1 in Fig. 2.4, and the two emergent beams were passed through two acousto-optic-modulators (AOM) shown in Fig. 2.4 as AOM1 and AOM2 and fed by two radio frequency sources (RF1 and RF2) respectively. The first order diffracted beams emerging from the two AOMs were passed through two quarter-wave plates ($Q1, Q2$), to render one beam right circularly polarized

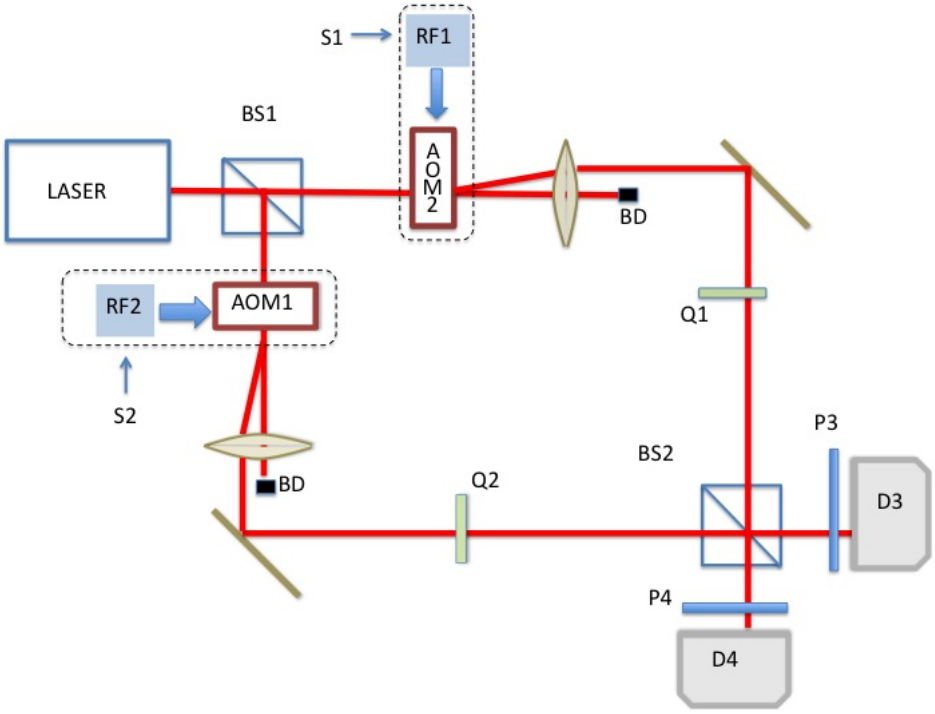

FIGURE 2.4: Figure shows a schematic diagram of the experimental setup. Two sources $S1$ and $S2$ illuminate two detectors $D3$ and $D4$ as explained in the text. $BS1$ and $BS2$ are non-polarizing beam splitters, $Q1$ and $Q2$ quarter wave plates, $P3$ and $P4$ linear polarizers and BD beam dumps

(R) and the other left-circularly polarized (L). The two beams were then combined at a non-polarizing beam splitter (BS2). At each exit face of the final beam splitter, a polarizer ($P3, P4$) was kept, followed by a detector ($D3, D4$). The undiffracted beam terminated in a beam dump (BD) as shown in Fig. 2.4. By keeping one of the polarizers (e.g., $P3$) fixed and changing the orientation of the other polarizer ($P4$), the relative angle between the polarizers, ϕ_{34} could be varied continuously from 0° to 360°. This results in a corresponding variation in the geometric phase. As we show below, this also causes a modulation of the intensity cross-correlation of the light reaching the two detectors. In order to measure this, the intensities of light reaching detectors $D3$ and $D4$, for each orientation of $P4$ was recorded for a certain length of time on a digital storage oscilloscope and cross correlated offline.

In striking contrast to the other interference experiments which require a source of coherent light, the two-photon intensity-interferometry needs incoherent sources as HB-T correlations vanish for a laser light source. One could use a thermal source such as a mercury vapor lamp.

However, the coherence time of natural thermal light sources is too short for bunching effects to be easily discernible by most present day solid-state photo-detectors. Two-photon interferometry experiments therefore usually simulate thermal light by passing laser light through a rotating ground-glass plate. This introduces, random intensity and phase fluctuations that occur at a time scale detectable by present day solid-state detectors. We employed a different technique of simulating incoherent light that utilizes acousto-optic interaction.

In an AOM, radio-frequency (RF) electrical signal is applied to create a travelling acoustic-wave grating that can diffract light. The frequency, intensity, and phase of light can be manipulated through the acousto-optic interaction by suitably tailoring the RF input to the AOM. In this experiment, however, only phase fluctuations were introduced. As demonstrated recently [73], an incoherent source may be created by electronically introducing random phase jumps to the RF and imprinting these onto laser light source. The phase evolves undisturbed for a time T, and then is changed by a random amount δ. The phase jump δ is uniformly randomly distributed over the circle and T has the distribution of a truncated exponential:

$$P(T) \;=\; \frac{1}{T_c} e^{-\frac{T}{T_c}} \;, \tag{2.14}$$

where $1\ \mu s < T < 100\ \mu s$, and $T_c = 10\ \mu s$. T_c represents the timescale over which the coherence of the light beam is lost. Such a distribution (in untruncated form) has been discussed [74] in connection with the emission of a single atom interrupted by collisions. Each AOM in the setup was independently phase modulated in this manner to derive two independent phase-incoherent sources from the same laser light.

2.4.2 Theory

Let E_j^α represent the electric fields associated with the electromagnetic waves emitted by sources 1 and 2. Here $j = 1, 2$ and the index α runs over the two polarization states. Light emitted by a source and received by a detector suffers propagation phases. These effects are captured by the functions u_{ij}, which represent the total dynamical phase in going from the source j ($j = 1, 2$) to

the detector i ($i = 3, 4$). With this notation, we express E_i^α and its Hermitean conjugate $\bar{E}_i^\alpha$ as

$$\begin{aligned} E_i^\alpha &= P_i^{\alpha\beta} \left[\epsilon_i P_L^{\beta\gamma} E_2^\gamma u_{i2} + P_R^{\beta\gamma} E_1^\gamma u_{i1} \right] \\ \bar{E}_i^\alpha &= \left[\bar{u}_{i2} \bar{E}_2^\gamma P_L^{\gamma\beta} \epsilon_i + \bar{u}_{i1} \bar{E}_1^\gamma P_R^{\gamma\beta} \right] P_i^{\beta\alpha} , \end{aligned} \tag{2.15}$$

where the overbar stands for complex conjugation; ϵ_i is a pure phase $\epsilon_3 = 1$, $\epsilon_4 = -1$ due to the geometry of the Mach-Zehnder setup. Note that 2×2 Hermitean projection matrices P satisfy $P^2 = P$ and $\bar{P}^{\alpha\beta} = P^{\beta\alpha}$.

The cross correlation is given by :

$$\mathcal{G}_{34}^2(\tau) = \frac{\langle I_3(\tau) I_4(0) \rangle}{\langle I_3 \rangle \langle I_4 \rangle} , \tag{2.16}$$

where $I_3(\tau)$ and $I_4(0)$ are the intensities measured at $D3$ at time τ and at $D4$ at time 0 respectively and the average $\langle \ldots \rangle$ is a time average over the integration time T_{int}:

$$\langle f \rangle = \frac{1}{T_{int}} \int_0^{T_{int}} f(t) dt \tag{2.17}$$

We calculate our final expression for the expected value of the second order correlation (Eq. 2.16) after computing the intensities ($I_i = \bar{E}_i E_i$) by squaring the electric fields. We obtain, for the intensity cross correlation at the two detectors (D3, D4)as described in ref.[47] :

$$\mathcal{G}_{34}^2(\tau = 0) = 1 - \frac{1}{2} \cos\left(\phi_D + \frac{\Omega}{2} \right) , \tag{2.18}$$

and for the intensity self correlation :

$$\mathcal{G}_{ii}^2(\tau = 0) = 1 + \frac{1}{2} \cos\left(\phi_D \right) , \tag{2.19}$$

where ϕ_D represents the dynamical phase (which, in our Mach-Zehnder interferometer has been adjusted to zero) and $\frac{\Omega}{2}$ is the geometric phase. Ω is the solid angle traced by a geodesic curve on a closed path over the Poincare sphere [63]. The negative sign for the second term (in Eq. 2.18) is due to the Mach-Zehnder configuration. Note that the geometric phase appears only in the intensity cross correlation (Eq. 2.18), and is absent both in the intensity self correlation (Eq. 2.19) and the lower order correlation ($\mathcal{G}_{ii}^1$; $i = 3, 4$) at each detector. This implies that this geometric phase is a purely nonlocal effect.

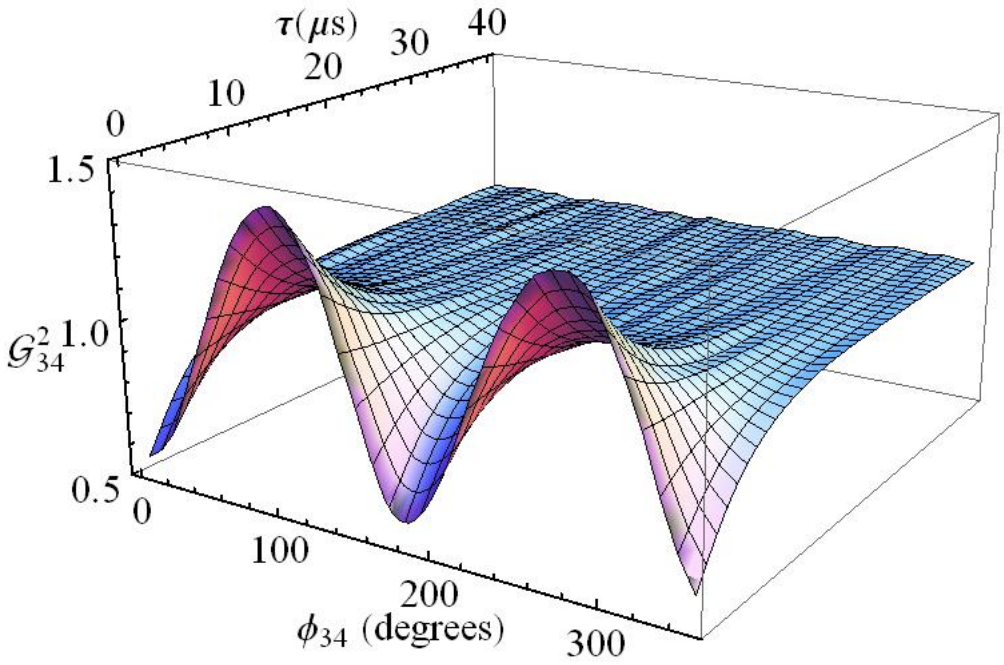

FIGURE 2.5: Figure shows the experimentally determined cross correlation, $\mathcal{G}^2_{34}$, as a function of ϕ_{34} the relative angle between the polarizers P_3 and P_4, and as function of time delay τ. Clearly, the cross correlation $\mathcal{G}^2_{34}$ is modulated by the geometric phase.

2.4.3 Experimental Results

The main results of our experiment are displayed in the three-dimensional plot of Fig. 2.5, which shows the quantity of interest, $\mathcal{G}^2_{34}$, as a function of the time delay, τ, and the relative angle, ϕ_{34}, between the linear polarizers $P3$ and $P4$ in front of the two detectors $D3$ and $D4$ respectively.

For zero delay ($\tau = 0$) between the two detectors, the cross correlation $\mathcal{G}^2_{34}$ was found to vary sinusoidally from ~ 0.5 to ~ 1.5 as ϕ_{34} is varied. Clearly, this is due to the geometric phase. For larger values of τ the amplitude of the sinusoidal variation is found to be progressively diminished, till finally, for for $\tau > T_C$, $\mathcal{G}^2_{34}$ remains nearly constant at 1, *i.e.,* correlations that are maximum for zero delay gradually decrease, and are absent for delays larger than the coherence time. At the regions of constructive interference (e.g. $\phi_{34} = 90°$), the value of $\mathcal{G}^2_{34}$ starts from 1.5 for $\tau = 0$ as is expected for a source with pure phase fluctuations [75]. Note that in regions of destructive interference, the cross correlation starts from 0.5, a value lower than that for a coherent source.

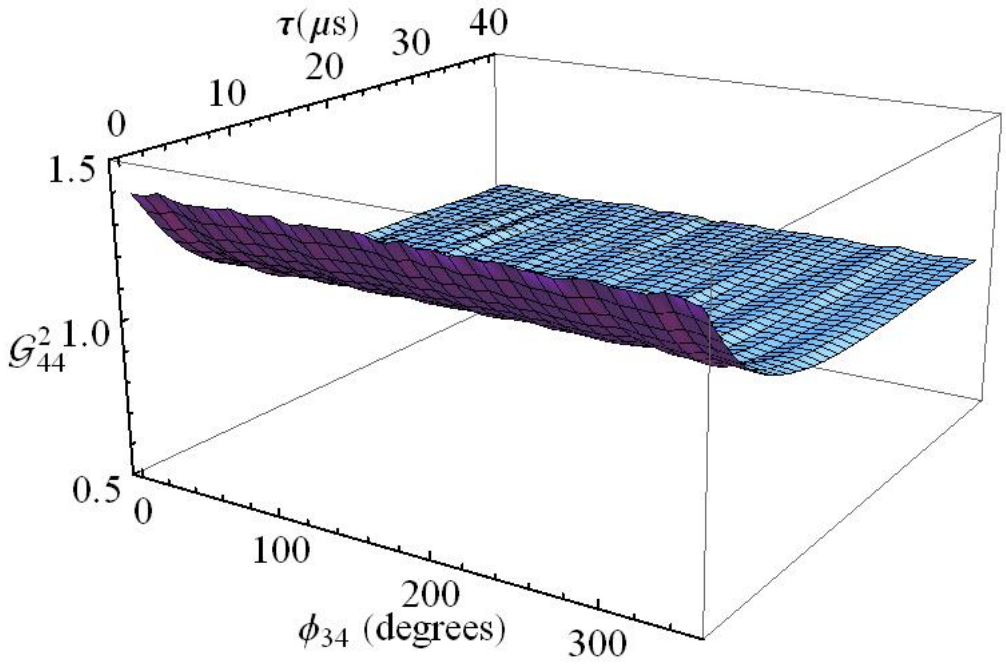

FIGURE 2.6: Figure shows the self correlation $\mathcal{G}^2_{44}$ as a function of ϕ_{34} the relative angle between the polarization angles of the two detectors, and of the time delay τ. Note that the self correlation ($\mathcal{G}^2_{44}$ is plotted) is independent of ϕ_{34} . Thus the geometric phase effect of Fig. 2.5 is a purely nonlocal effect.

This has been discussed in various contexts earlier [76].

In order to illustrate that it is a purely nonlocal effect we also plot in Fig. 2.6 the second order self correlation. In contrast to the cross-correlation, the self-correlation remains unaltered as the relative angle between the polarizers is varied. This may be easily understood by visualizing the trajectory on the Poincaré sphere - it is the arc connecting the three points $R, 4, L$ ($\mathcal{G}^2_{44}$) (or $R, 3, L$ ($\mathcal{G}^2_{33}$)). Two of the three points are antipodal (R and L are orthogonal states) and hence we do not expect a non-zero solid angle or geometric phase [63]. The first order correlation ($\mathcal{G}^1_{33}$) is also independent of variation of angle between polarizers in front of the two detectors.

2.4.4 Discussion

The experiment and the theoretical analysis presented here are purely classical. Interestingly, the earlier quantum mechanical treatment [62] too, predicted similar results, which have very recently been confirmed by intensity-interferometry using photon-counting techniques [77]. The classical

approach has the advantage that the physical ideas are easy to grasp. In fact, Hanbury Brown and Twiss were originally motivated by their classical experience with radio waves to propose the corresponding optical experiment. The quantum interpretation of this classically simple experiment led to profound changes in our understanding of quantum optics and coherence.

In addition to being completely in the classical domain, our experiment has another novelty. In the case of thermal or pseudo thermal light (*i.e.,* one with both phase and intensity fluctuations), $\mathcal{G}^2$ varies between 1 and 2. In contrast, for pure phase modulation, one expects a variation from 0.5 to 1.5. Baym, in his review article [75] that examines the $\mathrm{HB\text{-}T}$ effect in a wide variety of physical contexts ranging from nuclear physics to astronomy, had reached this conclusion in his discussion of the case of pure phase fluctuations. However, this has hitherto not been verified, as pure "phase-only" fluctuating sources have not been available. In our experiment, such a source has now been realized by tailoring fluctuations in light by the acousto-optic technique, and the result of Baym verified.

Two salient features of the geometric phase measured in our experiment are its purely non-local nature and its absence in the lower order correlation, in contrast to earlier works on geometric phase and intensity interferometry[78]. This suggests the possible application of the nonlocal Aharonov-Bohm effect as a two-photon deflector. We refer again to Fig. 2.4, where we now replace the polarizer P_4 by a "graded polarizer" - one where the axis of polarization changes in orientation gradually as one moves across the polarizer. In intensity interferometry this would introduce a geometric phase gradient. As is well known, a phase gradient in a wave is equivalent to a deflection or a change of wave vector. In the present experiment, the phase change appears *only* in the intensity cross correlations. Thus, we are able to generate a "two-photon deflector" which only affects pairs of $\mathrm{HB\text{-}T}$ correlated photons while leaving the remaining photons unaffected. Such a device may have applications in creating sources of correlated photons.

This section ends with a few classical remarks which may have interesting quantum interpretations.

Let us note that the geometric phase is unbounded. As one turns the polarizer $P4$, the geometric phase keeps accumulating without bound and the visibility of the interference pattern remains undiminished. This is in sharp contrast to the dynamical phase: as one increases the dynamical phase, by separating the detectors, the interference pattern is washed out when their

spatial (temporal) separation exceeds the coherence length (time). This difference is due to the fact that the geometric phase is achromatic and affects all frequencies equally. Thus the geometric phase effects are less susceptible to decoherence than the corresponding dynamical effects. This illustrates a point often made in the quantum computation literature that geometric and topological effects are robust against decoherence. This is crucial to the development of quantum computers.

At the level of classical information theory, our experiment can be interpreted as a way of delocalizing information. Consider the experimental setup above and make the following minor changes: We choose $P3$ and $P4$ to be orthogonal linear polarizations represented by antipodal points on the equator of the Poincaré sphere. We take the sources to be elliptically polarized and lying on the great circle orthogonal to the line joining the antipodal points 3 and 4. If the angle ϕ between the elliptical polarizations of the two sources is varied in time $\phi(t)$, one would find that there is a corresponding modulation in the cross-correlations of the intensities detected at $D3$ and $D4$. The signal $\phi(t)$ can be viewed as carrying information. However, the two beams emerging from the experiment are of fixed linear polarization, and beam by itself appears thermal in its self correlation. It is only by looking at their cross correlations that one can recover the originally impressed signal $\phi(t)$. Thus, in this example, information is stored in a completely delocalized manner. In quantum information theory, one presumes that it would be similarly possible to have apparently thermal beams carrying information entirely in their quantum cross correlations.

To summarize, we have demonstrated the existence of a non-local geometric phase in the intensity-intensity correlations of classical incoherent light, that is not seen in the lower order correlation. This two-photon Pancharatnam phase is the classical optical analogue of the multi-particle Aharonov-Bohm effect[66]. As the trajectory of light over the Poincaré sphere introduces a phase shift observable only in the intensity-intensity correlation, it provides a means of deflecting the two-photon wavefront, while having no effect on single photons. The experiments were performed using sources that had pure phase fluctuations. We expect that the results presented here will be of interest for applications in the realm of classical and quantum communication and cryptography.

2.5 $\mathcal{G}^2(\tau = 0)$ correlation modulation in cascaded polarized Interferometers

In this section the effect of cascading two or more interferometers of the type described in the section 2.4 is examined. The cascading of such interferometers can be used to modulate the zero delayed second order correlation function and values $\mathcal{G}^2(0) > 2$ can be obtained for phase incoherent light. Theoretically $\mathcal{G}^2(0) > 2$ value is expected for even a two stage interferometer and this can be modulated between a minimum value of $\mathcal{G}^2(0) = 0.75$ to a maximum value of $\mathcal{G}^2(0) = 2.25$. A numerical simulation of zero delayed second order correlation function and its comparison with the experimental results for a two stage polarised interferometer is presented in the following sections. The mathematical analysis of this can be done in terms of Jones matrices.

The Jones vectors (matrices) are useful tools to describe the polarization of light. The x- and y-components of the light with propagation along z-direction, is represented in terms of Jones vector,

$$\begin{pmatrix} E_x(t) \\ \\ E_y(t) \end{pmatrix} = E_0\, e^{i(kz-\omega t)}. \begin{pmatrix} E_{0x}e^{i\phi_x} \\ \\ E_{0y}e^{i\phi_y} \end{pmatrix}, \tag{2.20}$$

where

$$\begin{pmatrix} E_{0x}e^{i\phi_x} \\ \\ E_{0y}e^{i\phi_y} \end{pmatrix}, \tag{2.21}$$

is the Jones vector. It is clear that it represents relative amplitude and phase of the x- and y-component of electric field. The effect of different optical elements in the path of the propagation of the beam can be easily described by operation of the matrices corresponding to optical element on the Jones vector of the input field. The matrices corresponding to the three important optical elements relevant for this discussion are given.

The operation of the linear polarizer with the axis of transmission horizontal is,

$$L = \begin{pmatrix} 1 & 0 \\ 0 & 0 \end{pmatrix} \tag{2.22}$$

and the operation of the quarter wave plate with fast axis horizontal is,

$$Q = \begin{pmatrix} 1 & 0 \\ 0 & i \end{pmatrix}. \tag{2.23}$$

If the axis of the optical element is rotated about an angle Θ. Then the Jones matrix for the rotated element, $M(\Theta)$ can be derived from that of the unrotated element M, by the following transformation

$$M(\Theta) = R(\Theta)\ M\ R(-\Theta) \quad \text{where} \quad \mathrm{R}(\Theta) = \begin{pmatrix} \cos\Theta & -\sin\Theta \\ \sin\Theta & \cos\Theta \end{pmatrix} \tag{2.24}$$

For the purpose of this discussion an AOM may be thought of as a simple phase shifter and its operation can be represented as,

$$\Phi_{aom} = \begin{pmatrix} e^{i\Phi} & 0 \\ 0 & e^{i\Phi} \end{pmatrix} \tag{2.25}$$

2.5.1 Experimental Setup

As shown in the Fig. 2.7, a cascade of two Mach-Zehnder interferometers are used in the experiment. Each interferometer has an AOM along each of the arm. Two of the AOMs, AOM1 and AOM3, are driven by computer controlled VFG's operating at 80 MHz. Controlled random phase jumps, uniformly distributed between $(-\pi, \pi)$, can be introduced to them through labview

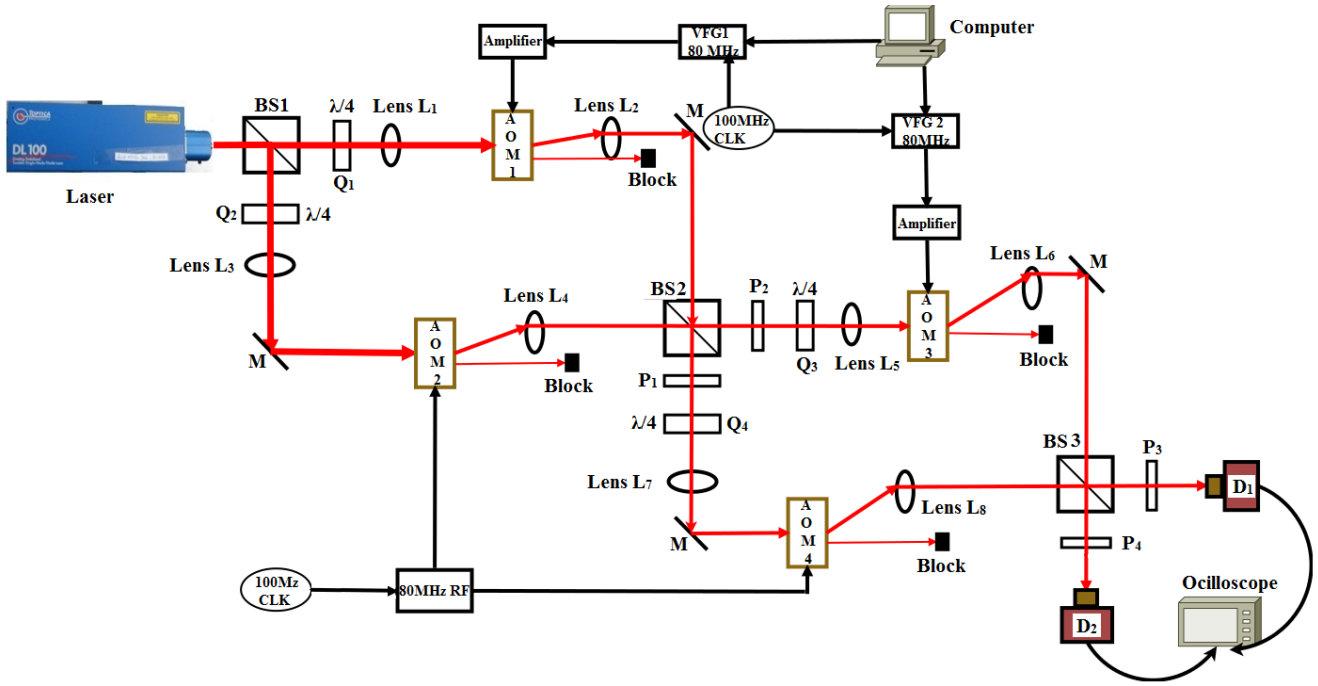

FIGURE 2.7: Figure shows the experimental setup of the two cascaded polarized interferometers. VFG1 and VFG2 are versatile function generator which generates rf signal. The phase, power and frequency of which can be computer controlled. $Q_1 - Q_4$ are the quarter wave plates, $P_1 - P_4$ are polarizers. BS1-BS3 are non-polarizing beam splitters.

interface . Other two AOMs, AOM2 and AOM4, are driven by fixed 80 MHz rf source. All the rf sources are referenced to a single external 10 MHz reference clock. Thus the phase incoherent light is generated by randomizing the phase of light passing through AOM1 and AOM3. Q1-Q4 are the four quarter wave plates to set opposite circular polarizations for the input incoherent light at each arm of the two cascaded interferometers. P1-P4 are the four polarizers which project the output beams in two different linear polarization states at the two output ports of the beam splitters.

Random phase noise is introduced to AOM1 and AOM3 which creates intensity fluctuations at the two output ports of the beam splitter BS2 and BS3. The relative angle between polarizers P1 and P2 is denoted by θ and that of P3 and P4 by ϕ. In the experiment θ is varied by rotating polarizer P_1 while polarizer P_2 is kept fixed. To maintain circular polarization the quarter wave plate Q_3 is rotated in the appropriate direction through same angle of rotation θ. At the final

output port polarizer P_3 is rotated while keeping P_4 constant to change the value of ϕ.

A comparison between the experimental and theoretical results for cross correlation and self correlation between the detectors is presented in the next section. The theoretical values are obtained by evaluating Jones matrix after polarizer P_3 and P_4, at the output port of the beam splitter BS3. From this, intensities at the detectors and hence the cross and self correlation is obtained.

Starting with horizontal polarized light with equal intensities at BS1 and applying matrix operation for different optical elements on it (as described in the previous section), final intensities at the two detectors are obtained. For each point corresponding to (θ, ϕ), this value is evaluated for a large ensemble of random phase values distributed between $(-\pi, \pi)$ corresponding to phase jumps, Φ (Eq. 2.25), imparted to the light by AOM1 and AOM3. The results obtained are as follows.

2.5.2 Results

The second order cross correlation between the detectors D_1 and D_2 is shown in the Fig 2.8. Both theoretical and experimental plots are shown along with their contour plots. Theoretically obtained maximum and minimum value of $\mathcal{G}^2(0)$ are 2.25 and 0.75. The maximum value of $\mathcal{G}^2(0)$ obtained in the experiment is 2.1. It can be seen from here that the $\mathcal{G}^2(0)$ can be modulated by varying θ and/or ϕ

The self correlation for individual detectors D_1 and D_2 are shown in the Fig. 2.9 and Fig. 2.10 respectively. The average value of intensities at individual detectors doesn't contain any information regarding the polarization changes of the light and remains almost constant as shown in the Fig. 2.11 and Fig. 2.12. Small changes are due to the imperfection in the retarder plates as well as instability of the interferometer due to external drifts.

2.5.3 Conclusion

The cascaded version of the polarized interferometer, as shown in the experiment, can be utilized to modulate the zero delayed second order correlation function of the light emerging through the output ports. Indeed superbunched light with $\mathcal{G}^2(0) > 2$ may be generated. Enhanced bunching

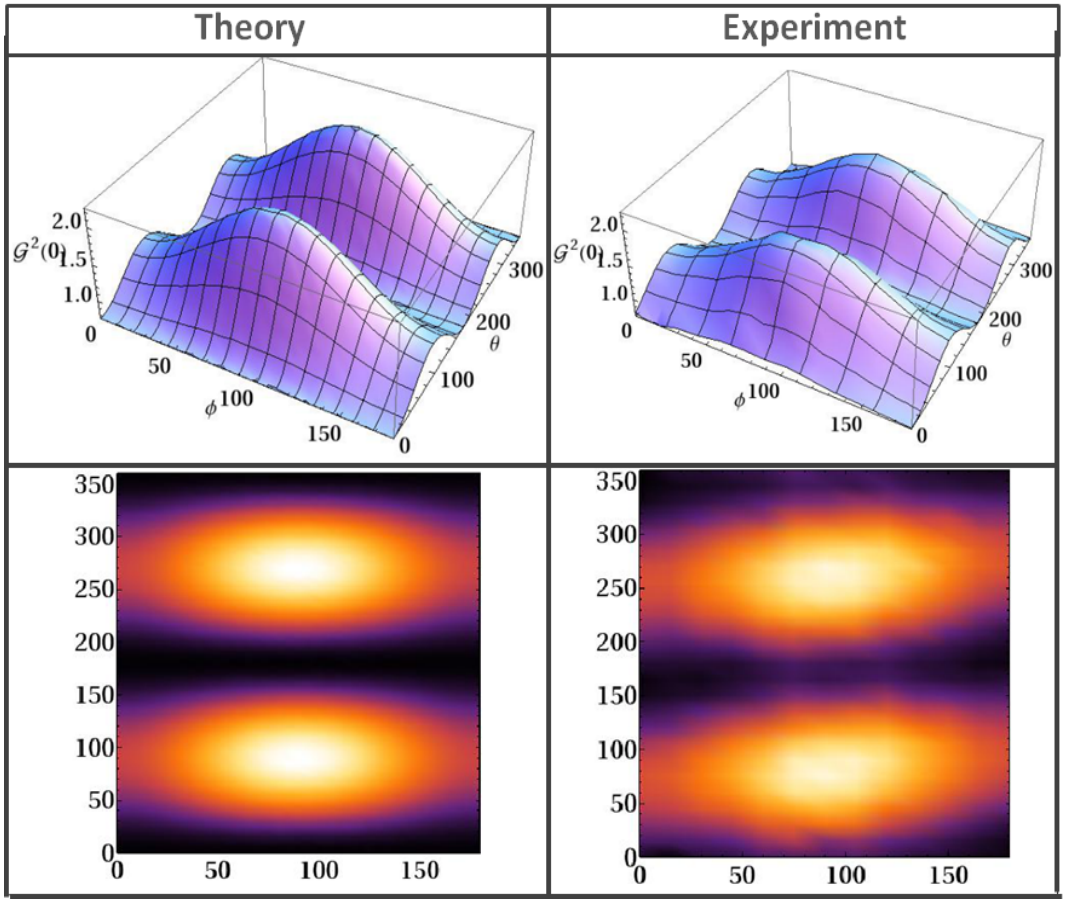

FIGURE 2.8: Figure shows the comparison between the theoretical and the experimental cross correlation values for the detectors D_1 and D_2 as functions of θ and ϕ. The corresponding contour plots are also shown.

and its tunability is likely to be useful in the experiments where correlated photon pairs are used. In fact the tunability of $\mathcal{G}^2(0)$ discussed here and the tunability of the temporal coherence discussed in Chapter 1, provides an interesting way to generate tailored bunched light sources.

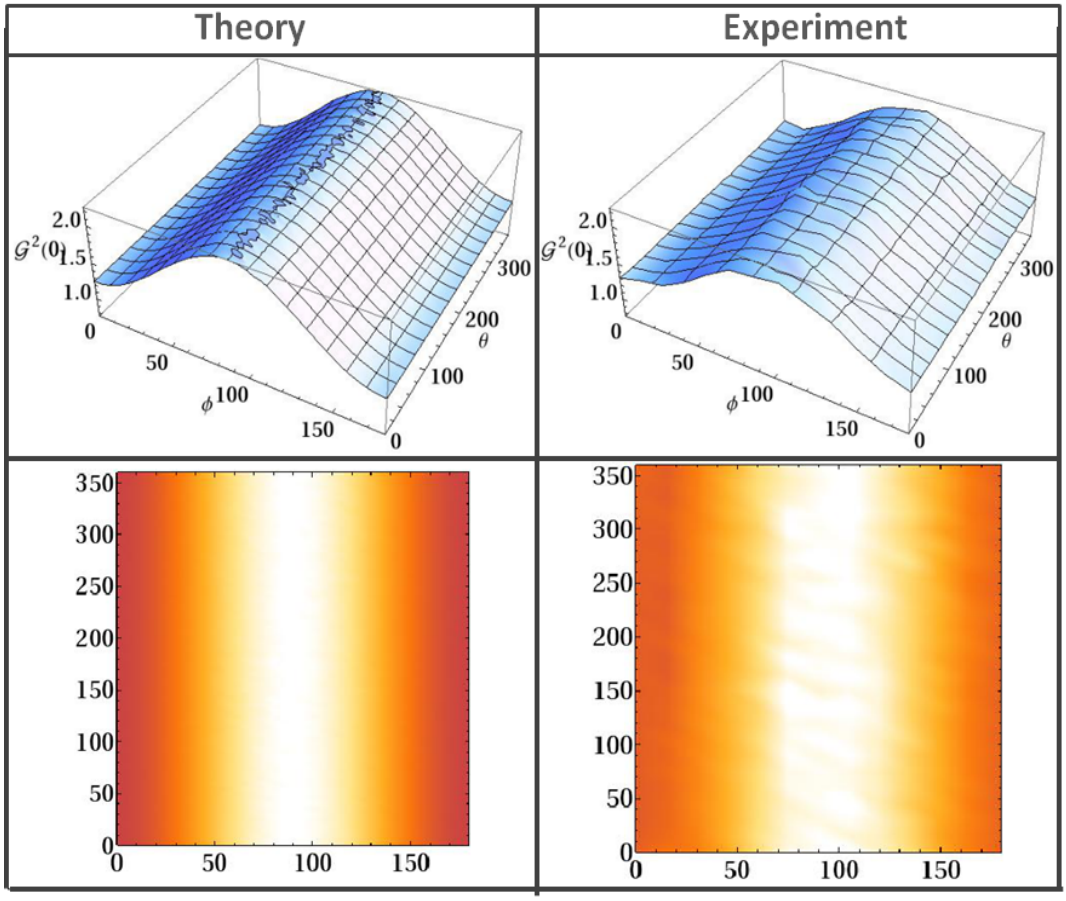

FIGURE 2.9: Figure shows the comparison between the theoretical and the experimental self correlation values for the detector D_1 as functions of θ and ϕ. The corresponding contour plots are also shown.

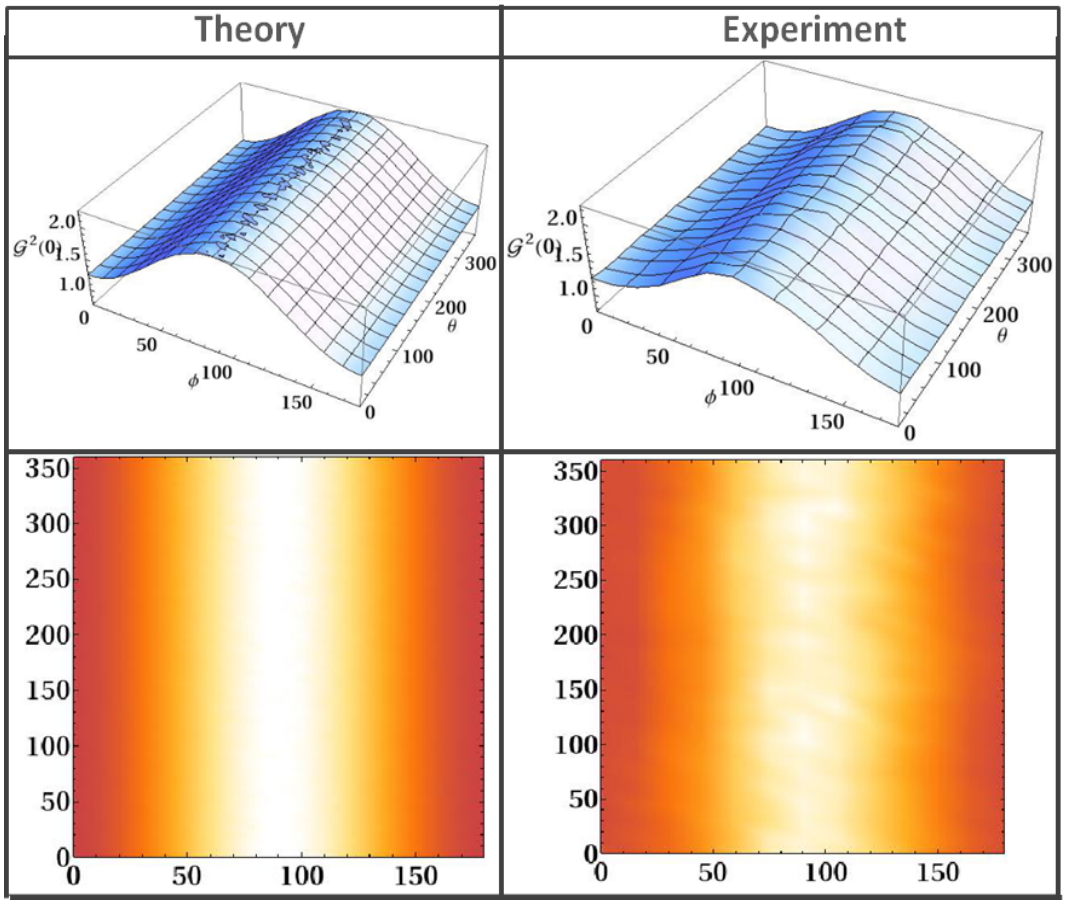

FIGURE 2.10: Figure shows the comparison between the theoretical and the experimental self correlation values for the detector D_2 as functions of θ and ϕ. The corresponding contour plots are also shown.

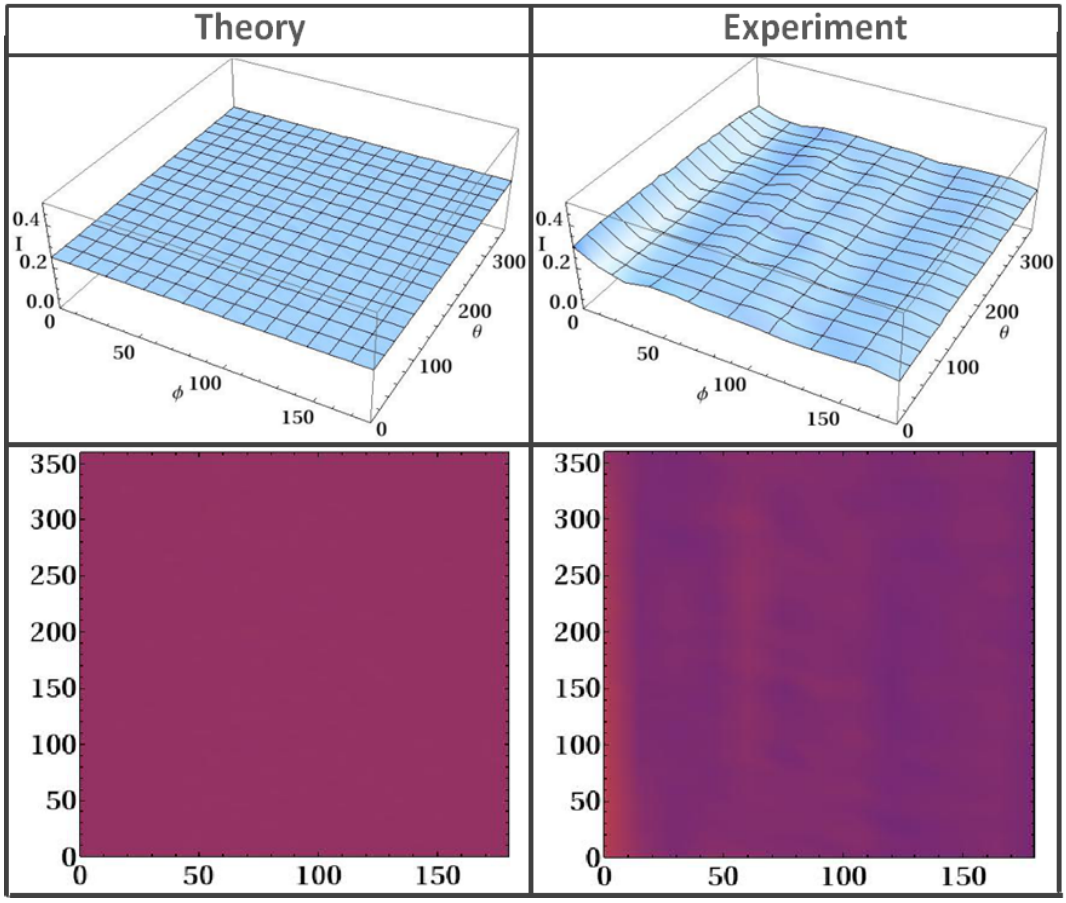

FIGURE 2.11: Figure shows the comparison between the theoretical and the experimental values for the average intensity at detector D_1 as functions of θ and ϕ. The corresponding contour plots are also shown.

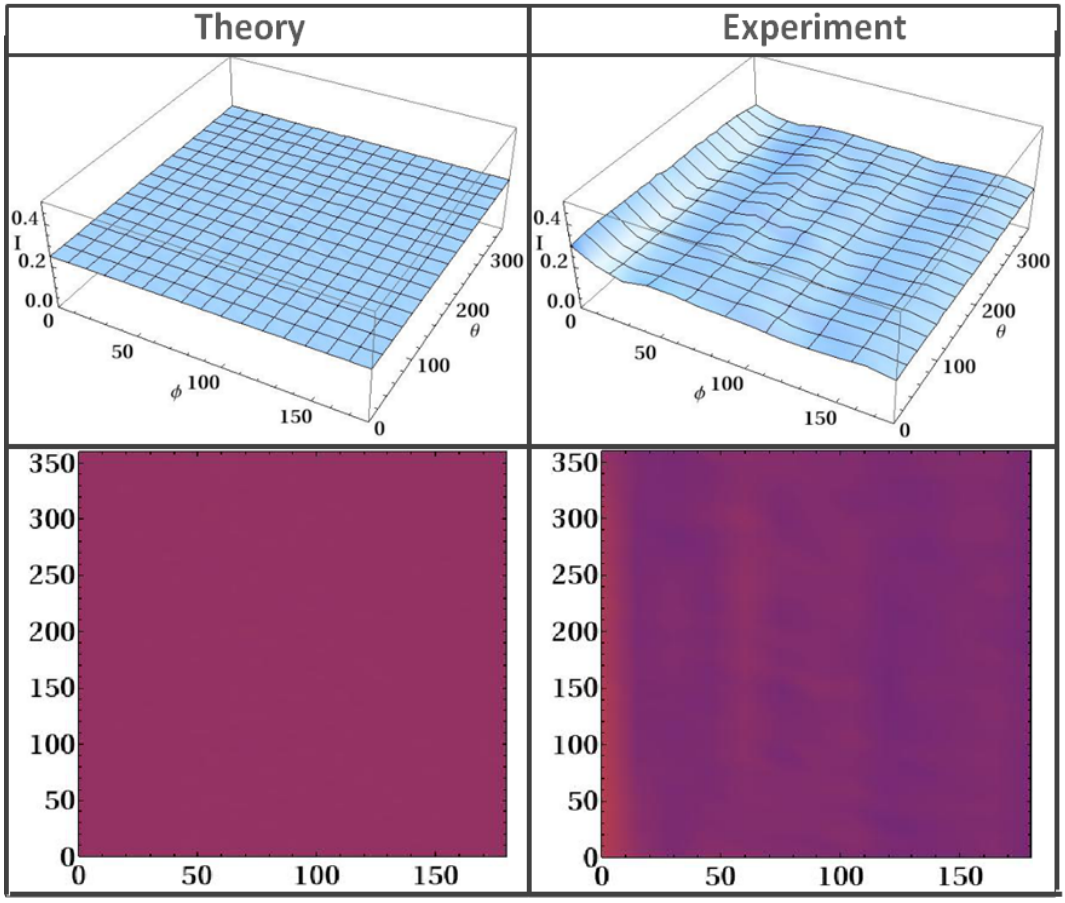

FIGURE 2.12: Figure shows the comparison between the theoretical and the experimental values for the average intensity at detector D_2 as functions of θ and ϕ. The corresponding contour plots are also shown.

3

Chapter 3

3.1 Coherent Light Manipulation of Atoms

Introduction:

The invention of laser has transformed experimental physics in an unprecedented manner. The first working laser was demonstrated by T. H. Maimam in 1960 [79], based on the theoretical idea of C. H. Townes, A. L. Schawlow [80] and G. Gould. Since then the lasers have become a device which have found applications in almost every branch of experimental science, in industries and even in the gadgets used in our everyday life. The invention of tunable diode lasers have made magnificent advancement in atomic and molecular physics. Due to their tunability and narrow linewidth, the spectroscopic investigation of matter, the study of light-atom interaction and the manipulation and interrogation of atoms and molecules has advanced at an outstanding pace.

Laser is a very peculiar device which has a quantum mechanical working principle, but the

emitted photons exhibit completely classical behaviour. It produces a stream of nearly collimated and monochromatic photons with a longer coherence time (few microseconds). This makes the device a very useful tool for precision spectroscopy and precision measurements. The narrow linewidth and the tunability of semiconductor diode lasers have made the manipulation of neutral atoms possible, because of their use in laser cooling and trapping techniques. This has provided a way of controlling the external as well as the internal degrees of freedom of the atoms using coherent photons.

The idea of cooling of neutral atoms from the room temperature atomic vapour by using near-resonant coherent laser radiation was proposed in 1975 by T. Hansch and A. Shawlow [81]. The first experimental demonstration of this method which is also known as Doppler cooling, was demonstrated in 1985 by S. Chu [82]. This remarkable experimental demonstration showed the effect of radiation force exerted by a near resonant light on a neutral atom, to cool it down to microkelvin temperature. Further in 1986 S. Chu et. al. [83] reported the trapping of the precooled neutral atoms using only optical fields. This was based on the idea proposed by Ashkin et. al.[84] for trapping and manipulating neutral atom using continuous coherent radiation. Later in 1987 E. Raab et. al. [85], based on the suggestion of J. Dalibard used an inhomogeneous magnetic field and circularly polarized near resonant coherent laser beams, to cool as well as trap the atoms in the space. This method of cooling and trapping of neutral atoms is known as Magneto-Optical-Trap (MOT). MOT has become a very popular tool for atom trapping because it captures atoms directly from a dilute atomic vapour at room temperature and cools them down to a temperature of few tens to hundreds of microkelvin with a 3D confinement in the space as well. MOT can be used as a cold atom reservoir to transfer the atoms into other traps.

The method of manipulating atoms using coherent light coming out of a narrow bandwidth single mode diode laser is the main concern in this chapter. In the first part of the chapter a relevant theoretical background for different methods to control the external degrees of freedom (centre of mass motion) of the atom is given. The later part of the chapter gives the details about the construction and the characterisation of ^{87}Rb MOT.

3.2 Laser Cooling of Atoms by Spontaneous Scattering of Coherent Photons

Consider a two level system at rest and in its ground state (Fig. 3.1 (a)). It interacts with a photon with angular frequency $\omega_L = \omega_0$. Here ω_0 is the atomic transition frequency, $\omega_0 = \frac{E_2 - E_1}{\hbar}$. Then the atom can absorb a photon by making a transition to excited energy state E_1 (Fig. 3.1

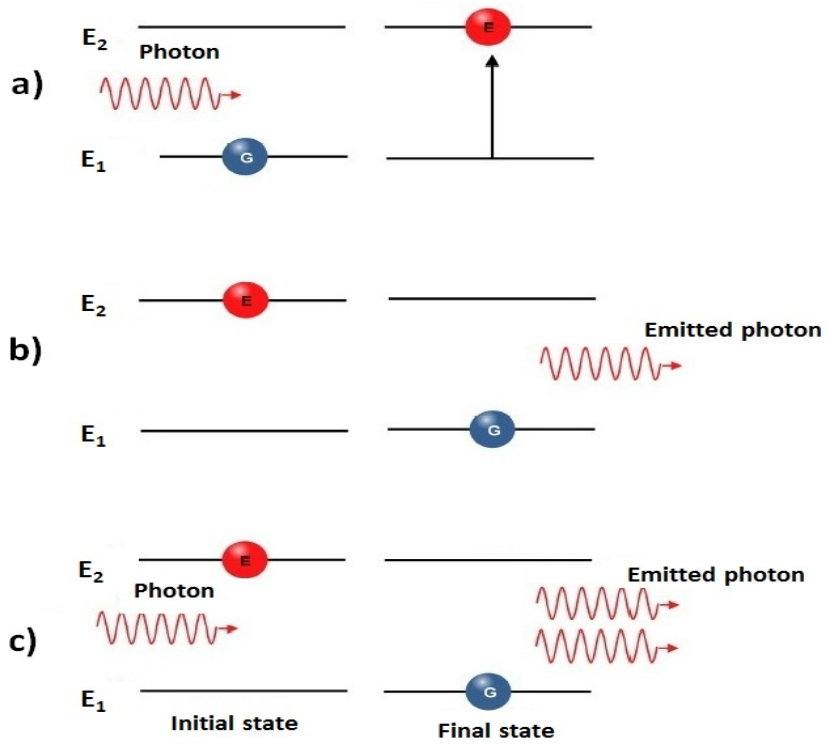

Figure 3.1: An atom in the ground state (E_1) absorbs a resonant photon and makes a transition to the excited state (E_2) as shown in the Fig (a). Atom in the excited state can either emit a photon spontaneously by making a transition back to the state E_1 (Fig. (b)) or in the presence of another photon it can de-excite to state E_2 by the process of stimulated emission (Fig. (c)).

(a)). The excited atom can either spontaneously emit a photon and decay to the ground state E_1 (Fig. 3.1 (b)) or in the presence of another photon it can decays to energy state E_1 by emitting two coherent photons with same phase and frequency (Fig. 3.1 (c)). The later process is known as stimulated emission.

If $\Delta = \omega_L - \omega_0$ is the detuning of the the incident light beam frequency w.r.t. atomic transition,

Γ^{-1} is the radiative lifetime of the excited state, then the rate of the spontaneous scattering of photon from the atom is given by.

$$R_{sc} = \frac{\Gamma}{2}\left(\frac{I/I_s}{1 + I/I_s + [\frac{2\Delta}{\Gamma}]^2}\right), \tag{3.1}$$

where I is the intensity of the incident beam, and I_s is the saturation intensity of the transition. In the process of an absorption-spontaneous emission cycle, the mean momentum transferred to the atom is equal to the momentum of the absorbed photon. This is because the scattering of the photons due to spontaneous emission is isotropic in space thus mean value of the momentum transfer due to this is zero. If the wave vector of the incident plane wave is **k**, then the change in the kinetic energy of the atom due to the recoil by incident photon's momentum and is given by

$$E_{rec} = \frac{p^2}{2m} = \frac{\hbar^2 k^2}{2m} \tag{3.2}$$

Now consider a one dimensional case where the atom is moving with a velocity $\boldsymbol{v}$ as shown in the Fig. 3.2, in a laser field with wave vector $\boldsymbol{k}$. In the presence of two counter-propagating laser beams which are slightly red detuned from the atomic transition i.e. $\Delta = \omega_L - \omega_A < 0$, a Doppler cooling mechanism for a moving atom works as follows:-
If the atom absorbs a photon with momentum $\hbar\boldsymbol{k}$ and emits a photon with momentum $\hbar\boldsymbol{k'}$ then the conservation of total momentum for atom-photon system can be written as follows

$$m\boldsymbol{v} + \hbar\boldsymbol{k} = m\boldsymbol{v'} + \hbar\boldsymbol{k'}, \tag{3.3}$$

For averaging over many cycles of these transitions gives $\langle\hbar\boldsymbol{k'}\rangle = 0$. The recoil momentum opposite to atomic motion is $\hbar\boldsymbol{k}$. Therefore the frictional force opposing the atomic motion can be written as multiplication of momentum transfer per cycle to the net spontaneous emission rate. Considering the opposite Doppler shifts of the two counter propagating beams, the resultant force, at low intensity limit, on the atom can be written as

$$\boldsymbol{F}(\boldsymbol{v}) = \boldsymbol{F}_{z+} + \boldsymbol{F}_{z-}, \quad \text{where} \quad \boldsymbol{F}_{z_\pm} = \pm\hbar\boldsymbol{k}R_{sc} \tag{3.4}$$

This force is always opposite to the velocity of the atom. Due to this frictional force, the atomic motion is damped in both directions. This gives rise to cooling of atoms. Such an arrangement of counter propagating beams is called optical molasses. For small velocities, $\boldsymbol{k}.\boldsymbol{v} << \Gamma$, Eq. 3.4 for net force can be written as

$$\boldsymbol{F}(\boldsymbol{v}) \approxeq \frac{8\hbar k^2 \Delta I/I_{sat}}{\Gamma\left(1 + I/I_{sat} + 4\left(\frac{\Delta}{\Gamma}\right)^2\right)^2}.\boldsymbol{v} \approxeq -\beta \boldsymbol{v} \tag{3.5}$$

where β corresponds to a friction coefficient. It is clear from the equation that friction occurs only for negative detuning. For negative detuning the atomic motion gets damped and thus the atoms get cooled.

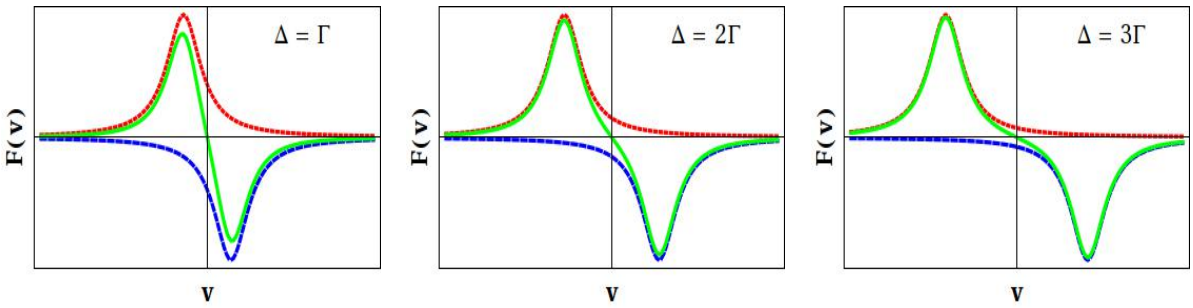

Figure 3.2: Radiation force versus velocity of the atom at three different detunings. Continuous curves represents the total scattering force $\boldsymbol{F}(\boldsymbol{v})$, the dashed curves represent $\boldsymbol{F}_{z+}$ and $\boldsymbol{F}_{z-}$

3.2.1 Doppler Cooling in 3D

Based on the above analysis it is clear that using three pairs of counter propagating laser beams, which are red detuned with respect to the atomic transition, a three dimensional cooling can be achieved. In the presence of red detuned laser beam, an atom is more likely to absorb a photon when it moves towards the laser source because the 'Doppler shifted' frequency is closer to resonance in atomic reference frame. Then each of the photons absorbed by the atom gives a recoil in the direction of laser beam and opposite to atomic motion. Hence the atom slows down. The minimum temperature achieved by Doppler cooling is limited by the spontaneous emission and the absorption cycles [86]. These cycles, due to the stochastic nature of spontaneous emission process, cause a random walk of the atom in momentum space, similar to Brownian

motion. This causes heating of the atom. The minimum temperature for Doppler cooling then can be determined by a balance condition between cooling and heating rates and is given by

$$k_B T_{min} = \hbar\Gamma/2. \tag{3.6}$$

In our experimental setup we use Rubidium atom which has a Doppler limit of approximately 150 μK.

The atoms can only be cooled by optical molasses, but they cannot be trapped in space as that would require a position dependent force as well, along with the velocity dependent force. For this one requires a Magneto-Optical-Traps (MOT) setup which is described in the section 3.5.

3.3 Sub-Doppler Cooling

In a very precise temperature measurement experiment of laser cooled gas of sodium atoms, Paul et.al. showed that the temperature obtained in an optical molasses could be much lower than predicted by the Doppler cooling limit [87]. This was thought to be arising due to some cooling mechanisms other than the Doppler scattering force which might be operating. Later in a detailed theoretical analysis, this is attributed to the multilevel structure of the real atoms, in contrast to simple two level model of the atom which was assumed for simplification. The existence of light polarization gradients in space and the AC stark shifts (light shifts), along with the multi-level structure of atom gives the explanation for temperature less than the Doppler limit [88, 89].

3.3.1 Sisyphus Cooling

Sisyphus cooling an example of Sub-Doppler cooling mechanism was proposed by J. Dalibard and C. Cohen-Tannoudji [88] in 1989. Consider the case of an atom with excited state $|J_e\rangle$ and ground state $|J_g\rangle$, with a number of Zeeman sublevels, which are degenerate in the absence of magnetic field. A specific example is shown in the Fig. 3.3 with ground state $|J_g = 1/2\rangle$ and excited state $|J_e = 3/2\rangle$. The polarization of light decides the population among the ground state sublevels in this case $m_J = \pm 1/2$. The probabilities for different excited state to decay to different ground state sublevels is shown in the Fig. 3.3 (a).

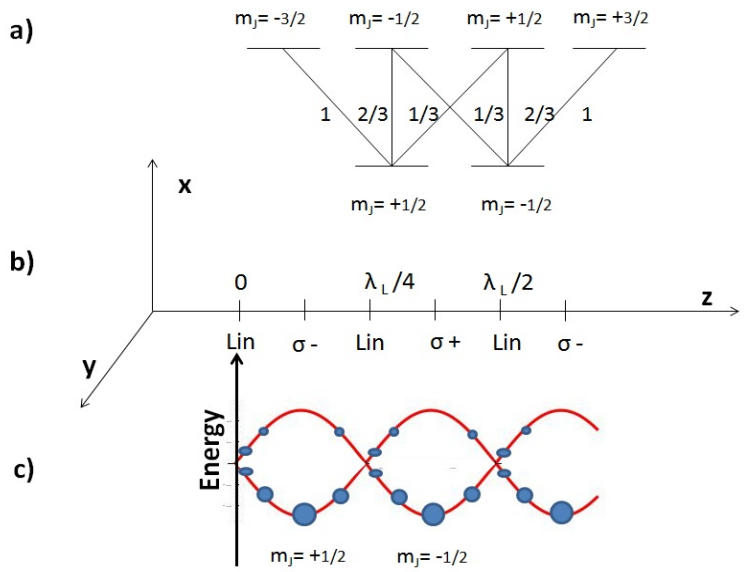

Figure 3.3: Fig. (a) shows the magnetic substates. Lower two ($m_J = +1/2$ and $m_J = -1/2$) are for ground state, $|J_g = 1/2\rangle$ and upper four ($m_J = -3/2$, $m_J = -1/2$, $m_J = +1/2$, $m_J = +3/2$) are for excited state $|J_e = 3/2\rangle$. Fig (b) shows resultant polarization of the two counter propagating beam with wavelength λ_L. Fig (c) Light shift in the ground state energy as a function of z. The size of the solid circles represents the population of the two substates.

Now consider two counter-propagating laser beams with orthogonal linear polarization and wavelength λ_L . The spatial variation of the polarization of the total radiation field is shown in the Fig. 3.3 b) which changes from linear to circular over a distance of $\lambda_L/8$. The polarization dependent light shifts of the ground state sublevels due to the electric field of light , varies spatially as shown. At the point in space where polarization is $\sigma+$, light shift of $|J_g = 1/2, m_J = +1/2\rangle$ is three times more compared to $|J_g = 1/2, m_J = -1/2\rangle$ and vice versa for the points of $\sigma-$ polarization. It is clear that at $\sigma+$ points the population of $|J_g = 1/2, m_J = +1/2\rangle$ becomes larger and the other way round at $\sigma-$ polarization points. The population of the two ground state sublevels are equal at the points where the polarization is linear. The time taken by optical pumping to produce the final population distribution is τ_p.

If an atom moves from left to right in such as radiation field, as described above, and with a maximum population at $|J_g = 1/2, m_J = -1/2\rangle$ and if the velocity of the atom is v, such that $v\tau_p = \lambda_L/4$, the atom can move to the top of the potential well without making a transition

to a different substate. This is possible when some of the kinetic energy of the atom must

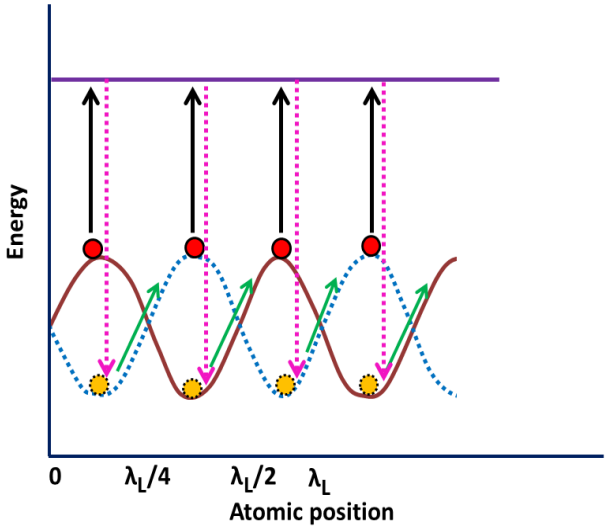

FIGURE 3.4: This figure shows the Sisyphus effect for an atom moving in a polarisation gradient laser field shown in Fig 3.3. The atom during its motion climbs out a potential valley and falls down to the bottom of the next valley by emitting a photon and therefore causing the cooling of the atom.

be transferred to potential energy. Therefore at the top of the potential well, atom makes a transition to the bottom of the next valley with highest probability. This process continues when the atom makes a transition from top to bottom by climbing the hill and then falling to the bottom by emitting photon (Fig. 3.4). This way atom gets cooled and this cooling mechanism is called *Sisyphus Effect*.

The above discussion considers the most favourable case, where $v\tau_p = \lambda_L/4$. But the cooling mechanism works over a range of velocities of the order λ_L/τ_p. Note that the optical pumping rate τ_p is proportional to the laser intensity I, therefore the range of velocities for which Sisyphus Effect work is also proportional to intensity. This is the difference between the Doppler cooling and Sisyphus cooling. In Doppler cooling the capture velocity is independent of intensity.

3.4 Magneto-Optical-Trap

Realization of magneto-optical-trap (MOT) for neutral atoms exploits the inelastic scattering of incident photons from a laser beam by the atom. In a MOT an inhomogeneous magnetic field generated by a pair of anti-Helmholtz coils and the three pairs of counter propagating laser beams (which are red detuned from a particular cyclic hyperfine transition) in x, y and z direction, provides a position dependent force due to momentum transfer from atom to light. This position and velocity dependent radiation pressure force on the atom, cools it down due to Doppler effect and also traps them in space.

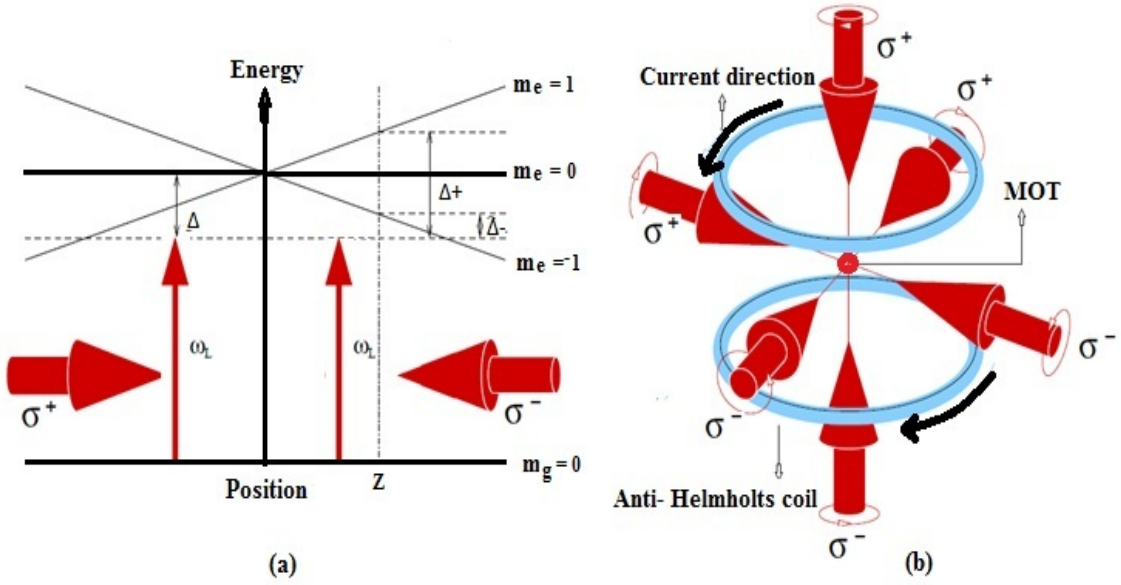

FIGURE 3.5: Fig. (a) shows the shift in the Zeeman sublevels in the presence of a magnetic quadrupole field. For two oppositely circular polarised light which are red detuned and counter propagating each other, as shown in the figure, the atom scatters photons preferentially from that beam which pushes the atom towards $z = 0$ position. Fig. (b) shows the basic three dimensional schematic of the MOT. Here m_g corresponds to $|J = 0, m_J\rangle$ while m_e to $|J = 1, m_J\rangle$

In a one dimensional case this can be understood as follows. Consider an atom moving in one dimension along $+z$ direction in the presence of a pair of counter propagating laser beams which are slightly red detuned with respect to the atomic resonance transition and have opposite circular polarization as shown in the Fig. 3.5. In the presence of the inhomogeneous magnetic field created by the anti-Helmholtz coil, the atomic hyperfine levels exhibits Zeeman splitting of

the levels shown for a simple case $J = 0$ ground state and $J = 1$ excited state. The magnetic field B splits the excited state due to the linear Zeeman splitting and the shift in the energy for state $|J, m_J\rangle$ is given by

$$\Delta E = m_J \; g_J \; \mu_B \; B \tag{3.7}$$

where g_J is the Lande's g-factor and μ_B is the Bohr's magnetron and B is the inhomogeneous magnetic field in one dimension and can be written as,

$$B(z) = \frac{dB}{dz} \; z. \tag{3.8}$$

Assuming the field gradient $\frac{dB}{dz} > 0$ and $g_J > 0$ the $|J = 1, m_J = -1\rangle$ level shifts downwards on the right side of the zero magnetic field point and therefore gets closer to the resonance for a red detuned beam (Fig. 3.5). As the atom moves towards the right side it sees the incoming photons more and more in resonance with $m_J = -1$ for incoming $\sigma-$ polarized beam and vice versa for atomic motion in $-z$ direction. This in turn exerts a radiation pressure on the atom towards $z = 0$. Therefore the radiation pressure force is always opposite to the direction of motion and directed to a fixed point in the space. This way one gets a cooling and trapping of atoms due to radiation pressure. The total force on the atom can be expressed as, $\boldsymbol{F} = \boldsymbol{F}_+ + \boldsymbol{F}_-$, where

$$\boldsymbol{F}_\pm = \pm \frac{\hbar \boldsymbol{k} \Gamma}{2} \frac{I/I_{sat}}{1 + I/I_{sat} + 4\left(\frac{\Delta_\pm}{\Gamma}\right)^2} \tag{3.9}$$

here $\Delta_\pm$ is the detuning of the two beams seen by the atom in the presence of inhomogeneous magnetic field and is given by

$$\Delta_\pm = \Delta \mp \boldsymbol{k}.\boldsymbol{v} \pm \mu^{'} B/\hbar \tag{3.10}$$

where $\mu^{'}$ is the effective magnetic moment of the excited state.

When the Doppler and Zeeman shifts are small compared to the detuning Δ, the force can be expanded in v and z, then Eq. 3.5 reads as follows

$$\boldsymbol{F}(\boldsymbol{v}) = -\beta \boldsymbol{v} - \kappa \boldsymbol{z} \tag{3.11}$$

where the damping coefficient β has the same definition as in Eq. 3.1 and spring constant is defined as

$$\kappa = \frac{\mu^{'} A}{\hbar k}\beta \tag{3.12}$$

Eq. 3.11 is that for a damped harmonic oscillator with damping coefficient equal to $\frac{\beta}{M}$ and the oscillating frequency equal to $\sqrt{\frac{\kappa}{M}}$, where M is the mass.

The one dimensional scheme for MOT can be extended to three dimension in the presence of a spherical quadrupole field by using a pair of anti-Helmholtz coil. The field in three dimension has the following form

$$\boldsymbol{B}(\boldsymbol{x}) = \frac{dB}{dz}\left(-\frac{x}{2}, -\frac{y}{2}, z\right) \tag{3.13}$$

along with two circularly polarized beam with right-handed helicity in z-direction and four circularly polarized beams with left-handed helicity along x- and y-direction.

3.5 Dipole Trap:- A Far-Off Resonant Trap

Once the atoms are cooled (typically below 1 mK temperature), by laser cooling techniques, these pre-cooled atoms can be trapped using a far-off resonant trap. This trap works on a completely different principle as compared to the radiation pressure trap. Here the trapping force, which is a dipole force, acts along the gradient of the intensity and its direction is determined by the detuning of the trapping laser with respect to resonance transition of the atom.

3.5.1 Classical Picture

For an intuitive understanding of the working principle of the dipole trap, one can consider the interaction of the neutral atoms with off resonant beam in classical picture where light from the laser is treated as continuous classical wave and the atom as a classical oscillating dipole in the presence of the electric field oscillation [90]. For a classical system of neutral atom, the electric field induces an electric dipole moment in the atom due to its polarizability. If the oscillating electric field of the light is

$$E(r,t) = \hat{e}E_0(r)\exp(-i\omega t) + c.c., \tag{3.14}$$

where $\hat{e}$ defines the polarization, $E_0(r)$ is the amplitude and ω is the frequency of the field. The induced dipole moment at any instant, at the location of the atom is

$$\boldsymbol{p(r,t)} = \boldsymbol{p_0(r)} \exp(-i\omega t) + c.c. \tag{3.15}$$

where the induced dipole moment p_0 is linearly proportional to $E_0(r)$ with the complex polarizability of the atom as the proportionality factor,

$$p_0 = \alpha(\omega) E_0. \tag{3.16}$$

The complex polarizability of the atom is given by

$$\alpha(\omega) = \frac{e^2}{m_e} \frac{1}{{\omega_0}^2 - \omega^2 - i\omega\Gamma} \tag{3.17}$$

This induced dipole interacts with the driving field itself which has an interaction energy

$$W = -\boldsymbol{p.E} \tag{3.18}$$

Due to very high frequency of the optical field (10^{14} Hz), atomic motion can only experience a time averaged effect of W. Therefore the potential that the atom experience due to the interaction with the field is,

$$U_{dip}(r) = \langle W \rangle_t = -\frac{1}{2\epsilon_0 c} Re(\alpha) I(r) \tag{3.19}$$

The dipole force is given by the gradient of the U_{dip}

$$\boldsymbol{F_{dip}(r)} = -\boldsymbol{\nabla} U_{dip}(r) = \frac{1}{2\epsilon_0 c} Re(\alpha) \nabla I(r) \tag{3.20}$$

where $I(r) = \frac{c\epsilon_0 |E^2|}{2}$. It is clear that dipole force acts along the gradient of the light intensity unlike the radiation force which acts in the laser propagation direction.

Dependence of the dipole force on the detuning :- Fig. 3.6 shows the dispersion relation of $\alpha(\omega)$. It is clear from the Eq. 3.20, that for a dipole force, the direction of the force depends upon the detuning with respect to the atomic resonance frequency. As $\alpha(\omega)$ changes sign at $\omega = \omega_0$, there are two different behaviour of the dipole force around resonance frequency. For external field frequency smaller than atomic resonance frequency (detuning $\Delta = (\omega - \omega_0) \leq 0$),

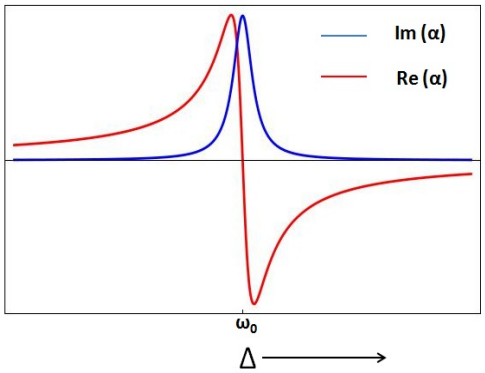

FIGURE 3.6: The dipole force is proportional to Re(α), having a dispersive profile with a change of sign at resonance. But the scattering rate depends on Im(α) with a Lorentzian profile.

the induced dipole oscillations are in phase with the external field oscillation and the atom feels force towards the high intensity region and gets pulled towards that region. In contrast to this, if the external field frequency is higher than resonance frequency ($\Delta = (\omega - \omega_0) \geq 0$), dipole oscillations are out of phase w.r.t. external field oscillation and the atom gets repelled from the high intensity region.

3.5.2 Scattering Rate

In this picture of damped harmonic oscillator, energy absorbed by the atom is

$$P_{abs} = \langle \hat{p}.E \rangle_t = \frac{\omega}{\epsilon_0 c} \mathrm{Im}(\alpha) \mathrm{I(r)} \tag{3.21}$$

This energy is radiated as dipole radiation. The energy radiated is proportional to the intensity of the trapping field and to the imaginary part of polarizability. In classical picture this radiation is emitted continuously, but in quantum mechanical picture the radiated energy corresponds to the scattering rate of the photons given by

$$R_{sc} = \frac{P_{abs}}{\hbar\omega} = \frac{1}{\hbar\epsilon_0 c} \mathrm{Im}(\alpha) \mathrm{I(r)} \tag{3.22}$$

From the classical analysis, $F_{dip} \propto \frac{1}{\Delta}$ and $R_{sc} \propto \frac{1}{\Delta^2}$. It is clear that the classical physics already predicts the correct dependence. In the next section the quantum-mechanical treatment is given.

In the present experimental scenario where the detuning Δ is much larger than the natural linewidth of the atomic transition, $\Delta \geq \Gamma$, the expression for the trap depth and the scattering

rate are as follows

$$U_{dip} = -\frac{3\pi c^2}{2}\frac{I}{\Gamma}\left(\frac{1}{\omega_0 - \omega} + \frac{1}{\omega_0 + \omega}\right) \tag{3.23}$$

$$R_{sc} = \frac{3\pi c^2 \Gamma^2 \omega^3}{2\hbar {\omega_0}^6}\left(\frac{1}{\omega_0 - \omega} + \frac{1}{\omega_0 + \omega}\right) I \tag{3.24}$$

For the case of detuning less than optical frequency of the trapping radiation, $\Delta << \omega$, the above expression can be approximated by the following

$$U_{dip} = \frac{3\pi c^2}{2}\frac{I}{{\omega_0}^3}\frac{\Gamma}{\Delta} \tag{3.25}$$

$$R_{sc} = \left(\frac{3\pi c^2 I}{2\hbar {\omega_0}^3}\right)\frac{\Gamma^2}{\Delta^2} = \frac{\Gamma}{\hbar\Delta}U_{dip} \tag{3.26}$$

3.5.3 Dipole Force Direction

For the case of $\Delta << \omega_0$, From the Eq. 3.25,The dipole force is

$$F_{dip} = -\left(\frac{3\pi c^2 \Gamma}{2{\omega_0}^3}\right)\frac{\nabla I}{\Delta} \tag{3.27}$$

The direction of dipole force along the intensity gradient depends upon the sign of the detuning. For red detuned trapping laser,$\Delta < 0$, the force is along the highest intensity region i.e. atom gets pulled towards high electric field region. While for the other case, when the laser frequency is above resonance frequency, $\Delta > 0$, the atom gets pushed away from the high intensity region. It is also straight forward to see that for large detuning, a condition for very low scattering rate of photons can be achieved at the cost of increased intensity at the trapping region.

3.5.4 Dipole Trap for Multilevel Atom in Classical Picture

In a practical experimental situation where one needs to trap a multilevel atom (Rubidium in this case), the classical model of damped oscillating dipole still produces correct dependencies of force and scattering rate on field parameters i.e. intensity and detuning. To take into account for multilevel resonance transition approximately, one has to apply Eq. 3.23 and Eq. 3.24 separately for each individual transition weighted by the oscillator strength of the transition.

For the case of this work the trapping laser was operated at 852 nm and the neutral atoms were Rubidium atoms. Therefore only D1 and D2 lines contribute to the dipole trapping force significantly. The full expression for dipole potential and the scattering rate in this case are

$$U = -\frac{3\pi c^2 I}{2}[\zeta_{D1}\frac{\Gamma_{D1}}{{\omega_{D1}}^3}\left(\frac{1}{\omega_{D1}-\omega}+\frac{1}{\omega_{D1}+\omega}\right)+\zeta_{D2}\frac{\Gamma_{D2}}{{\omega_{D2}}^3}\left(\frac{1}{\omega_{D2}-\omega}+\frac{1}{\omega_{D2}+\omega}\right) +\zeta_{D3}\frac{\Gamma_{D3}}{{\omega_{D3}}^3}(\frac{1}{\omega_{D3}-\omega}+\frac{1}{\omega_{D3}+\omega})] \tag{3.28}$$

$$R_{sc} = \frac{3\pi c^2 I}{2\hbar}[\zeta_{D1}\frac{{\Gamma_{D1}}^2\omega^3}{{\omega_{D1}}^6}\left(\frac{1}{\omega_{D1}-\omega}+\frac{1}{\omega_{D1}+\omega}\right)+\zeta_{D2}\frac{{\Gamma_{D2}}^2\omega^3}{{\omega_{D2}}^6}\left(\frac{1}{\omega_{D2}-\omega}+\frac{1}{\omega_{D2}+\omega}\right) +\zeta_{D3}\frac{{\Gamma_{D3}}^3\omega^3}{{\omega_{D3}}^6}\left(\frac{1}{\omega_{D3}-\omega}+\frac{1}{\omega_{D3}+\omega}\right)] \tag{3.29}$$

where ζ represents the dipole oscillator strength for the respective transition and related with decay rate of the transition is as follows [90]

$$\Gamma = \frac{e^2\omega^3}{2\pi\epsilon_0 m_e c^3}\frac{g_g}{g_e}\zeta \tag{3.30}$$

where g_e and g_g are the degeneracies of the excited and ground state respectively.

3.5.5 Semiclassical Picture

Semiclassical treatment of atom-photon interaction involves quantization of atomic system and its interaction with the classical radiation field. In contrast to classical theory, here the decay rate represents the spontaneous emission rate from the excited state and is given as follows

$$\Gamma = \frac{\omega^3}{3\pi\epsilon_0\hbar c^3}|\langle e|\hat{d}|g\rangle|^2, \tag{3.31}$$

where $\hat{d}$ is the dipole operator and $\langle e|\hat{d}|g\rangle$ denotes the dipole matrix element of the two level atom between the ground state $|g\rangle$ and the excited state $|e\rangle$. [90]

The semiclassical picture yields the expression for dipole potential and the scattering rate in terms of saturation intensity along with other parameters as follows

$$U_{dip} = \frac{\hbar\Gamma}{8}\frac{\Gamma}{\delta}\frac{I(r)}{I_s}, \tag{3.32}$$

$$\Gamma_{sc} = \frac{\Gamma}{8}\left(\frac{\Gamma}{\delta}\right)^2\frac{I(r)}{I_s} \tag{3.33}$$

where the saturation intensity I_s is defined as follows

$$I_s = \frac{{\omega_0}^6}{36\pi^2\epsilon_0 c^5}|\langle e|\hat{d}|g\rangle|^2 \tag{3.34}$$

and

$$\frac{1}{\delta} = \frac{1}{\omega - \omega_0} + \frac{1}{\omega + \omega_0}. \tag{3.35}$$

For detuning much less compared to optical frequency of the trapping radiation i.e. $\Delta << \omega_0$, δ can be replaced by detuning ,Δ (rotating wave approximation).

3.5.6 Semiclassical Picture for multi-level atoms

Multilevel atom case can be considered within semiclassical picture by including the contributions of all coupled excited states. The interaction of the atom with the time dependent electric field of the form Eq. 3.14, is described by time dependent perturbation theory. The energy shift in the atomic levels due to light-atom interaction for a given state with eigen energy E_i is given by [91]

$$\Delta E(E_i) = -\frac{1}{4}\sum_{n',J',F',m'}\frac{1}{\hbar\Delta'_{if}}|\langle nJIFm|\hat{d}.E|n'J'IF'm'\rangle|^2, \tag{3.36}$$

where n, J, F, m and n, J', F', m' are the quantum numbers for ground and excited states respectively and the summation goes over all the atomic states E_f except initial state E_i. Δ'_{if} is defined as the effective detuning in terms of atomic transition frequency ω_0 and frequency of the electric field of light.

$$\frac{1}{\hbar\Delta'_{if}} := \frac{1}{\hbar(\omega_0 - \omega)} + \frac{1}{\hbar(\omega_0 + \omega)}, \tag{3.37}$$

Expanding the term $\hat{\mathrm{d}}.\mathrm{E}$ in Eq. 3.36 in terms of the spherical tensors and then applying the standard procedure of Wigner-Eckart theorem [91], the new expression reads as follows

$$\Delta E = -\frac{1}{4}\sum_{n',J',F',m'}\frac{1}{\hbar\Delta'_{if}}|E|^2 \begin{pmatrix} F & 1 & F' \\ -m & -\mu & m' \end{pmatrix} |\langle nJIF||d||n'J'IF'\rangle|^2 \tag{3.38}$$

Here the brackets represent the 3-J-symbols, μ is the polarization of light which can have $+1, -1$ or 0 value depending whether the polarization is right circular $\sigma+$, left circular $\sigma-$ or linear

respectively. $|\langle nJIF||d||n'J'IF'\rangle|$ represents the reduced matrix elements. By introducing 6-J-symbols, the hyperfine coupling can be separated and this gives

$$|\langle nJIF||d||n'J'IF'\rangle| = (2F+1)(2F'+1)(-1)^{J+I+F'+1} \begin{Bmatrix} J & F & I \\ F' & J' & 1 \end{Bmatrix} \langle nJ||d||n'J'\rangle \quad (3.39)$$

The remaining elements of the matrix $\langle nJ||d||n'J'\rangle$ is given in terms of the oscillator strength f_{if} for the transition $nJ \rightarrow n'J'$

$$f_{if} = \frac{2m_e}{3\hbar e^2}\frac{\omega_{if}}{2J+1}|\langle nJ||d||n'J'\rangle|^2 \quad (3.40)$$

Substituting values from above two equations into the Eq. 3.38 which yields a final expression for energy level shift depending only on the transition frequency and the oscillator strengths as follows:-

$$\Delta E(n,J,F,m,\mu) = -\frac{3e^2 I}{8\pi c^2 m\epsilon_0}(2J+1)(2F+1)\sum_{n',J',F',m'}(2F'+1)\frac{2\pi c}{\omega_{if}}\frac{f_{if}}{\Delta'_{if}} \begin{pmatrix} F & 1 & F' \\ -m & -\mu & m' \end{pmatrix}^2 \begin{Bmatrix} J & F & I \\ F' & J' & 1 \end{Bmatrix}^2 \quad (3.41)$$

3.5.7 Quantum Mechanical Picture

The full quantum mechanical picture of the dipole force considers the *dressed state* picture of the atom-photon interaction [92]. Here both the atom and the field are quantized. The quantized atom when interacts with a quantized monochromatic single mode light field, then the resulting eigenstates of this new atom-photon system are called as dressed states. The eigen energies of these new eigenstates are a function of laser intensity and detuning. The dipole potentials are explained in terms of light shifts (AC Stark shift) which are related to the intensity at observation point. The transition rates and lifetime are assigned to the dressed states by coupling them to the empty modes of the electromagnetic field similar to the case of atomic levels alone.

Hamiltonian

Considering the two-level atom at rest and interacting with the light field of the trapping laser. The Hamiltonian for the combined system is

$$\hat{H} = \hat{H_A} + \hat{H_L} + \hat{V} \tag{3.42}$$

$\hat{H_A}$ is the Hamiltonian for two level ($|g\rangle$ ground state and $|e\rangle$ excited state) atomic system with $\hbar\omega_0$ energy difference between the two energy levels.

$$\hat{H_A} = \hbar\omega_0 |e\rangle\langle e|. \tag{3.43}$$

For simplification, the effect of dipole trapping laser on the atom is modelled as a two level atomic system placed inside a large, lossless ring resonator. The dipole trap laser beam in this picture contains n photons of energy $\hbar\omega$ and the atom sees a continuous stream of new photons provided n is fairly constant. The Hamiltonian of the light field is

$$\hat{H_L} = \hbar\omega(\hat{a}^\dagger\hat{a} + \frac{1}{2}), \tag{3.44}$$

where $\hat{a^\dagger}$ and $\hat{a}$ are the creation and annihilation operators of the photons in the mode.

Two Level Atomic system with trapping light field

First a simple case of two level atom is considered in full quantum mechanical view point. The energy eigenstates of $\hat{H_A} + \hat{H_L}$ are denoted by $|g, n+1\rangle$ and $|e, n\rangle$. Within one manifold $E(n)$ the energy levels are separated by $\hbar\Delta$, where $\Delta = \omega - \omega_0$, whereas corresponding levels of two successive manifolds are one photon energy $\hbar\omega$ apart.

Coupling

Now the interaction part is introduced in the Hamiltonian $\hat{H}$, which is $\hat{V}$ and expressed as operator $\hat{d}$ times the laser field operator $\hat{E}$ at the location of the atom,

$$\hat{V} = -\hat{d}.\hat{E}(r) \tag{3.45}$$

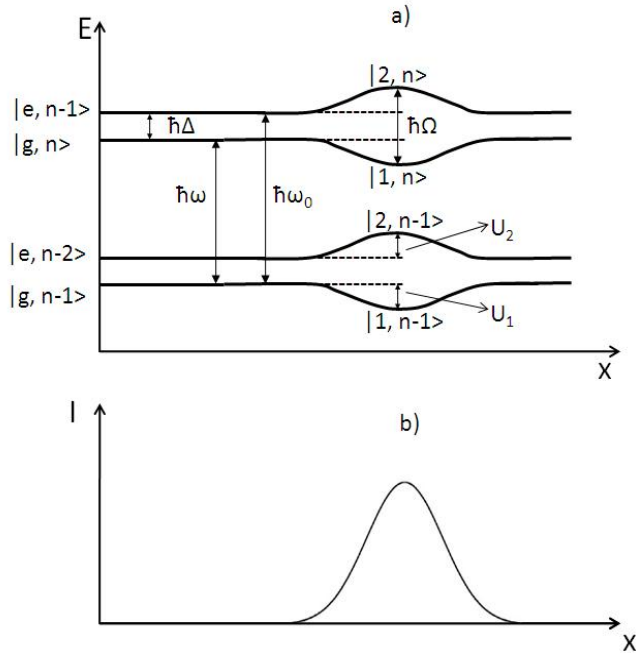

Figure 3.7: In the presence of a strong, red detuned Gaussian laser beam, the atom interacts with the radiation field which causes shift in the levels of the atom, in the dressed state picture. This creates a position dependent dipole potential.

The electric field operator in terms of $\varepsilon(r)$ (mode distribution) of the laser beam is,

$$\hat{E}(r) = \varepsilon(r)\,\hat{a} + \varepsilon^*(r)\hat{a}^\dagger \tag{3.46}$$

which satisfy the normalization condition

$$\epsilon_0 \int_V (\varepsilon(r)^2 + \varepsilon^*(r)^2) = \hbar\omega_o. \tag{3.47}$$

The dipole moment operator for the atom is

$$\hat{d} = d|e\rangle\langle g| + d^*|g\rangle\langle e| \tag{3.48}$$

The full coupling Hamiltonian reads as

$$\hat{V} = -[d.\varepsilon\,\hat{a}|e\rangle\langle g| + d\,.\,\varepsilon^*\hat{a}^\dagger|e\rangle\langle g| + d^*.\varepsilon\,\hat{a}|g\rangle\langle e| + d^*.\varepsilon^*\hat{a}^\dagger|g\rangle\langle e|] \tag{3.49}$$

Coupling of the states $|g, n\rangle$ and $|e, n-1\rangle$ enters into the Eq. 3.49 through first and last term. These states are separated by Δ. The other two terms of the equation couples the states $|g, n\rangle$

and $|e, n+1\rangle$, having separation $\omega_0+\omega >> \Delta$. This larger separation in the second case reduces the coupling and the corresponding terms can be neglected on the account of rotating wave approximation.

The states within same manifold only couples by

$$\langle e, n-1|\hat{V}|g, n\rangle = -d.\varepsilon\sqrt{n} \tag{3.50}$$

From Eq. 3.50 it is clear that coupling strength depends on the number of photons. For a coherent laser light field, $|\alpha e^{i\omega t}\rangle$ state, the average number of photons are $\langle n\rangle = |\alpha|^2$, and can be taken as constant for high intensity such that the Poissonian uncertainty is $1 << \Delta n << \langle n\rangle$. Therefore the Rabi frequency Ω_R can be written

$$\Omega_R = \frac{2\,.\,\mathrm{d}.\varepsilon\sqrt{n}}{\hbar}, \tag{3.51}$$

and the expectation value of electric field operator, for the coherent laser field is,

$$E = \langle \alpha e^{i\omega t}|\hat{E}|\alpha e^{i\omega t}\rangle = \left(\varepsilon e^{i\omega t} + \varepsilon^* e^{-i\omega t}\right)\sqrt{n}. \tag{3.52}$$

Thus for the case of linear polarisation and for assuming d and ε real,

$$\hbar\Omega_R = 2.d.\varepsilon\sqrt{n} \tag{3.53}$$

Modified Eigen State

The total Hamiltonian for a two level system, in the basis of $|g, n\rangle$, $|e, n-1\rangle$, under rotating wave approximation (RWA) reads now as follows

$$\hat{H} = \hbar\begin{pmatrix} n\omega & \frac{1}{2}\Omega_R \\ \frac{1}{2}\Omega_R & n\omega - \Delta \end{pmatrix} \tag{3.54}$$

The eigenvalues of $\hat{H}$ gives the modified eigen states of the light-atom system

$$E_1 = \hbar\left(n\omega - \frac{\Delta}{2} - \frac{1}{2}\sqrt{{\Omega_R}^2 + \Delta^2}\right) \tag{3.55}$$

$$E_2 = \hbar\left(n\omega - \frac{\Delta}{2} + \frac{1}{2}\sqrt{{\Omega_R}^2 + \Delta^2}\right) \tag{3.56}$$

It becomes clear from the above two equations that as the atom is moved in the laser beam, there is a light shift for both the excited as well as the ground state. For red detuned laser beam ($\Delta < 0$) , the lower state, which couples to the atom's ground state is lowered in the energy by a shift of $\Delta U_g = -\frac{1}{2}\left(\Delta + \sqrt{{\Omega_R}^2 + \Delta^2}\right)$ and the upper state is up shifted by same amount. In an inhomogeneous light field this corresponds to a spatially varying shift of potential energy, and its gradient gives dipole force. For the intensities lower than the saturation intensity, atom remains in the ground state most of the time. Therefore the light shift (AC Stark shift) in the ground state is the relevant potential for the motion of the atom. For far detuned trapping laser beam ($|\Delta| >> \Omega_R$), a first order approximation of $\frac{\Omega_R}{\Delta}$ gives following expressions of energy shift

$$\Delta U = \pm\frac{{\Omega_R}^2}{4\Delta} \tag{3.57}$$

The new eigen states due to coupling between $|g, n\rangle$ and $|e, n-1\rangle$ are,

$$|1, n\rangle = \left(1 - \frac{{\Omega_R}^2}{8\Delta^2}\right)|g, n\rangle + \frac{\Omega_R}{2\Delta}|e, n-1\rangle \tag{3.58}$$

$$|2, n\rangle = -\frac{\Omega_R}{2\Delta}|g, n\rangle + \left(1 - \frac{{\Omega_R}^2}{8\Delta^2}\right)|e, n-1\rangle. \tag{3.59}$$

Scattering Rates

The spontaneous decay rate for a transition from excited states $|e\rangle$ i.e. $|1, n\rangle, |2, n\rangle$ to ground states $|g\rangle$ i.e. $|1, n-1\rangle, |2, n-1\rangle$ can be derived from full atomic dipole moment corresponding to these states

$$\Gamma = \frac{\omega^3}{3\pi\epsilon_0\hbar c^3}\left(|\langle e|d_{eg}|b\rangle|\right)^2 \tag{3.60}$$

In the far detuning regime $|\Delta| >> \Omega_R$ and considering only the lowest orders of Ω_R/Δ, the decay rates can be written as follows

$$\Gamma_{11} = \Gamma_{22} = \frac{{\Omega_R}^2}{4\Delta^2}\Gamma \tag{3.61}$$

$$\Gamma_{12} = \frac{{\Gamma_R}^4}{16\Delta^4} \tag{3.62}$$

$$\Gamma_{21} = \Gamma \tag{3.63}$$

It can be seen that atom stays mostly in the state $|1, n\rangle$ due to $\Gamma_{21} >> \Gamma_{12}$ and therefore the scattering rate R_s is dominated by Γ_{11}.

3.6 Single Atom Dipole Trap

The loading process of a dipole trap, in the presence of MOT beams, suffers dominantly from light assisted two body collisional losses [93] as compared to single particle collisional losses (from the background vapour inside the vacuum apparatus). The number of atoms loaded during the loading process is related to these two dominant loss process by the following rate equation

$$\frac{dN}{dt} = R - \gamma N - \beta^{'} N(N-1) \tag{3.64}$$

where R is loading rate, γ is the single particle loss coefficient which occurs due to collision between a hot background atom to the cold atom in the MOT and $\beta^{'}$ is the coefficient for two body losses due to collision between two cold atoms in the presence of MOT light beams. Since the equation relates the atom number change to loading rate and loss processes, it is clear that $\beta^{'}$ is inversely proportional to volume of the trap i.e. $\beta^{'} = \frac{\beta}{V}$. As described in the reference [93], the volume V can be determined by the trapping beam waist and the temperature of atoms.

$$V = \pi {w_0}^2 z_R ln\left(\frac{1}{1-\eta}\right)\sqrt{\frac{\eta}{1-\eta}} \tag{3.65}$$

where $\eta = \frac{k_B T}{|U|}$. For ^{87}Rb the value of β reported in the far-off-resonance dipole trap is $3 \times 10^{-10}...10^{-9} cm^3/s$ [93] .

For microscopic dipole trap ($w_0 \leq 4\mu$) the two body collisional losses locks the atom number to one in the presence of cooling beams [3, 94]. This collisional blockade mechanism was experimentally demonstrated for the first time by Schlosser et. al. [3]. The requirement of the small microscopic dipole trap for single atom trapping demands the focusing lens with high numerical aperture (NA) to obtain very small beam waist of trapping beam. A more detailed discussion related towards single atom trapping in our set up is given in chapter 4.

3.7 Experimental Setup For Laser Cooling and Trapping

The most important requirement related to manipulation of individual quantum system (atomic system), is to first prepare an isolated atomic system with a control over its external degree of freedom i.e. center of mass motion and a precise addressability of the internal degrees of freedom (internal energy levels). This is achieved by first cooling an ensemble of atoms to microkelvin temperature range, using the standard technique of Magneto-Optical-Trap (MOT) and then superposing a microscopic dipole trap in the region of the MOT . In our case, this is done by first isolating Rubidium atoms from the environment inside a ultra-high vacuum system and then cooling and trapping them using the techniques of laser cooling and trapping. This section describes the various modules of the experimental setup which is developed for aiming towards single atom dipole trap of Rubidium-87.

3.7.1 Vacuum System

We have used a custom made non-magnetic stainless steel chamber as shown in the Fig. 3.8. The chamber is in the shape of do-decagon with 12 viewports along the circumference and

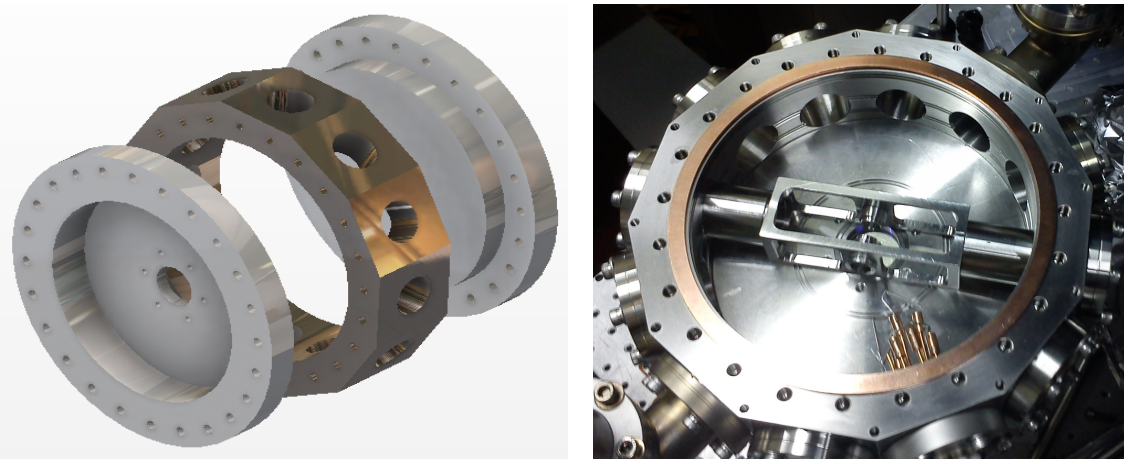

Figure 3.8: The custom made vacuum system to accommodate the high NA lens inside the vacuum.

two viewports at the top and bottom flanges. The top and bottom flanges have a U-shape so that the distance between the anti-Helmholtz coils can be reduced by placing them inside

the U-shaped depressions. This allows to design coils without any need of water cooling which happens due to resistive heating in the coils. To accommodate the high NA lens, for single atom trap and fluorescence detection, a lens mount was built and assembled with the vacuum system, as shown in the Fig. 3.8. The vacuum chamber is connected to a titanium sublimation pump from Varian (916-0061) and to an ion pump (Varian-Diode 9191213, pumping capacity 40 l/s) using a T-connector as shown in the Fig. 3.9. The Rubidium and the Potassium getter sources from SEAS are connected through high current insulation feedthroughs at one of the port. An ionization gauge (Varian-UHV-24) is also installed inside the chamber through one of the viewport to measure the vacuum level inside it.

After standard cleaning procedure for vacuum components, the whole vacuum system was evacuated initially with a turbo-molecular pump (Alcatel ATP-400, pumping capacity 400 l/s) through an auxiliary all metal bakeable valve and baked for one week for a maximum temperature of 200^0C. Baking is required because the metal surface of the vacuum chamber and other components adsorbs and trap gases and water vapour from the atmosphere and therefore needs to be removed by heating the vacuum system while pumping during the process of baking. Electrical heating tapes were used with a current controlled unit to increase the temperature

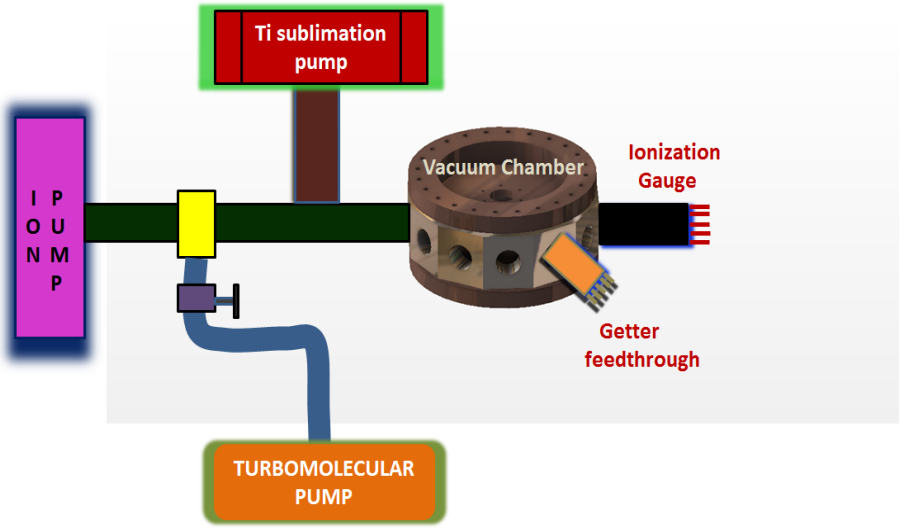

FIGURE 3.9: Complete Vacuum assembly used for achieving ultra-high vacuum inside the vacuum system.

in steps with uniform heating at various part of the chamber. The heating rate was kept low

enough (10^0 C/hr) to avoid unwanted heterogeneous expansion due to temperature gradient, the temperature of the various parts of the vacuum system was also maintained so that not to allow any spatial temperature gradient which is more than 20^0 C. During this first baking the high NA lens were not mounted in the lens holder. After the first bakeout a pressure of 10^{-11} mbar. was achieved. The chamber was then opened to mount the lenses with proper alignment. The whole system was then baked again for a maximum temperature 150^0 C. After this bakeout the final pressure attained inside the chamber was 2.5×10^{-11} mbar. The ion pump was started after the final bakeout to maintain the UHV (ultra high vacuum), while the sublimation pump was used few times to reduce excess Rubidium levels. The all metal gate valve was closed by applying the specified torque and the turbo pump was detached.

3.7.2 Laser Systems and Saturation Absorption Spectroscopy Setup

The hyperfine energy levels for Rubidium-87 D1 and D2 lines are shown in the Fig. 3.10. For Magneto-Optical-Trapping of Rubidium atoms one needs radiation pressure force pointing towards a fixed point in space.

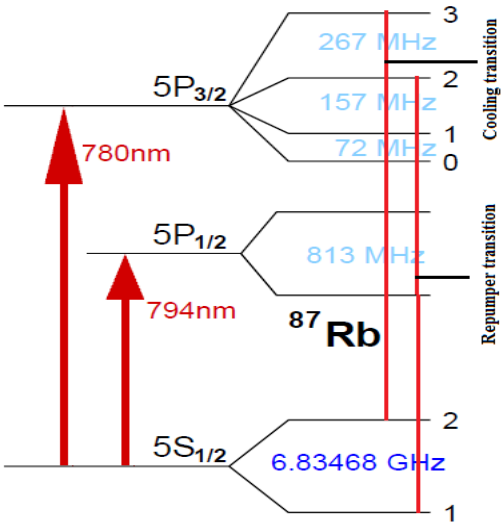

Figure 3.10: Hyperfine transition of Rb87 used for cooling and trapping in the MOT

This requires selection of a cyclic transition to realize a practical two level system. For laser cooling and trapping of ^{87}Rb we use two diode lasers one for cyclic transition $F = 2 \rightarrow F' = 3$ to

cool the atom through radiation pressure force, this is called cooling laser. Another laser is used to repump the atom back to the cyclic cooling transition, which are leaked to other transitions due to various effects such as Doppler broadening, laser linewidth etc. This is called repumper laser. For dipole trapping a far-off resonant laser which is red detuned with respected to D1 and D2 transition of Rubidium, at a wavelength of 852 nm is used. All the lasers used in the experiment are commercially available External Cavity Diode lasers (DL100, Toptica Photonics) with a very

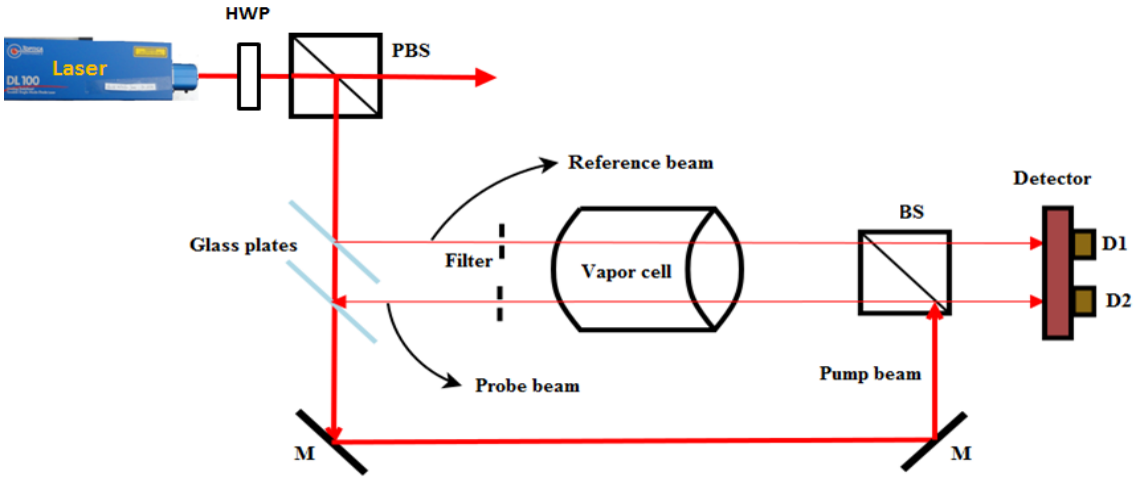

FIGURE 3.11: Saturation absorption spectroscopy setup used in the experiment

narrow linewidth approximately 1 MHz. For some cases, where a higher power of dipole trapping beam is required, some part of the dipole trapping laser is injected to a commercially available tapered amplifier chip of BOOSTA (from Toptica photonics). A brief description about the different laser systems with their spectroscopy setups is presented in the following sections.

Saturation Absorption Spectroscopy (SAS) is an excellent technique to resolve the hyperfine levels, which are few 10 to 100 MHz apart, and are not resolvable otherwise in a conventional absorption of a single probe beam through the vapor of the atoms. This is due to the Doppler

broadening of the transitions, which is of the order of few GHz and results in a broad Doppler profile.

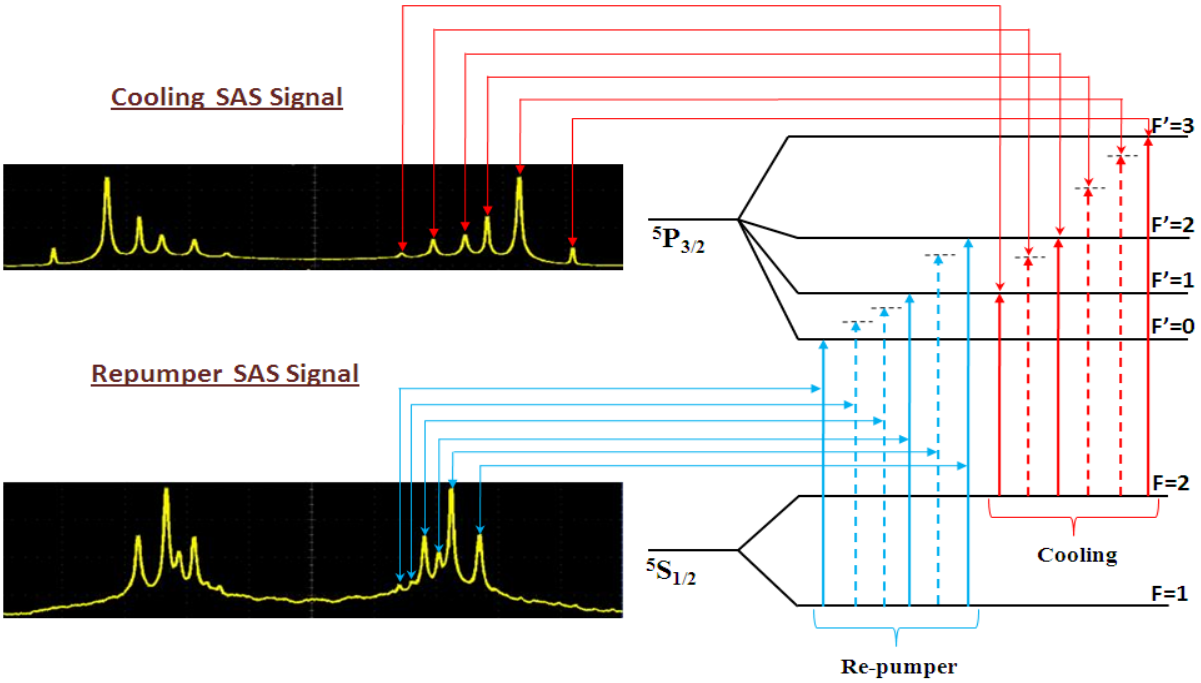

Figure 3.12: Saturation Absorption Signal for Rb87 cooling and repumper hyperfine transition.

The hyperfine levels are resolved in SAS by detecting the absorption of a weak probe on a photodiode in the presence of a counter propagating strong pump field. Both the pump and the probe, are derived from the same laser beam. As the laser frequency is scanned through the hyperfine transitions, the pump and probe addresses the same velocity class of atoms when
1) the laser frequency matches with one of the resonance frequency (ω_i) of the atomic transition
2) cross over frequencies ($\omega_1 + \omega_2$) i.e. a transition frequency which is midway between two resonance transition frequencies ω_1 and ω_2.
Due to the presence of a strong pump beam, the probe beam sees an enhanced transmission. This is due to saturation of the transition by pump beam for the case when both beams addresses the same transition. This is called a Lamb dip. Now the hyperfine peaks are observed on top of the Doppler broadened profile.

Fig 3.11 shows the SAS setup used. A small part (power 1 mW) of the main laser beam is used for SAS. This beam is partially reflected by two glass plates to get two weak beams, one is

used as reference beam and other is used as probe. Both the beam passes through the vapour cell and incident on two balanced photodiodes. The reference beam contains only the Doppler broadened profile of the thermal atomic vapour of ^{87}Rb. Probe beam which counter propagate against the pump beam has hyperfine level dips on top of the Doppler broadened profile. The difference of the two photodiode signal gives a Doppler free hyperfine spectrum.

Cooling Laser

Cooling laser is tuned across the hyperfine transitions $F = 2 \rightarrow F' = 3, 2, 1$. For MOT operation this laser is locked at the $F = 2 \rightarrow F' = 3$ hyperfine transition peak of the SAS signal. This is a closed transition for a ^{87}Rb atom which is at rest and excited by an narrow linewidth laser beam because an excited atom to $F' = 3$ cannot de-excite to the other hyperfine ground state ($F = 1 \rightarrow F' = 3$ transition is forbidden). Fig. 3.12 shows a Doppler free SAS signal for ^{87}Rb. The full beam alignment for cooling laser is shown in the Fig. 3.13 The laser beam, after sending a small part to the SAS setup, is double passed through a 100-40 MHz AOM-1 (Isomet) at its 1^{st} order diffracted beam. This allows to change the detuning of the cooling beam without affecting the beam alignment. This double-passed beam is fiber coupled and then guided to the MOT chamber using single mode polarization maintaining fiber. The waist of the beam at the output collimator is around 2.0 mm. A small waist is must to avoid the clipping of the beam from the high NA lens inside the chamber. This reduces the background scattering. The total power at the output coupler is around 20 mW.

The 0^{th} order diffracted beam of the AOM-1 is also double-passed through another 100-40 MHz AOM-2 (Brimrose). This beam is also fiber coupled using a single mode fiber and used as a probe beam. This is send along one of the cooling beam and along the axis where camera is installed. AOMs used along the beam paths are used as fast switch to switch on/off the beams. Additionally mechanical shutters are also used which were made out of the computer hard disks. These mechanical shutters are obtained from the hard disks of the computers and an electronic circuit is built to control these shutters using TTL pulses generated from the Labview. For MOT operation cooling laser is locked at second crossover of the cooling SAS signal, AOM-1 is operated at 94 MHz while AOM-2 is operated at 105 MHz.

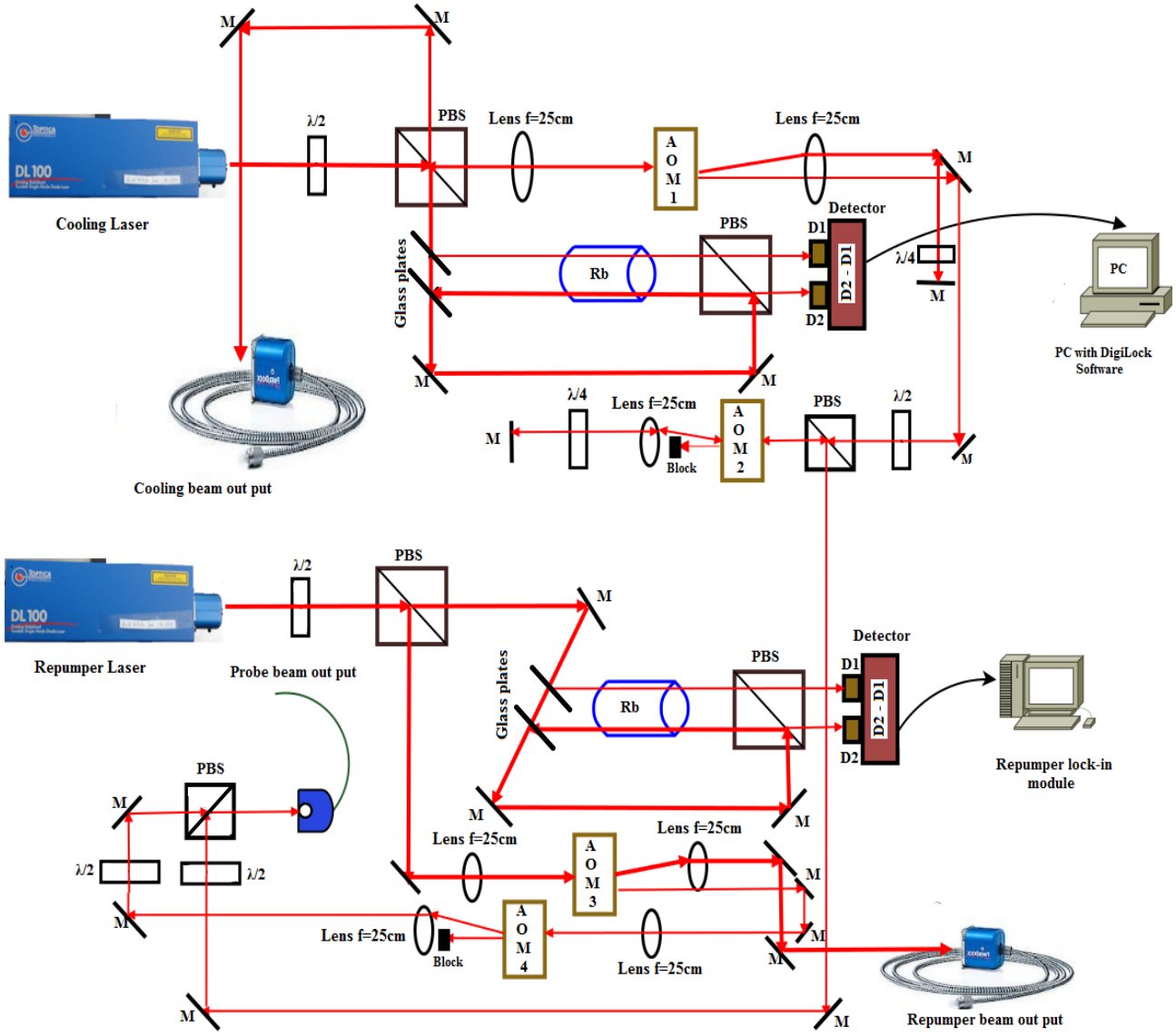

Figure 3.13: The full optical layout for the cooling and the repumper lasers along with their respective saturation absorption spectroscopy setups

3.7.3 Repumper Laser

The repumper laser for ^{87}Rb trapping is tuned to address the hyperfine transitions $F = 1 \rightarrow F' = 2, 1, 0$. SAS signal for ^{87}Rb repumper transitions is shown in the Fig. 3.12 The full optical alignment of repumper laser beam is shown in the Fig. 3.13. A small portion of the beam (1 mW) is used for SAS. The remaining power is passed through a 80-40 MHz AOM-3 (Brimrose). The first order diffracted beam is fiber coupled using single mode fiber and send to the MOT

chamber. The zeroth order beam of AOM-3 is single passed through another 80-40 MHz AOM-4 (Isomet) and fiber coupled in a single mode fiber along with cooling probe beam. The laser is locked at first crossover peak for the MOT operation.

3.7.4 Anti-Helmholtz Coil

The MOT of neutral atom needs spatially varying inhomogeneous magnetic field with a spherical quadrupole magnetic field lines. This is achieved by a pair of anti-Helmholtz coils i.e. coils with opposite current flow. These coils are made up of 18 gauge insulated copper wire. The frame for the coil has a inner radius of 4 cm and outer radius of 8.3 cm, so that it fits inside the depression on top and bottom of the flanges. There are 23 layers of copper windings with 23 windings in each layers. The resistance of each of the coils is 3Ω and inductance is 30 mH. These coils can generate a magnetic field gradient of 10 Gauss/cm-A at the center of the chamber, where MOT is formed. The coils doesnot require water cooling when operated at a current upto 3.5 amperes.

The switching of current in the coils is done by a transistor-based switching circuit. The rise and fall time of the currents in the coil is around 1 ms and 200 μs respectively.

3.7.5 Compensation Coils

Three pairs of Helmholtz coils are used along the three perpendicular axis to compensate the earth's magnetic field as well as residual fields at the MOT position. These are made up of the standard ribbon cables strips having 10 adjacent wires (Fig. 3.14) Using end to end connectors, the different wires are connected in series to get a coil with 10 turns. One pair of the coil can also be used for a bias field so as to define the quantization axis. Each pair of coil generates around 1 Gauss magnetic field at the center of the chamber at a current of 1 ampere.

3.7.6 Setup for Magneto Optical Trap

Fig. 3.15 shows the full MOT beam alignment layout on the vacuum chamber which is used for Magneto-Optical-Trapping of the ^{87}Rb atoms. The beams in the x-y plane are at 56° instead of the standard orthogonal geometry of the beams. This is due to the presence of the lens mount inside the chamber which has to accommodate the lenses with small working distance (which is

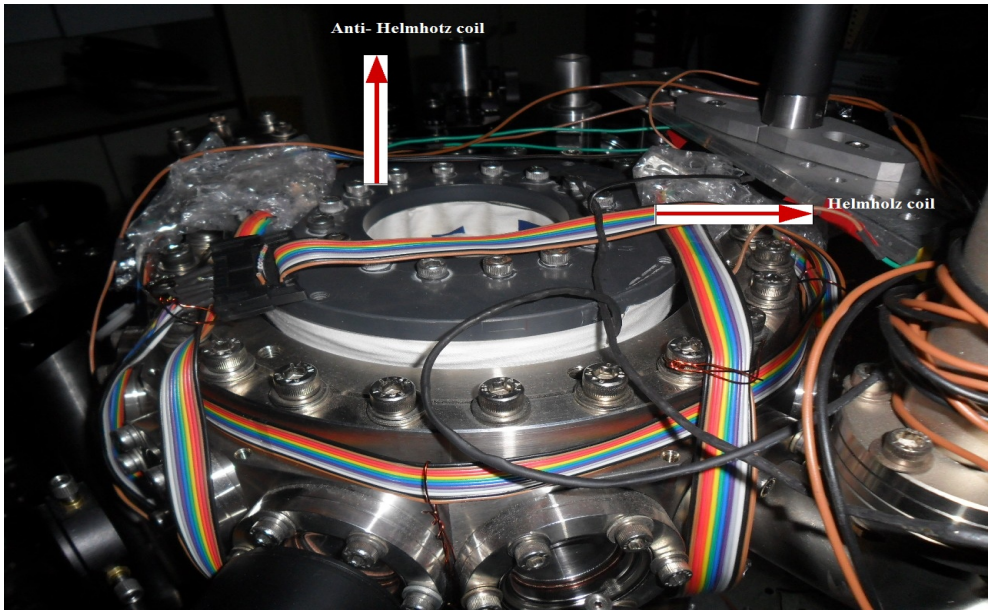

Figure 3.14:

only about 5.5 mm). The beam size is kept around 2mm to avoid scattering at the lens mount. A third beam is sent along z- direction, perpendicular to the plane of the x-y beams. Anti-Helmholtz coils are also placed along this direction.

The laser beams from cooling and repumper output couplers are combined on a polarizing beam splitter. One part of this is sent for z-axis MOT beam. Another part is further divided into two beams using a half wave plate and polarizing beam splitter, to be used as the MOT x and y beams. Three quarter wave plates are kept in the path of the beams before they enter the chamber. Their axis are set such that they generate circularly polarized light with same helicity with respect to magnetic field lines. The MOT beams are retro-reflected on the other side of the chamber. A quarter wave plate is also inserted at each retro reflected beam to make them opposite circular polarization with respect to input beam.

3.7.7 Computer Control and Automation

The cold ensemble of atoms produced in the MOT should be characterized for its temperature, atom numbers, density etc. This enables the use of this system further for efficiently loading atoms in other types of traps or for other various experiments with the MOT. Measurement of

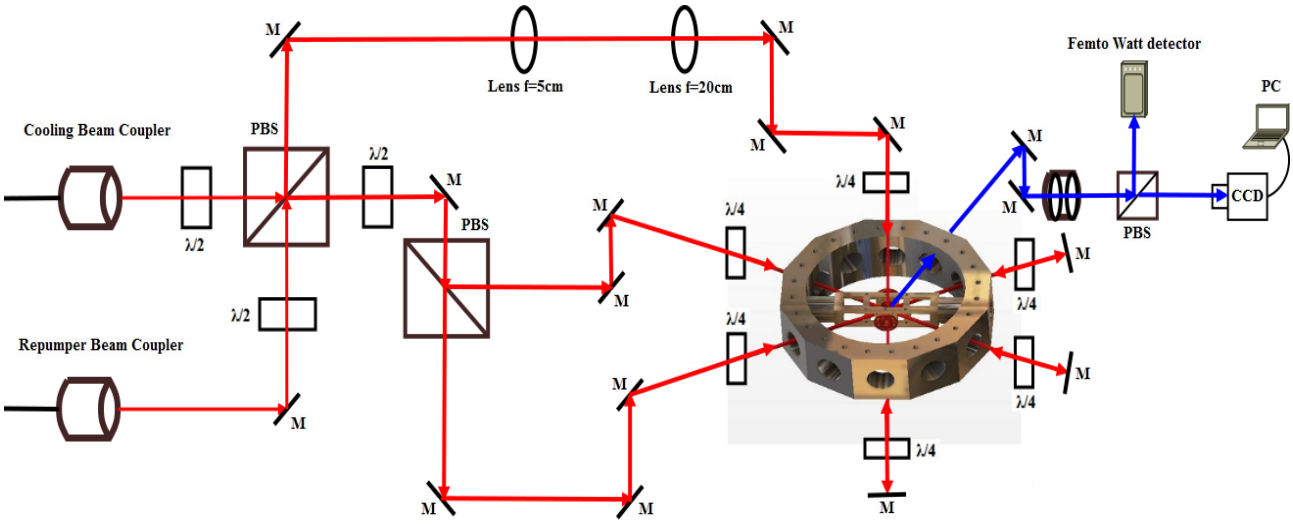

FIGURE 3.15: The Schematic for optical beam alignment in the MOT

parameter like temperature of the MOT relies on measuring the momentum distribution of the atoms in the MOT. The usual method for that is to allow the MOT to ballistically expand in the absence of cooling and trapping forces for a given time.This requires a precise control over the MOT loading on/off time, MOT coils switching, camera triggering and MOT beams as well as probe beam on/off timing with all of them synchronized with a given timing reference.

In our experiment the various timing sequences, analog as well as digital, are generated using PCI based card from National Instruments (NI) and interfaced with the experiment using Labview program. Usually Labview based programs to generate electronic sequences are not real time and have rather very low timing resolution (not even few millisecond). The M-Series PCI cards have on board memory option with FPGA (Field Programmable Gate Array) based platform. We exploit this by first generating a timing sequence waveform for various digital and analog channels available on the cards PCI-6251/6259 based on the clock frequency of either an external function generator or the clock frequencies which are available on the card itself. Once the timing sequence is generated, it is dumped onto the respective output channels by giving a clock trigger to the card. This method generates well synchronized timing sequences with a minimum time interval decided by the frequency of the clock and synchronization accuracy better that 10 nanosecond. Generally we use a clock frequency of 10 KHz which gives a minimum time interval of 100 microsecond

and a maximum time interval of 3 minutes without a loss of synchronization accuracy of 10 nano second. For lower time intervals, higher clock frequencies are used. As one goes for higher clock frequencies the maximum time interval which can be generated is limited by the on-board memory of the card. Initially card PCI-6251 was used for the automation of the experiment. This card has only two analog output channels. To get more analog outputs we have used another card PCI-6259 installed in a separate PC. The two cards installed in two different PCs are synchronized with each other using same clock frequency for both the cards which is generated by PCI-6251. We have a total 6 analog outputs and more than 10 digital outputs which are synchronized.

For switching the MOT coils on and off, transistor based switching circuits are used (Appendix:-D). Digital switching or analog ramping of the MOT beam parameters (frequency and intensity) is done by feeding the output of the digital or analog channels (PCI 6251 card) to modulation or frequency port of the AOM driver. The Camera used for quantitative measurement is EMCCD from Princeton Instruments. The PCI controller card for the camera system is installed in a separate PC and one of the digital line from M-series PCI cards is used to control the exposure time as well as the imaging time sequences.

3.8 Characterization of the MOT

Getting the MOT

The MOT beams used in our setup have a waist of 2 mm; this small beam size is chosen to avoid clipping and therefore scattering from the lens mount. Due to this small beam size and the inclined geometry of the beams along the xy-plane, the beam alignment is very crucial to load atoms efficiently in the MOT directly from the room temperature rubidium vapor. First the beam heights on the xy-plane is adjusted to keep the two beams perfectly on the same horizontal plane. This is done by passing the maximum light through a 500 μm pinhole (which is kept at the height of the focus of the high NA lens) on both sides of the chamber. The angle between the beams along the xy-plane is around 56°, therefore the beams do not pass exactly through the center of the viewport but are adjusted to minimize the clipping from the lens mount. The final alignment of the MOT beams is done by looking at the fluorescence of the atoms along

these beams from two or more different viewing angles. A constant current of 2.7 A. is passed through the getter for 15 minutes to get enough Rb atoms inside the chamber and to get a clear visible fluorescence tracks along the beam directions. The beams then are adjusted slightly to maximize the intersection volume at the center of the chamber. For increasing the accuracy, the same procedure is repeated by reducing the beam size iris size by placing irises concentric to the beams. The retro-beams are aligned by looking their reflection on the irises at the input side of the chamber. Provision for placing two lenses of focal lengths $f_1 = 5cm$ and $f_2 = 25cm$ is made to get expanded beam along the z-direction. This is useful because the probe beam is send along the z-axis and the MOT dynamics during ballistic expansion can be observed for longer duration.

After the MOT beam alignment, the cooling and repumper lasers are locked on appropriate peaks (described in section 3.7.2) of the SAS signals. The cooling beam is kept red detuned about 2 to 4 Γ w.r.t. cooling transition $F = 2 \rightarrow F' = 3$, where Γ is linewidth of the excited state cooling transition. Repumper is locked exactly on resonance to the $F = 1 \rightarrow F' = 2$ transition. Initially the MOT coils are operated by two independent power supplies so as to adjust the minimum magnetic field point if it doesn't intersect with the intersection point of the MOT beams. The current in the coils is kept around 2.2 Amperes. which creates a high magnetic field gradient of around 22 Gauss/cm. The getter is operated at 2.5 Amperes. A surveillance type CCD camera is place along the lens mount axis as shown in the Fig 3.15. A bright spot at the center of the chamber appears due to florescence of atoms trapped in the MOT. It was observed that the equal current is required for both the MOT coils. The MOT coils are then driven by same power supply. Now the current magnitude and the direction in the three pairs of the compensation coils is adjusted such that the MOT position doesn't shift with changing current in the MOT coils. In this condition ballistic expansion of the MOT happens with no shift in its center except due to free fall under the gravity which is small. For these observations an imaging system with a magnification of 1 is built and the CCD camera was replaced by a low noise and temperate stabilized EMCCD camera from Princeton Instruments is used details of which are given in the Appendix:-B.

Imaging system for the MOT

The characterization of the various MOT parameters like density, atom number, temperature etc. requires collection of the fluorescence light from the trapped atoms and suppressing the background scattered light. This is achieved by spatial filtering of the MOT florescence by placing an iris at the focus of the objective lens in the imaging system. Here the objective lens was from Nikkor (NIKKOR-55-200-1:4-5.6G). The iris of this objective lens is fully opened. The light collected from this lens is focused on a pinhole 500 μm. The image of this pinhole is focused on the PI-Acton camera as well as on the Femto-watt detector from New Focus with a gain of 2×10^{10}.

3.8.1 Fluorescence Detection of Trapped Atoms

The fluorescence collected from the trapped atoms through the imaging system is detected on the EMCCD camera as well as on the Femtowatt photo diode. The quantitative estimation of the atom numbers in the MOT is done by converting the Femto-watt detector signal level into corresponding photon numbers from the MOT. Then by knowing the scattering rate of a single Rb atom and the collection efficiency of the imaging system, one can estimate the total number of atoms present in the MOT. First the MOT is loaded from the atomic vapour. The loading curve during the MOT loading process, shows an exponential rise towards a saturation value analogous to the curve for charging of a capacitor, this is discussed in the next section. When the MOT signal reaches to its saturation value, the MOT is in an steady state. The total number of atom in the trap in this condition is calculated as follows.

The total number of photons scattered from an atom inside the trap is given by

$$R_{sc} = \frac{\gamma}{2}\left(\frac{I/I_s}{1 + I/I_s + [\frac{2(\Delta + kv_x}{\gamma}]^2}\right) \tag{3.66}$$

The spontaneously scattered photons are isotropically distributed in the full 4π solid angle. Therefore the total number of photons scattered from the cold atom ensemble can be deduced by collecting the photons in a given solid angle subtended by the imaging system with respect to the MOT. If the radius of the lens aperture which collects light from the MOT is r and distance from the center MOT is d, detector sensitivity is K volt/Watt and the T_t is the total transmissivity

of all the optical elements present between the MOT and the Femtowatt detector and V is the signal voltage at the photodiode. Then the number of atoms in the MOT is calculated from the following expression

$$N = \frac{4Vd^2}{Kr^2 R_s c\hbar\omega T_t} \tag{3.67}$$

The total number of atoms estimated in the MOT is 2×10^4.

3.8.2 Loading and Decay of the MOT

The dynamics of the MOT is governed by three important factors in the trapping process. The capture rate of the atoms in the trap, the loss rate of the atoms from the trap due to collision from the background atoms of the thermal vapor and two and three body collisions loss inside the MOT due to light assisted collisions. Equilibrium between the loading process and loss

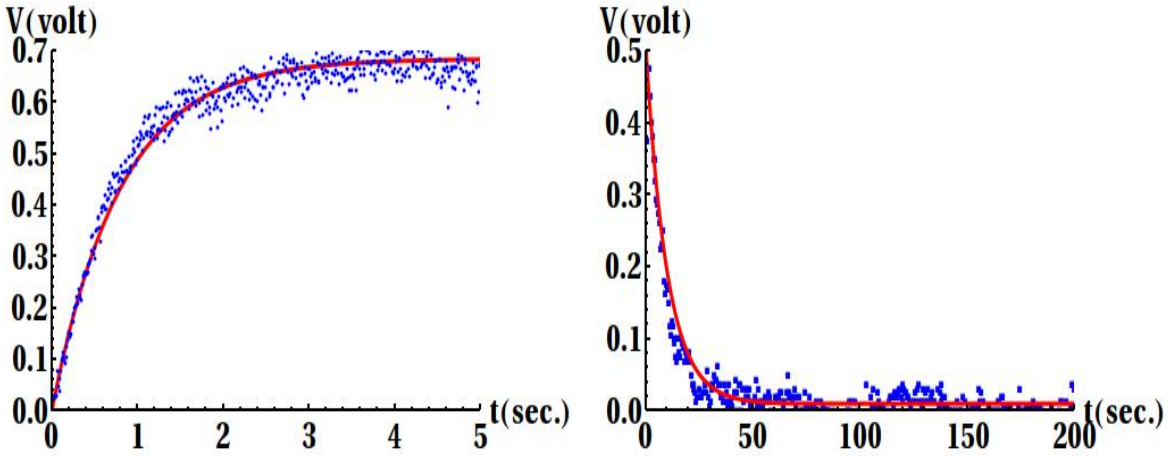

FIGURE 3.16: loading and decay of the vapor loaded MOT in our setup

mechanism decides the number of atoms in the MOT when it saturates. In a vapor loaded MOT under low pressure condition, only the atoms lying in the low energy tail of the Maxwell-Boltzmann distribution are cooled and trapped. Except under certain conditions, inter-collisions between the trapped atoms can be ignored in this type of MOT. The dominant loss mechanism is then mainly due to the collision with the room temperature background gas. The number of

atoms in the MOT increases with the following form

$$N(t) = N_0(1 - e^{-t/\tau}) \tag{3.68}$$

where τ is the time constant for the atom number saturation in the MOT. This also represents the average time for an atom to remain in the trap before it gets kicked out by a thermal background atom. The time constant τ can be expressed in terms of the cross section, density and velocities for Rb and background components as follows [95]

$$\frac{1}{\tau} = n_{Rb}\sigma_{Rb}v_{Rb} + n_b\sigma_b v_b \tag{3.69}$$

Fig. 3.16 shows the photodiode signal in time during the loading process of the MOT. The curve fitting into this data gives a loading time of around $0.8s$ and decay time of $13s$. The getter current was 2.8 A for this particular data. The decay curve is obtained by switching off the Rubidium source at $t = 0$ but the MOT is always on. The decay in that case is mostly governed by collision from the background atoms.

3.8.3 Number of Atoms and Density of the MOT using Absorption Imaging and Fluorescence imaging using EMCCD

The density of the MOT is calculated from the images taken using EMCCD camera. The size of the MOT is estimated by fitting a Gaussian to the MOT image as shown in the Fig. 3.17. As the magnification of the imaging system is known, the density of the MOT is calculated from the number of atoms obtained in the MOT by fluorescence detection technique. Assuming the distribution of atom in 3D is given by Gaussian density distribution given by

$$n(x, y, z) = n_0 \exp\left(-\frac{x^2}{{\sigma_x}^2} - \frac{y^2}{{\sigma_y}^2} - \frac{z^2}{{\sigma_z}^2}\right) \tag{3.70}$$

where σ_x, σ_y, σ_z are the $1/e$ radii of the cloud in respective direction and the peak density n_0 is given by

$$n_0 = \frac{N}{\pi^{3/2}\sigma_x\sigma_y\sigma_z} \tag{3.71}$$

The density in our MOT is estimated around $\sim 8 \times 10^8 cm^{-3}$.

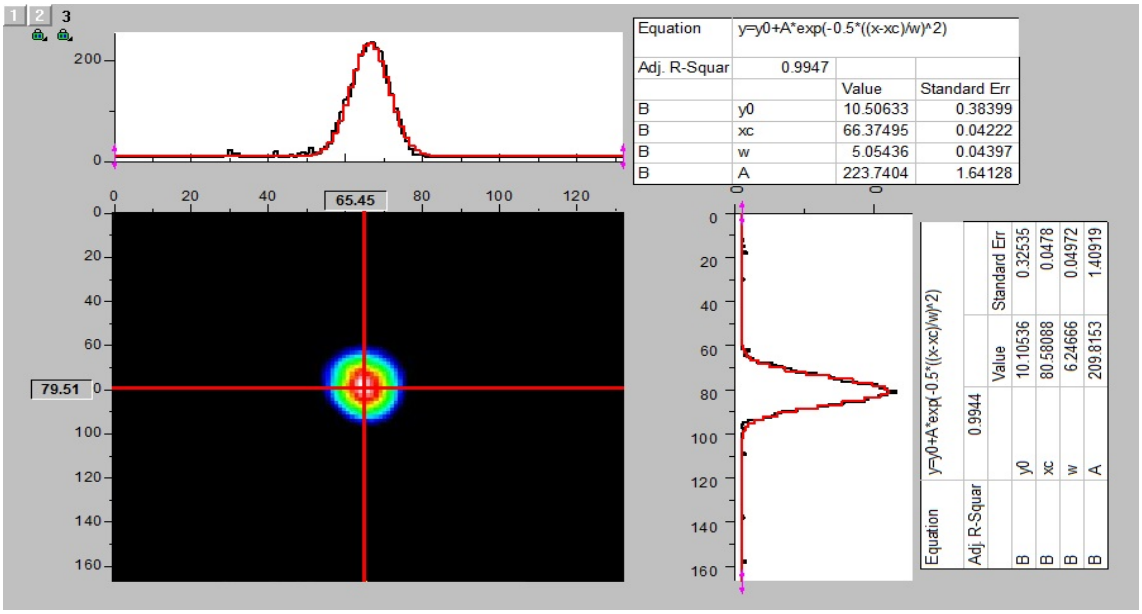

FIGURE 3.17: The fluoresence image of a cold cloud of ^{87}Rb atom in the MOT.

3.9 Temperature Measurement of the MOT

Temperature is a physical quantity for the state of a thermodynamical system which is closed and is in equilibrium with its surroundings. The average kinetic energy of the particles in the system is related to the system temperature as follows

$$\langle E \rangle = \frac{3}{2} k_B T \tag{3.72}$$

The atoms in the MOT are not in thermal equilibrium with its surroundings because there is vacuum inside the chamber. The exchange of energy happens due to momentum transfer from atom to photons. As the photons are not a form of heat energy, the temperature of the MOT atoms can be determined by measuring position, velocity or energy distribution of the cold ensemble of atoms. The three different techniques in general used for MOT temperature measurement is discussed in the following section.

3.9.1 Trap Oscillation Method

This is a non-destructive and online temperature measurement technique for the MOT. The analysis presented here is based on reference [96]. In the trap oscillation method an oscillating bias field is applied so that the magnetic field minimum of the spherical quadrupole field oscillates with the external bias field. The MOT atoms follow this oscillatory motion with a phase lag. Therefore the system can be described by a classical damped harmonic oscillator.

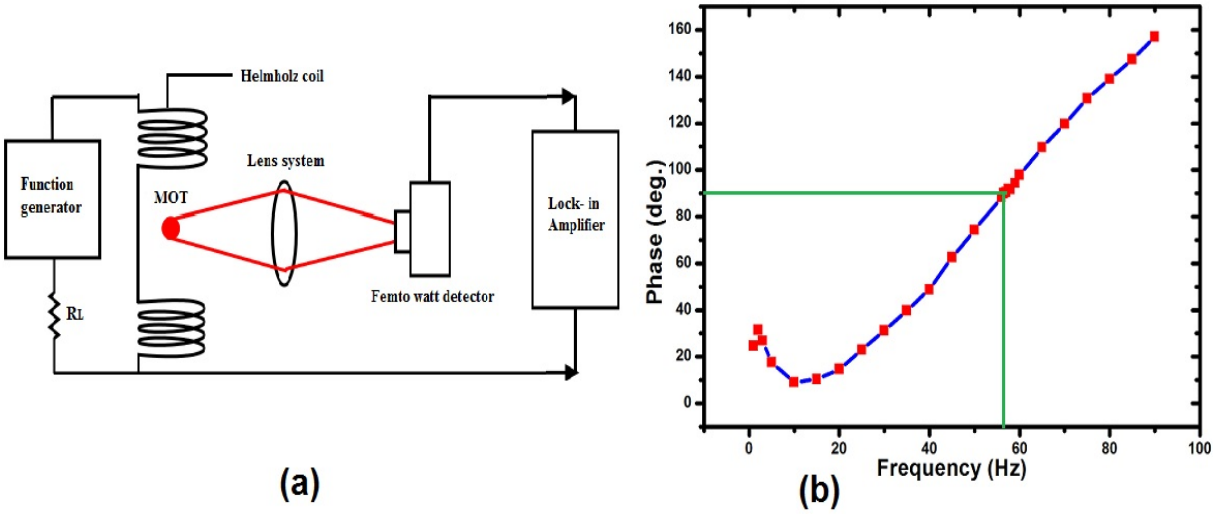

Figure 3.18: (a) Experimental setup for trap oscillation method of temperature measurement of the atoms in the MOT. (b) the measured values of phase difference between the applied oscillation to magnetic field and the oscillation of the MOT.

The equation of motion for a damped harmonic oscillator can be written as

$$F(t) = -\kappa x(t) - \alpha v(t) + f(t) \tag{3.73}$$

where κ is the spring constant for the harmonic motion, α is the damping coefficient and $f(t)$ is the external driving force

$$f(t) = f_0 \cos \omega(t). \tag{3.74}$$

Trail solution

$$x(t) = a_0 \cos(\omega t - \phi), \tag{3.75}$$

gives

$$a_0 = \frac{f_0}{\sqrt{(\kappa - m\omega^2)^2 + \alpha^2\omega^2}} \tag{3.76}$$

and

$$\tan\phi(\omega) = \frac{\alpha\omega}{\kappa - m\omega^2}. \tag{3.77}$$

Measuring the phase or amplitude as a function of the frequency gives the values of the constants α and κ. As the analysis till now assumes linear approximation i.e. harmonic force linearly depends on the displacement, the displacement of the MOT from the center should be small.

At thermal equilibrium the relation

$$k_B T = \kappa\langle x^2\rangle = m\langle v^2\rangle \tag{3.78}$$

yields the temperature of the MOT once κ is known.

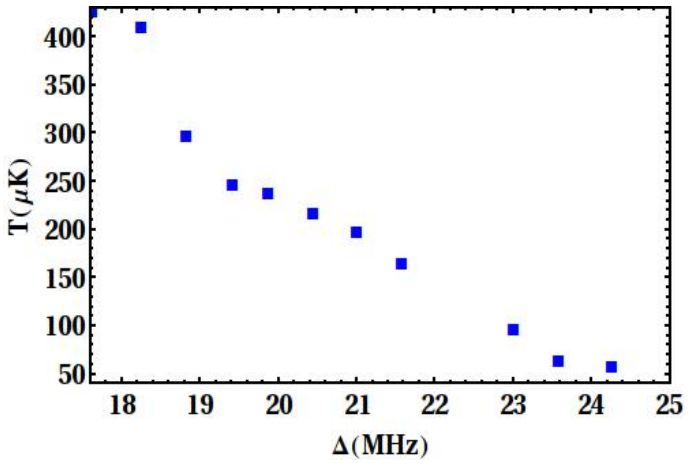

FIGURE 3.19: Temperature vs. detuning, measured by the trap oscillation method.

Fig. 3.18 (a) shows a schematic of the experimental setup used for the trap oscillation method. A modulating signal is generated from the function generator and amplified using a power amplifier circuit. This modulating signal is applied to a pair of Helmholtz coils along one of the axis. This periodically shifts zero point of the magnetic field. The change in the MOT position is detected

by Femto-watt detector signal. The phase difference between the input modulating signal from the function generator and the Femto-watt detector signal is measured using Lock-in amplifier (SRS-850). Fig. 3.18 (b) shows a plot between phase (w.r.t. external signal) of the photodiode signal, looking at the MOT fluorescence, vs. the frequency of the trap oscillation. The value of the frequency for which the phase difference is 90^0 is 57 Hz. From this the value of the κ is calculated using Eq. 3.77 and the value of the temperature is determined from Eq. 3.78. The temperature of the MOT measured using this method is $260\mu K$. The effect of the detuning (Δ) of the cooling laser on the temperature of the MOT is studied as shown in the Fig. 3.19. The detuning (Δ) is measured with respect to cooling transition $F = 2 \rightarrow F' = 3$ and is red detuned.

3.9.2 Release and Recapture Method

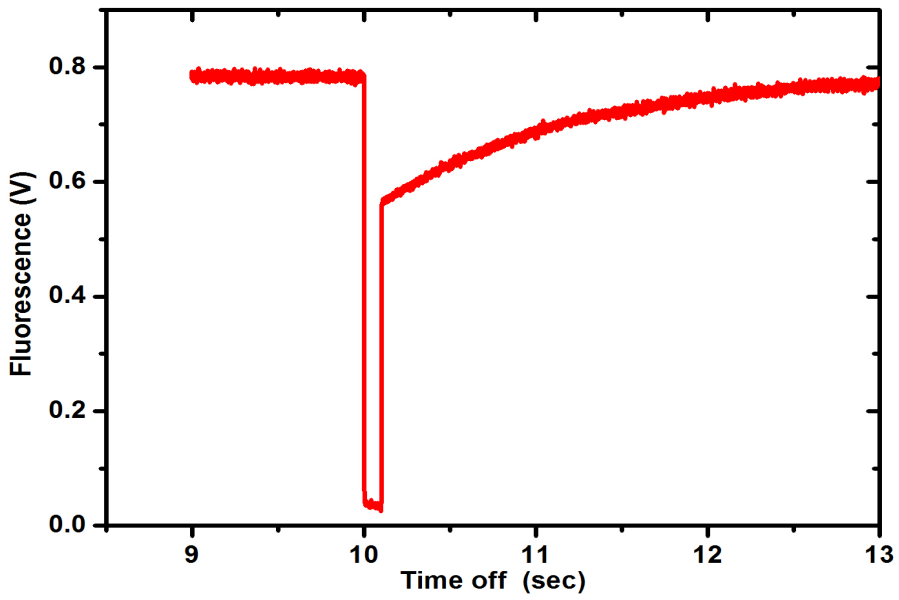

Figure 3.20: Photodiode signal during MOT release and recapture process

Release and recapture is an easy method for MOT temperature measurement. This method was first used by Chu. et. al [82] to estimate the temperature of the optical molasses in a Doppler cooling process. The method is now used for determining the temperature of the cold ensemble of atoms in MOT or dipole trap. The advantage of this method is that it doesn't

require any imaging of cloud instead the recorded fluorescence signal on a photodiode during the whole process is enough to deduce the temperature of the cold atomic sample.

In the release-recapture method the trapping potential is switched off non-adiabatically and the cold ensemble is allowed to expand freely for a short time interval. The trapping potential is then switched on and recaptures the remaining atoms which are present in the trap volume. The hotter atoms leave the trapping volume with a higher velocity. The off time in which a substantial fraction of the trapped atoms leave the trapping region, can be used to estimate the temperature of the atoms in the MOT. The precise determination of the temperature by this method requires a good estimation of the trapping volume and the numeric modelling of the expansion process with known energy distribution.

In our setup we start with 2×10^4 atoms in the MOT which is collected on Femtowatt detector using the imaging system. The MOT was then switched off for variable times by switching off the MOT beams using AOMs and magnetic field using switching circuit. The fluorescence from the remaining atoms in the trap is then recorded (Fig. 3.20).

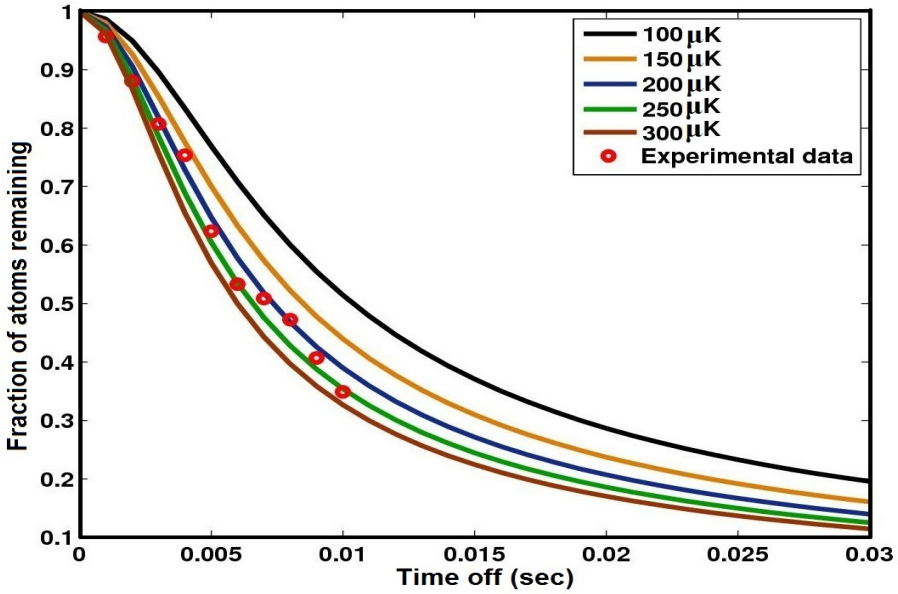

FIGURE 3.21: Temperature estimation by MOT release and recapture method

During the free ballistic expansion of the cloud the gaussian profile changes to different gaussian

profile which depends on the initial temperature of the MOT.

$$\sigma^2(t) = \sigma^2(0) + \frac{k_B T}{m} t^2 \tag{3.79}$$

where $\sigma(0)$ is the initial size of the cloud , $\sigma(t)$ is the size of cloud after expansion for time t, k_B is the Boltzmann's constant and m is the mass of the atom. The fraction of the atoms remained in the trap are given by

$$\frac{N(t)}{N(0)} = \left(1 + \frac{k_B T}{m\sigma^2(0)} t^2\right)^{-\frac{1}{2}} \frac{\int_0^{r_0} \exp\left(-\frac{x^2}{2\left(\sigma^2(0)+\frac{k_B T}{m}t^2\right)}\right) dx}{\int_0^{r_0} \exp\left(-\frac{x^2}{2\sigma^2(0)}\right) dx} \tag{3.80}$$

where $N(0)$ is the initial number of atoms in the trap, $N(t)$ is the remaining number of atoms in the trap when it is switched back on after a time t off for the potential. r_0 is the radius of the detection region. In the experiment $r_0 = 0.5$ mm, $\sigma(0) = 400\,\mu m$ and the ratio $\frac{N(t)}{N(0)}$ is obtained from the ratio of the voltages for the Femtowatt detector output. For various off-time intervals this ratio is compared with the theoretical curves for off-time versus fraction of atoms (Eq. 3.80). This is shown in the Fig. 3.21.

3.9.3 Ballistic expansion method

In this method, the cold ensemble of atoms in the MOT, is allowed to expand freely for variable time intervals after switching of the trapping fields. The expanded cloud is imaged using MOT beams itself but with a short exposure time of 100 μs. The initial and final sizes of the cloud are used to deduce the temperature from the Eq. 3.79. Fig 3.22 shows the expansion of the cold cloud for different expansion times. The temperature estimated by this method is around 255μ K.

3.10 Conclusion

This chapter gives a discussion of the necessary theoretical concepts regarding the laser cooling and trapping of neutral atoms. A description of the experimental set-up for the MOT is given. The various parameter of the MOT has been observed in the set-up to understand the trap characteristics. Atom numbers, temperature and the loading, decay characteristics of the MOT

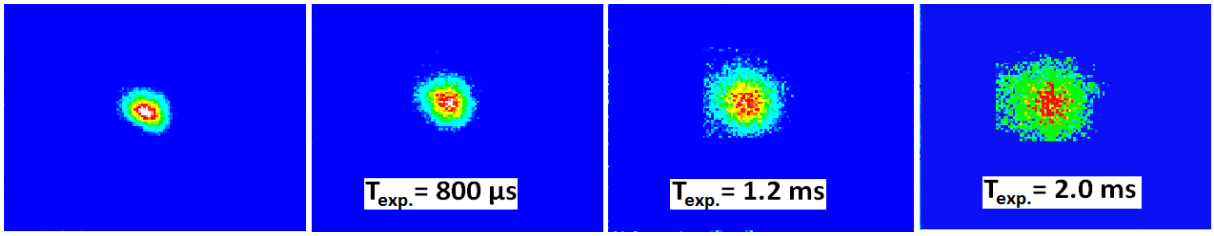

FIGURE 3.22: Images of the cold atom cloud before and after different expansion times.

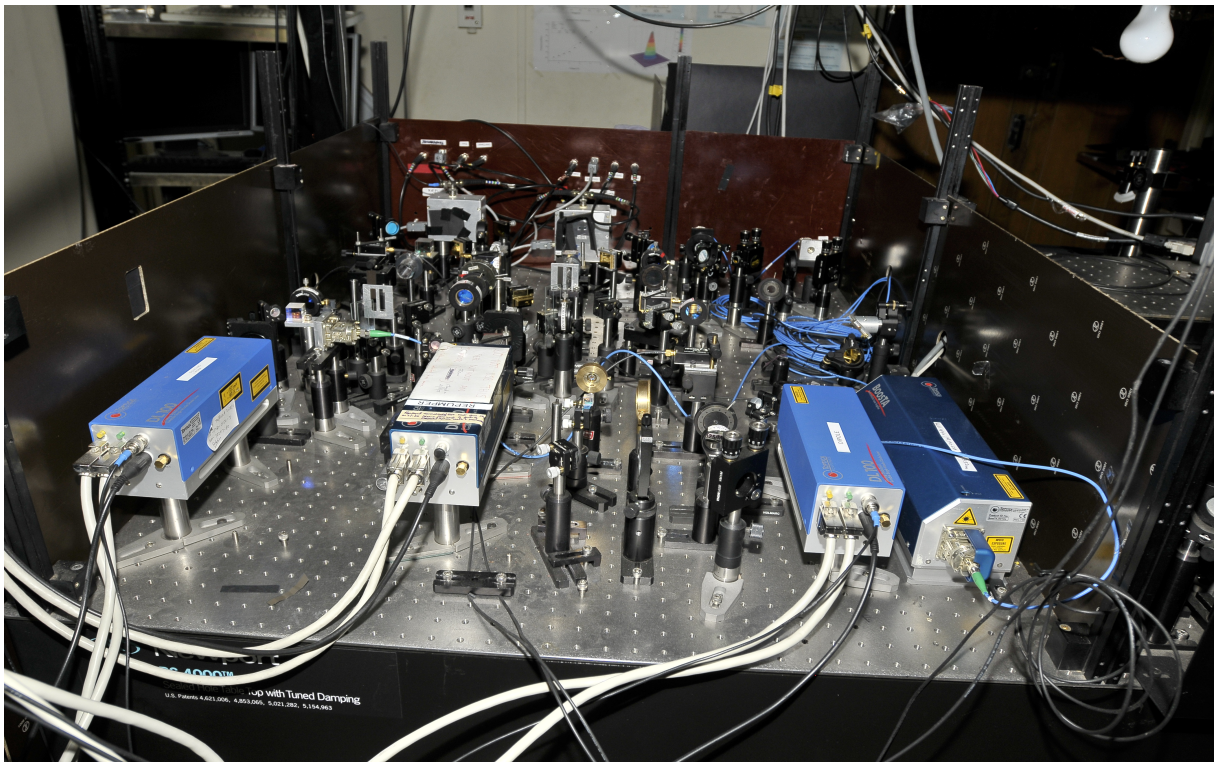

FIGURE 3.23: Full layout of the laser system with optics alignment.

for one particular set of parameters is presented. The final aim of this experimental set-up is to load an ensemble of cold atoms of ^{87}Rb which is fast, efficient and deterministic for single atom dipole trap loading.

4

Chapter 4

4.1 Towards a Single Atom Trap

4.1.1 Introduction

The behaviour of the individual atom, which are the basic constituent of the matter, is governed by the laws of quantum mechanics. In general an individual atom cannot be in isolation and it interacts with other atoms to produce the matter around us, whose properties can be described in classical physics frame work. Therefore to study the precise dynamics and the interaction between the atoms at quantum level requires to prepare isolated controlled quantum systems. This is the reason that manipulation of individual quantum systems is one of the most vibrant fields of modern experimental physics. This facilitates a platform to study a whole range of quantum mechanical phenomena which appears to be bizarre and very much counter-intuitive in

the classical mechanics framework. Some of the applications of the individual quantum systems are in quantum information processing as well as in the studies of fundamental laws in quantum domain.

The first direct observation of an individual microscopic particle was reported by Wilson in his cloud chamber [97]. Based on the idea of Dehmelt [98], Neuhauser et. al. [99] demonstrated trapping of single or few Ba+ ions in an ion trap, which uses electromagnetic potentials to overcome the thermal energies of the ions and traps them. However for neutral atoms, magnetic dipole or induced electric dipole are too shallow to trap atoms directly from the thermal vapour. But the pre-cooled atoms from a MOT can be loaded into a very steep dipole trap to trap a single atom, at specific loading rates [94, 100].

The first observation of a single Cesium atom in a MOT was reported by Z. Hu et.al. [101] in 1994. In 1996 Haubrich et al. demonstrated the trapping of individual neutral Cesium atoms in a MOT with a very high magnetic field gradient, and also loaded the single atom from the MOT to a magnetic trap for tens of seconds [102]. Later the same group showed a controlled quantum system of individual neutral atom by deterministically loading a single atom from the MOT to the dipole trap [100] and also performed sub-micrometer position control of the single atom trapped this way [100, 103]. The collisional blockade based subpoissonian loading of single atom in a dipole trap was demonstrated in the group of Philippe Grangier [3, 94].

Recent experiments on individual neutral atoms, trapped in a dipole trap, have shown very impressive advancement in terms of their application in quantum computation as logic gates [104–106] as well as in quantum walk implementation [107]. Thanks to the high resolution imaging systems based on a high numerical aperture lens, which can trap and detect the internal states of the atom at its focal plane [108–112].

4.2 Single atom dipole trap based on collisional blockade

Trapping single neutral atoms from an ultra-cold atom reservoir has been demonstrated and exploited by several groups [94, 100, 105, 113]. The interest in this chapter is single atom dipole traps based on the collisional blockade mechanism [3]. Collisional blockade, which locks the average atom number to 0.5 in a microscopic dipole trap at specific loading rates in the presence

of MOT light beams [3, 114], arises due to very high two body loss rates in the microscopic dipole trap. The loading rate of the dipole trap is given by Eq. 3.64. Schlosser et. al. demonstrated three different regimes for the dipole trap loadings [3]. 1) Weak Loading:- for small loading rates, average number is $< N > \sim R/\gamma$ and collisional terms within trap are negligible while in 2) Strong

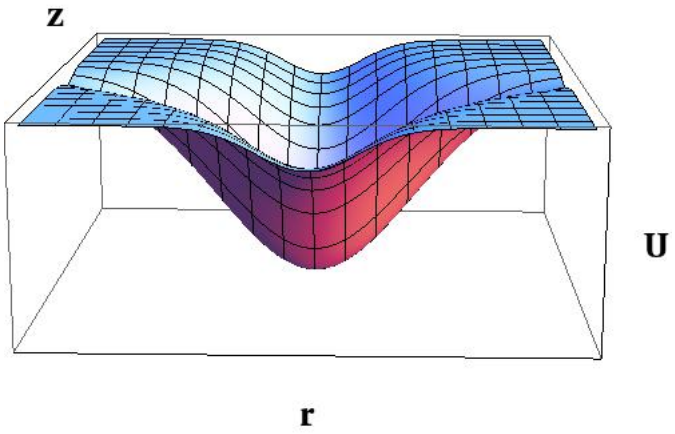

Figure 4.1: Potential generated by a focused red detuned gaussian laser beam. This negative potential due to the dipole trap beam, traps the atom with temperature less than the potential depth.

loading regime that becomes dominant and the average number of atoms are $< N > \sim \sqrt{R/\beta'}$ and 3) intermediate regimes, where collisional blockade can be observed for $\gamma \ll \beta'$. In the intermediate regime two atoms collision loss rate is very high i.e. as soon as the two atoms enter the trap, collisional loss kicks out both the atoms from the trap. Therefore either there can be one atom or no atom inside the trap.

These microscopic dipole traps are created by focussing a Gaussian laser beam to a diffraction limited spot using high numerical aperture (NA) lens. Therefore the single atom dipole trap requires focussing of the trapping beam on the cold atom reservoir i.e. MOT using High NA lens. Initial single atom dipole trap based on collisional blockade, used the diffraction limited high NA lens which were specially designed to give the diffraction limited performance without significant aberrations in the beam at the focus. Sortais et. al. [108] showed the complete characterization of commercially available high NA lens (NA=0.5) with a focal length of 8 mm to trap and detect the single trapped atom. It has become a very robust technique to trap and manipulate individual atoms in a tightly focused dipole trap. In our experiment the scheme towards the single atom

dipole trap is similar to that given in the references [108, 109]. An aspheric lens from Thorlabs C240TME-B (NA=0.5, f=8mm) has been used, to tightly focus the dipole beam and collect the fluorescence from the trapped Rubidium atoms.

Consider a Gaussian laser beam of power P, focused to a minimum waist w_0, with the spatial intensity distribution as,

$$I(z,r) = \frac{2P}{\pi w^2(z)} e^{-2r^2/w^2(z)}, \tag{4.1}$$

where

$$w(z) = w_0\sqrt{1+\left(\frac{z}{z_0}\right)^2} \quad \text{and} \quad z_0 = \frac{\pi w_0^2}{\lambda}, \tag{4.2}$$

$w(z)$ is the beam radius with beam waist w_0 and z_0 is the Rayleigh range. The parameters we use for dipole trap are the following

$$\lambda = 852\ nm \tag{4.3}$$

$$w_0 = 1\ \mu m \tag{4.4}$$

$$z_0 = 3.6\ \mu m \tag{4.5}$$

$$P = 10mW \tag{4.6}$$

$$\tag{4.7}$$

The trap depth and the scattering rate for ^{87}Rb for above parameters can be calculated from Eq. 3.25 and Eq. 3.26,

$$U_0 = -3mK.k_b \tag{4.8}$$

$$R_s = 87s^{-1} \tag{4.9}$$

Assuming harmonic oscillation of the atom, the radial and transverse oscillation frequencies of the atom at the center of the dipole trap can be given by,

$$\Omega_z = 2\pi\sqrt{\frac{2U_0}{m\lambda^2}} \tag{4.10}$$

$$\Omega_r = \sqrt{\frac{4U_0}{mw_0^2}}. \tag{4.11}$$

For the above mentioned parameters, $\Omega_z/2\pi = 33$ kHz and $\Omega_r/2\pi = 171$ kHz.

It is clear from the above discussion that precooled atoms with average thermal kinetic energy less than the dipole trap depth can be trapped in a dipole trap. The single atom trapping can be achieved in a microscopic dipole trap based on a collisional blockade mechanism. The requirement for this is a tightly focussed far-off red detuned laser beam. This is achieved by placing a high NA lens very near to the trap. This helps in following two ways:-

1) As discussed in section 3.6 of chapter 3, when a far-off red detuned beam (dipole trapping beam) is tightly focussed (waist $\leq$ 4 micron) at the centre of the cold atom reservoir (MOT), one can trap a single atom at specific loading rates. The collisional blockade mechanism [3], in the presence of the dipole trap, locks the atom number to one.

2) One of the conventional technique of florescence imaging used for cold atoms detections, requires collection of the photons emitted from the sample on a sensitive photodiode. For a single atom, this florescence signal is very small and requires collection of emitted photons within maximum solid angle. Placing the high numerical aperture lenses near the trap, maximizes the solid angle over which the fluorescence is collected.

4.3 Single atom dipole trap setup

4.3.1 High Numerical Aperture Lens inside the Vacuum Chamber

The cold atom experiment built for single atom trapping in our lab, consists of a vapour loaded MOT of ^{87}Rb. Two high NA lens (Thorlabs C240TME-B), are placed inside the vacuum system, symmetrically on the two sides of the MOT. The working distance between the lens is $\sim$ 1.1 cm. MOT is formed between these two lenses as described in chapter 3. The lens collects the fluorescence from the atoms and couples this light to a Single Photon Counting Module (SPCM) from Perkin Elmer and to an EMCCD camera through an imaging system described below (Fig. 4.2).

The pair of lenses have a numerical aperture of 0.5 with an effective solid angle for fluorescence collection of 0.7 percent . These are diffraction limited lens for a range of wavelength from 630-900 nm.

The high NA lens inside the vacuum has a diffraction limited performance for a point source at the focus with a 0.25 mm thick glass plate inserted between the lens and the object. In the absence of the glass plate this needs a convergence of 0.2^0 for the beam falling on the aspheric lens. Additionally the focal points for 850 nm and 780 nm differ by ~ 31 μm due to the difference in the refractive index of the lens material at different wavelengths . To make the trapping beam focus coinciding with 780 nm in the absence of the thin glass window, requires an overall convergence of 0.4^0 for a beam waist of 4 mm on the aspheric lens. For this the distance between the output coupler lens and the fiber holder is adjusted to get the required convergence. Fine adjustment is done by a piezoelectric driven translation stage under the coupler lens mount.

4.3.2 Trapping laser setup

The laser used for the dipole trap is an External Cavity Diode laser (Toptica) at the wavelength of 852 nm. The maximum output of the laser without and with fiber coupling is 130 mW and 100 mW respectively. The fiber output is splitted in two parts. One part is fed to the a tapered amplifier Boosta and the other part is send for single atom trapping. This trapping beam is collimated by a 60 mm focal length lens of a fiber collimator (60FC-T-4-M-60 from Kirchhoff-Schafter). This collimation lens is fixed on a high precision xyz-translation stage and can be adjusted with respect to the fiber. To change the convergence of the output beam, the distance between the collimating lens and the fiber holder can be adjusted. The trapping beam then transmits through the dichroic plate, kept at 45^0 to the incident beam. This separates the 780 nm fluorescence signal coming from the trapped atom and the 852 nm trapping beam. The dichroic plate has a 99% transmission (98% reflection) and 89% reflection (90% transmission) for 780 nm (852 nm) at 45^0 incidence angle.

The output of the Boosta is used for many atom dipole trap. The two beams are combined on a polarising beam splitter (PBS) as shown in the Fig. 4.2.

4.3.3 Imaging System

Detection of a single atom in the trap requires a carefully designed imaging system. This is due to the following reasons:-

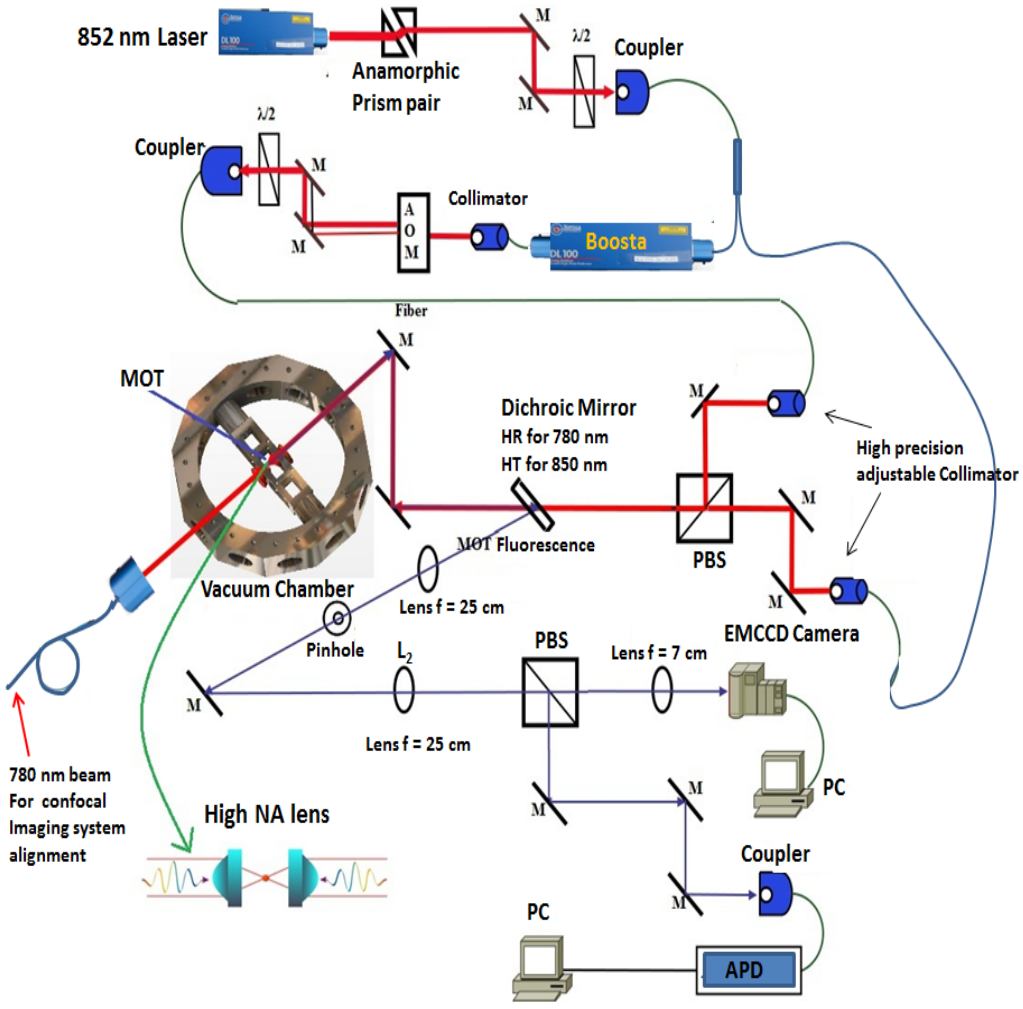

Figure 4.2: Figure shows the complete layout of the various optical elements used for the dipole trapping and detection of the rubidium atoms in the trap.

1) The fluorescence coming from the single ^{87}Rb atom is at subfemtowatt level. Further taking into account for all optical losses in various optical components, there are only few thousands of photons capable of reaching the detector. One has to minimize the losses as much as possible and at the same time have the maximum collection efficiency for the photons at 780 nm.

2) The careful alignment of all the optical components used in the imaging system is necessary to reduce the aberration at the image plane to improve signal to noise ratio. Additionally, to detect the single trapped ^{87}Rb atom in the presence of MOT requires a precisely aligned confocal

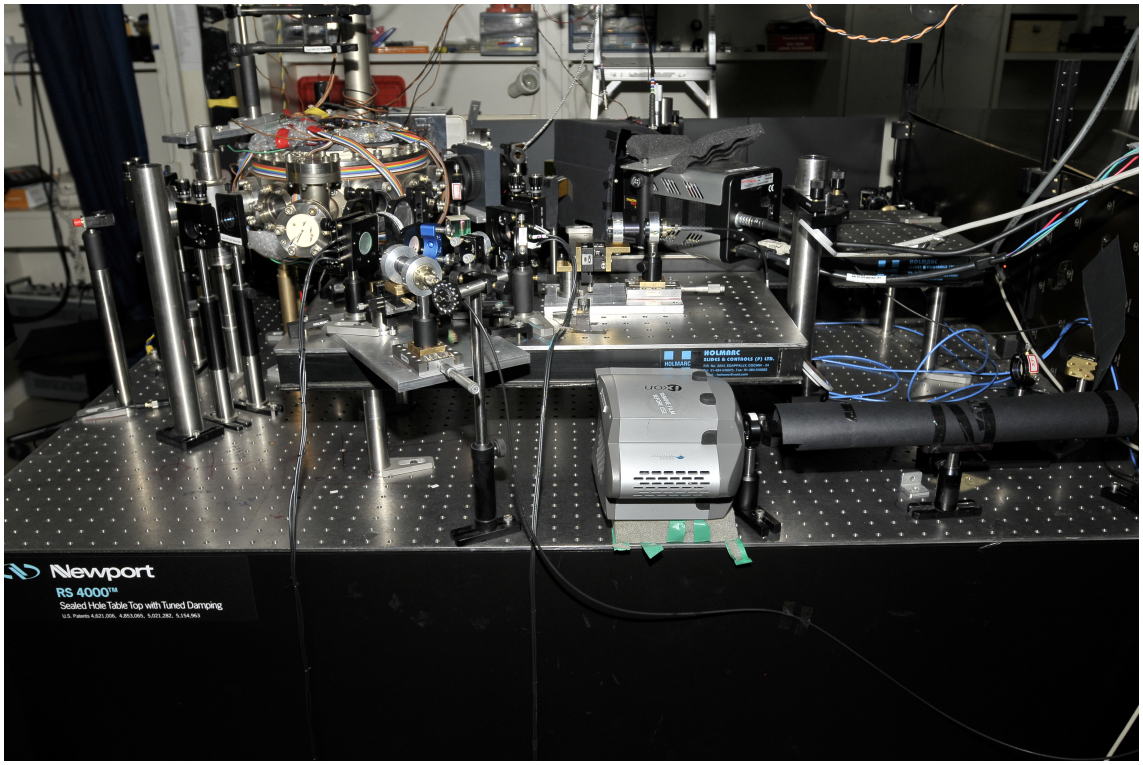

FIGURE 4.3: Complete optical layout around the vacuum chamber.

imaging system with respect to the trapped atom so that the background fluorescence coming from the MOT and the MOT light beams scattered from the lens mounts inside the chamber, can be maximally eliminated to get a good signal to noise ratio for atom detection.

Fig. 4.2 shows the schematic of the imaging system. The high NA lens inside the chamber works as an objective lens. The fluorescence collected by this lens is reflected by the dichroic plate and then focused on a 50 micrometer pinhole, using a doublet lens of 25 cm. The image of this pinhole is projected on the EMCCD camera using another doublet lens of 25 cm. A polarising beam splitter (PBS) in between, splits half of the signal for single photon detection on single photon counting module (SPCM). The fluorescence from the atoms is coupled to the SPCM using single mode polarization maintaining fiber. The fiber provides an easy way for spatial filtering of the light coming out of the trapped atom, from the stray light. The pinhole and the lens L_2 are placed on a translation stage so as to adjust the focus of the image on the camera. 780 nm band pass filters with 10 nm band pass is inserted in front of the single photon counting detector as

well as the camera.

4.3.4 Detector and Counting Module Integration

There are two detectors which we use for observing photons emitted from the trapped atoms, EMCCD (Andor-ixon) and Single photon counting module (SPCM). EMCCD specification is given in the Appendix:-B.

SPCM is an integrated single photon counting module from Perkin Elmer. This contains an APD (Avalanche Photo Diode) with quenched circuit and a well stabilized temperature controller. The APD has a quantum efficiency of 90% at 780 nm with an overall detection efficiency of 60%. Each detected photon event generates a standard TTL pulse at the output port. The dark count rates of the module is 50 counts per second (cps) as specified in the manual. Due to low dark count rates and high quantum efficiency, these devices have been used for various quantum optics experiments at single photon counting regime.

For monitoring the number of scattered photons from the single trapped atom as well as the MOT, SPCM is integrated with a M-series data acquisition (DAQ) card M-6259 from National Instruments. This card can count the TTL pulses resulting from the photon events in the detector (SPCM), in user specified time bins (minimum 10 microseconds). To see the presence or absence of a single atom in the trap, we operate the counter in the DAQ card at 10 ms time bin. The number of counts in the specified time bin is continuously displayed on the computer screen so as to control the sequence and optimize the experimental parameters. All the voltage sequences to control and automate the experiment is acquired and sent using Labview based programs.

To find out the spatial and the temporal correlation of photons emitted from the single atom or the MOT, we use two SPCMs in a Hanbury-Brown-Twiss kind of set up (Section 4.4) and the time series of photon counts is recorded with FPGA based coincidence counting unit which is described later in this chapter.

4.3.5 Alignment Procedure

The single atom dipole trapping beam from the diode laser is guided through a single mode polarization maintaining fiber and collimated using a high precision adjustable collimator (60

mm triplet lens) as shown in the Fig. 4.2. Both the fiber tip holder and the collimating lens of the collimator are mounted on separate and stable stand-alone mounts. The output fiber (lens) mount has x-, y- and z-translation.

Firstly the beam was perfectly aligned at the optical axis of the collimation lens. This is ensured by minimizing any lateral shift in the focal point position with the change in the distance between the fiber tip and the collimation. After the collimator the beam is aligned very accurately along the optical axis of the aspheric lens. The total distance between the collimation lens and the high NA (aspheric) lens inside the chamber is between 35 to 40 cm. A laser beam at 780 nm counter-propagates exactly to the trapping beam and used for the alignment of the imaging system.

After fixing all alignments very accurately, the convergence of the trapping beam (852 nm) is adjusted so as to have a convergence such that the trapping beam focus matches with the focal point of 780 nm beam, and also to overcome the shift in the focal plane due to the absence of the glass plate along with which the lens is supposed to be diffraction limited at the focus [108]. The trapping beam after passing through the second high NA lens is coupled to another fiber which has the same specification as for the fiber used to guide the trapping beam from the laser using another similar collimation lens. A beam at 780 nm is sent in the opposite direction to align the imaging system as well as the SPCM for fluorescence collection from the trapped atom. Detection efficiency of the overall imaging system is also calibrated using this beam. The various losses introduced by the different optical elements in the florescence signal after a 7.6 % collection of the signal from the solid angle subtended by the high NA lens are listed below.

4.3.6 Detection Efficiency Calibration

The previous table gives a list of losses due to different optical components in the path of the fluorescence light before it reaches SPCM and EMCCD camera. From this one can approximately estimate the number of counts expected from the SPCM in the presence of single trapped atom. The scattering rate of the atom from the MOT beam is approximately 1×10^6 per second and the overall efficiency of our detection system is around 0.7 %. The number of expected counts in the presence of the single trapped atom is around 700 counts/ 100 ms.

Table 4.1: Loss data budget due to different optical elements

Optical Element	Percentage loss
High NA lens	4 %
Viewport	5 %
Gold coated mirrors	7 %
Dielectric mirrors	4%
PBS	50 %
Pinhole	50 %
Band pass filter	40 %
Fiber Coupling	40 %
Detector	40 %

4.3.7 Towards Single Atom Trap

First the MOT is loaded from the thermal vapour of ^{87}Rb. The getter current is kept just above the threshold so that the background pressure does not rise significantly. The magnetic field gradient is kept low, around 5-10 Gauss/cm. The MOT is loaded in the presence of the dipole beam, the fluorescence from the trapping region is collected and number of photons per 100 ms time bin are continuously displayed on the computer screen. The background count, which includes the counts due to the scattered light at the lens mount, dark counts of the SPCM, and the photon counts due to MOT, are 500 cps. In the presence of a single trapped atom, the discrete jumps upto 7000 cps are expected when a single atom is loaded in the dipole trap.

Till the time of writing this thesis the single atom dipole trap setup has been completed. Few attempts which could be made to see the single atom signal in the presence of MOT beams, could not be unambiguously observed. Scattering from lens mount in the presence of MOT beams is one of the obstacle. The triggered measurement of the single trapped atom (in the dipole trap), using separate probe beam, is in progress.

Photon correlation measurement on the fluorescence light collected from the MOT is presented in the next section. Fig. 4.4 shows the MOT loading and decay characteristic, observed by

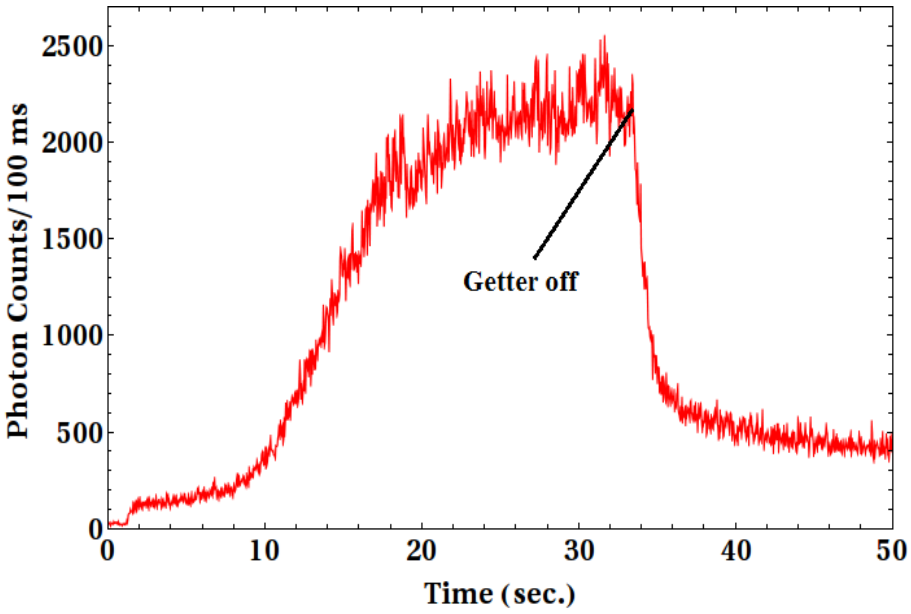

FIGURE 4.4: This figure shows the loading and decay of the MOT observed through high NA lens on single photon counting module. Getter current and field gradient is kept much higher in this case compared to the case of single atom operation regime.

counting number of photons in the SPCM for every 30 ms.

4.4 Coincidence Detection and Photon Correlation Measurement

Introduction:-

Fast and accurate coincidence detection of two or more input electrical signals within precise time window, has widespread applications in different branches of experimental physics. The coincidence counting schemes are routinely exploited in the study of quantum physics phenomenon dealing with the most fascinating and counter-intuitive properties of non-locality and entanglement of quantum particles. In these experiments two or more particles created from the same source following some conservation law and thus inexorably related to each other are used to trigger the quantum measurement. The other most important application of coincidence counting is in finding correlation between two detector signals in a Hanbury-Brown-Twiss (HBT) kind of

setup. This allows the study of a whole range of phenomenon, like bunching/anti-bunching properties of particles and photons, precision spectroscopy, life time measurement of atomic states, single molecule fluorescence spectroscopy etc. The basic principle of an HBT setup involves coincidence detection between the output pulses of two detectors, which are located at two different space time points. By varying the time delay, τ between the two detectors, one constructs the second order correlation function $g^2(\tau)$. This is an important parameter for specifying the photon/particle statistics in various experiments involving light matter interactions. The light-matter interaction at the microscopic level can be studied by the correlation properties of the scattered photons.

In this section a design and characterization of FPGA based correlation detection module and its application for $g^2(\tau)$ measurement using a HBT experiment is presented. The $g^2(\tau) = 1$, for all time delays τ, is obtained for a continuous laser beam while $g^2(0) = 2$ is obtained for light coming from the MOT, as expected from a thermal source. The interest in the photon correlation measurements is to study the various parameters of the laser cooled atoms and to detect the non-classical single photon states generated by using these systems.

The correlator which is built around a Virtex-5 field programmable gate array (FPGA) unit is a compact, multichannel recording module, which records the time-of-arrival of photons from two Avalanche Photo Diodes (APDs), and carries out coincidence-counting, offline. The module, accepts pulses from APDs in transistor-transistor logic (TTL) format, and time-tags them with a timing resolution of 5 ns. To optimize the overall data rate from the module, the FPGA implements an efficient time tagging scheme, wherein, tagging is carried out only when an output pulse from any or both APDs is registered. The time-tagged data is transferred to a PC through a standard Gigabit Ethernet interface, without any dead-time in data acquisition. Analysis tools, for a Linux platform, have been developed to measure the multi-fold coincidence, with the coincidence time-window ranging from a minimum of 5 ns to integral multiples of 5 ns.

4.4.1 Photon Statistics and Correlation Measurement

Photon statistics and the photon correlation functions [4] are the crucial parameters to characterize the light sources. The photon correlation function which can be described in terms of the

intensity-intensity correlation $(g^2(\tau))$ in a HBT experiment can also provide the information about the photon number distribution for a weak light source. More importantly the non-classical states of the light are characterized by $g^2(0) \leq 1$. $g^2(\tau)$, was first used by Hanbury Brown and Twiss in 1950 [29]) for classical states of light coming from a thermal light source. In that experiment the detectors and the integrated electronics were used in an analog mode and the time resolution was insufficient to observe the actual expected value of $g^2(\tau)$ at $\tau = 0$ but a smeared-out version of the actual curve was obtained. $g^2(\tau)$ function has also been used to observe Single-atom dynamics in a trap by photon correlations measurements [115].

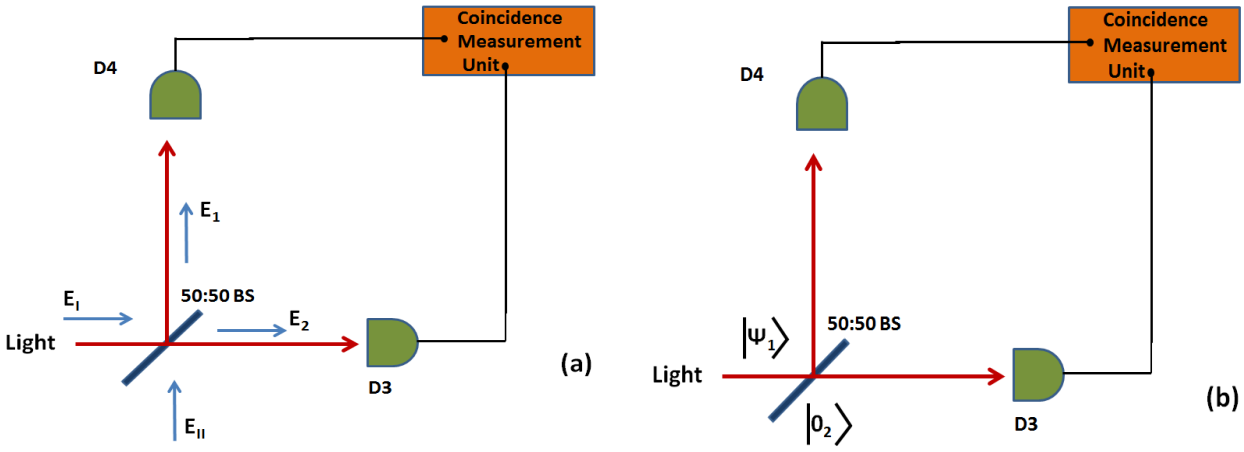

FIGURE 4.5: Fig. (a) shows an HBT experiment to measure the intensity cross correlation between the two input light fields (E_I and E_{II}) incident on a 50:50 beam splitter (BS). If one of the input port of the BS is vacuum (Fig. (b), it can measure $g^2(\tau)$ function for input light field $|\psi_1\rangle$ at other port.

In quantum detection theory developed by Glauber [4], $g^2(\tau)$ is the property of the radiation field and the measured quantity in a HBT experiment is the normally ordered correlation function [116]

$$g^2(\tau) = \frac{\langle E^{(-)}(t)E^{(-)}(t+\tau)E^{(+)}(t+\tau)E^{(+)}(t)\rangle}{|\langle E^{(-)}(t)E^{(+)}(t)\rangle|^2} \tag{4.12}$$

where the quantity at the numerator can also be written as

$$\langle E^{(-)}(t)E^{(-)}(t+\tau)E^{(+)}(t+\tau)E^{(+)}(t)\rangle = \langle : I(t)\, I(t+\tau) : \rangle \propto \langle : n(t)\, n(t+\tau) : \rangle \tag{4.13}$$

Here $E^{(+)}$ and $E^{(-)}$ represents the positive and negative frequency part of the scattered electric field at the detector, and $\langle ... \rangle$ denotes statistical averaging. The Eq. 4.12 can be written in a

form more formally used in theoretical analysis by using the definition of photon number operator as follows

$$g^2(\tau) = \frac{\langle \hat{a_1^\dagger}(t)\hat{a_2^\dagger}(t+\tau)\hat{a_2}(t+\tau)\hat{a_1}(t)\rangle}{\langle \hat{a_1^\dagger}(t)\hat{a_1}(t)\rangle\langle \hat{a_2^\dagger}(t+\tau)\hat{a_2}(t+\tau)\rangle} \tag{4.14}$$

where $n(t) = \hat{a}^\dagger(t)\hat{a}(t)$. For zero time delay between the detectors, the Eq. 4.14 simplifies to the following form

$$g^2(0) = \frac{\langle \hat{a_1^\dagger}\hat{a_2^\dagger}\hat{a_2}\hat{a_1}\rangle}{\langle \hat{a_1^\dagger}\hat{a_1}\rangle\langle \hat{a_2^\dagger}\hat{a_2}\rangle} \tag{4.15}$$

The value of $g^2(0)$ distinguishes between a classical or quantum state of radiation. One can learn whether a light source is bunched or anti-bunched.

Now considering the HBT experiment shown in the Fig 4.5(a), the $g^2(0)$ for an arbitrary input state can be calculated by relating the creation and annihilation operator at the output port of the beam splitter to the input fields. The input-output fields , (E_I, E_{II}) and (E_1, E_2) respectively has the following relationship at the ports of the beam splitter.

$$E_1 = (E_I - E_{II})/\sqrt{2} \tag{4.16}$$

$$E_2 = (E_I + E_{II})/\sqrt{2} \tag{4.17}$$

The relationships between the creation and annihilation operators at the input-output port follows from this

$$\hat{a}_1 = (\hat{a}_I - \hat{a}_{II})/\sqrt{2} \tag{4.18}$$

$$\hat{a}_2 = (\hat{a}_I + \hat{a}_{II})/\sqrt{2} \tag{4.19}$$

and similar for creation operators by taking Hermitian conjugate of the equation.

As shown in the Fig 4.5(b), the light $|\psi_1\rangle$ enters at port 1 while other port 2 has vacuum state $|0_2\rangle$. The input state can therefore be written as follows

$$|\Psi\rangle = |\psi_1, 0_2\rangle \tag{4.20}$$

Now using the Eq. 4.18 and Eq. 4.15, the final expression for $g^2(0)$ is

$$g^2(0) = \frac{\hat{n}(\hat{n}-1)}{\hat{n}^2}, \tag{4.21}$$

where $\langle ....\rangle$ are the expectation values now evaluated at the input state port 1.

For the input photon number state $|n\rangle$,

$$g^2(0) = \frac{n(n-1)}{n^2}. \tag{4.22}$$

A highly non-classical value of $g^2(0) = 0$ is expected for a single photon source which emits photon number state with $n = 1$. The source is anti-bunched in this case which means that the probability of measuring a second photon after one photon is already detected is very small. Such sources are single quantum emitters and often called non-classical because in classical electromagnetic theory the auto-correlation of the intensity must attain its maximum value at $\tau = 0$.

For a classical "random Gaussian field" where the emitted light field is a resultant sum of many independent radiators, the intensity correlation function $g^2(\tau)$ is related to the field correlation function by [116]

$$g^2(\tau) = 1 + |g^1(\tau)|^2, \tag{4.23}$$

where the field correlation function or the first order coherence function $g^1(\tau)$ is given by

$$g^1(\tau) = \frac{\langle E^{(-)}(t)E^{(+)}(t+\tau)\rangle}{\langle |E(t)|^2\rangle} \tag{4.24}$$

$g^1(\tau)$ is related to the power spectrum of the field by Wiener-Khintchine theorem [28]. Therefore for a field with a Lorentzian spectrum

$$g^2(\tau) = 1 + e^{-\gamma\tau}, \tag{4.25}$$

and for a field with Gaussian spectrum

$$g^2(\tau) = 1 + e^{-\gamma^2\tau^2}, \tag{4.26}$$

where γ is the spectral linewidth which is inverse of the coherence time, τ_c of the source. It can be seen here that for $\tau \gg \tau_c$, $g^2(\tau) \to 1$. The increased value of the $g^2(\tau)$ for $\tau < \tau_c$ for chaotic light compared to the coherent light is due to increased intensity fluctuations in the chaotic light field. In a HBT experiment with photon counting detectors it tells that there is a high probability to detect a photon in the second detector soon after the detection of the photon at the first

detector. Due to this property of photons to arrive in bunches, a chaotic light source is sometime also called as bunched light source. Light coming from a thermal light source like incandescent lamp, fluorescence from the Magneto-Optical-Trap or Optical molasses, light from the sun etc. are few examples of chaotic or thermal light sources.

In the photon correlation measurement, the modified version of the HBT experiment often uses single photon sensitive avalanche photodiodes for the photon detection. Which generates an electrical pulse whenever a photon is detected. After detecting each photon, there is a minimum time required to stop the avalanche process and prepare for the next detection event. During this time the detector experiences a "dead" time. The detector used in this work are commercially available single photon counting modules SPCM-AQR-15 from Perkin Elmer. These have a dead time of 50 ns and a dark count rate of around 50 per second. The output of the detector are standard TTL pulses with a rise time of $\approx 2ns$ and width of $\approx 16ns$. In the standard HBT experiment as shown in the Fig. 1.3, the photons from a weak source incident on a 50:50 beam splitter and after splitting impinges on these two detectors. The output pulses are analyzed for photon coincidence with a lowest possible coincidence time window of 5 ns from the recorded time series of the two detectors. The HBT experiment circumvents the dead time of APDs. In the setup $g^2(\tau)$ measurement relies on the coincidence detection between the two detectors at various time delay.

4.4.2 Operating principle of the coincidence detection unit

The coincidence detection unit which is developed and used here is based on FPGA electronics and carries out coincidence detection between output pulses from the avalanche photodiodes (APD) based single photon counting modules (SPCMs). The unit works like a multichannel recording module, which records the time-of-arrival of photons from upto four detectors. Apart from recording the number of photons that arrived from each of the four SPCMs and counting the multi-fold coincidences, one of the primary requirements of this unit was to continuously record the time-of-arrival of photons from each of the four SPCMs. A straightforward way of achieving this would have been to record, at every sampling interval of 5 ns, an n-bit pattern consisting of any of the 16 possible states from the four possible detectors, along with a k-bit (k

n) time-tag. At such a high sampling rate, even for n = 8, it would result in a huge data rate of 200 megabytes per second (MBps) if there is no preprocessing in the FPGA hardware. While recording data at such a high data rate is one challenging aspect, other practical issues arising from this scheme are data archival and processing-time, especially, considering that the useful

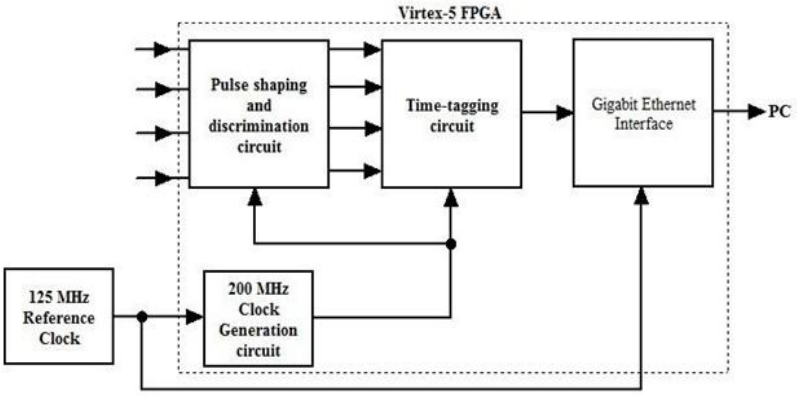

FIGURE 4.6: Block schematic of Coincidence unit

data could be less than 1 percent of the acquired data. Instead of recording an n-bit data pattern at every sampling instant, if data is recorded only when there is an event in any SPCM, it would result in a substantial reduction of data rate. A schematic diagram illustrating the basic operating principle of this unit firmware residing inside the Virtex-5 (XCV5LX50T) FPGA is shown Fig. 4.6.

The pulse-shaping and discrimination logic section and the time-tagging circuit operate on a 200 MHz master clock signal. The master clock is generated inside the FPGA, using the 125 MHz reference signal coming from an on-board crystal oscillator. The coincidence detection unit accepts signals in TTL standard from four SPCMs, and translates them to low voltage differential signal (LVDS) format. The operating voltages of modern FPGAs prevent them from directly accepting signals in TTL standard. A glitch, generated in the unit's hardware, being common to all four inputs would result in a false coincidence from all four detectors. In order to reduce such false coincidences being registered, the SPCM signals are first passed through a pulse-shaping and discrimination logic section. Unlike in a typical coincidence detection circuit based on logic gate and multiplexers, in our system, pulse widths do not matter because the time-tagging circuit is edge-sensitive. The time-tagging circuit is designed around a 5-bit counter, running on the

200 MHz master clock, and a 16-bit register. The 5-bit counter wraps around once every 160 ns.

B_{15}	b_{14}	b_{13}	b_{12}	b_{11}	b_{10}	b_9	b_8	b_7	b_6	b_5	b_4	b_3	b_2	b_1	b_0
OvF	X	X	Reserved				D4	D3	D2	D1	C4	C3	C2	C1	C1

Figure 4.7: 16-bit register in the time-tagging circuit

The 16-bit register is used to register events in any/all of the four SPCMs, and each wraparound of the 5-bit counter. Fig. 4.7 shows the arrangement of the 16-bit register, in which, the SPCM events are registered in bits b5 to b8 and wraparound event is stored in the most significant bit, b15, and 5-bit counter value is stored in the five least significant bits. The overflow bit, OvF, stays high for one master clock period, every time a wraparound event occurs. Between two OvF pulses, if there are no SPCM events to be registered, data rate from the coincidence unit would be limited to 12.5 MBps. The time-tagged data is transferred out of FPGA using the standard Gigabit Ethernet (GigE) interface, whose theoretical data throughput rate is 125 Mbps. The Virtex-5 FPGA used in the coincidence detection unit contains embedded Tri-mode (10/100/1000 Mbps) Ethernet Media Access Controller (TEMAC) blocks, and GTP transceivers capable of serial transmission up to 3.75 Gbps. The TEMAC is capable of supporting gigabit Ethernet transmission over fiber, by connecting to a GTP transceiver. Instead of an optical SFP (small form-factor pluggable) module interfacing with the GTP transceiver, the coincdence unit uses a GigE SFP copper transceiver module to interface with a PC. The Ethernet firmware used in this unit has features to include some maker patterns and a 32-bit packet counter along with data that is sent as a UDP (user datagram protocol) packet. A marker pattern, for example, helps the data processing software in skipping certain packet header information and identifying the start of actual data. The 32-bit packet counter value can be used to identify missing UDP packets, if any.

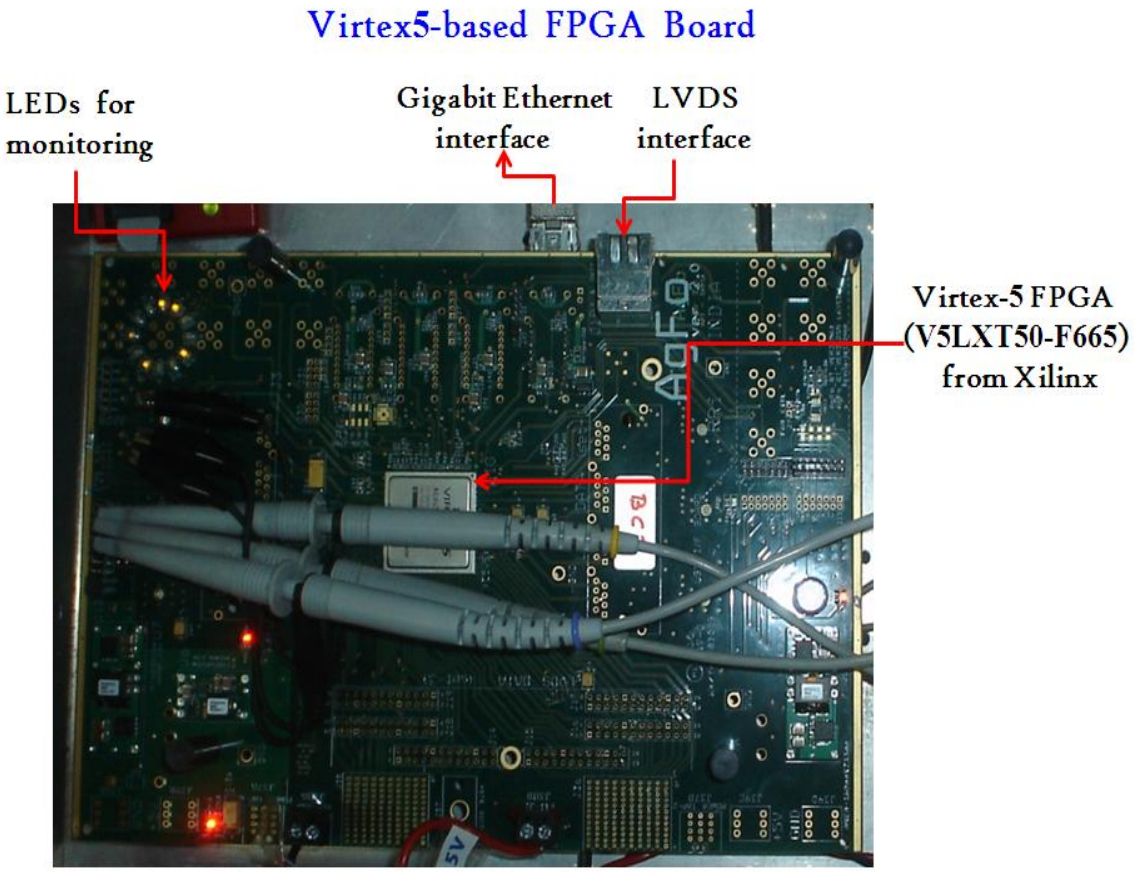

FIGURE 4.8: Vertex-5 based FPGA board used for Coincidence unit

4.4.3 $g^2(\tau)$ measurements

In a HBT experiment using two photon counters, the $g^2(\tau)$ is evaluated in terms of number of coincidence counts at both detectors, individual counts on each detector, averaging time T and the coincidence time window t_c. For photon counting detection the $g^2(\tau)$ can be written in terms of probabilities of coincidence counts and counts of individual detectors as follows

$$g^2(\tau) = P_{12}/P_1P_2, \tag{4.27}$$

where P_{12} is probability of coincidence counts at both detectors and P_1 and P_2 are the probabilities at individual detectors. In the experiment the total coincidence counts N_{12} and individual counts N_1, N_2 are recorded for a total time T using a coincidence time window of Δt. The probabilities

then can be written as

$$P_1 = (\frac{N_1}{T})\Delta t \tag{4.28}$$

$$P_2 = (\frac{N_2}{T})\Delta t \tag{4.29}$$

$$P_{12} = (\frac{N_{12}}{T})\Delta t \tag{4.30}$$

Finally the $g^2(\tau)$ can be written in terms of experimentally observed parameters as follows

$$g^2(\tau) = \frac{N_{12}}{N_1 N_2}(\frac{T}{\Delta t}) \tag{4.31}$$

The time delay between the detectors, τ, is introduced offline by shifting the one of the recorded time series of the two detectors.

For a coherent laser beam

First as a test bench for the coincidence detection module, a highly attenuated light from a narrow linewidth continuous diode laser was analysed for $g^2(\tau)$ for various coincidence time windows and

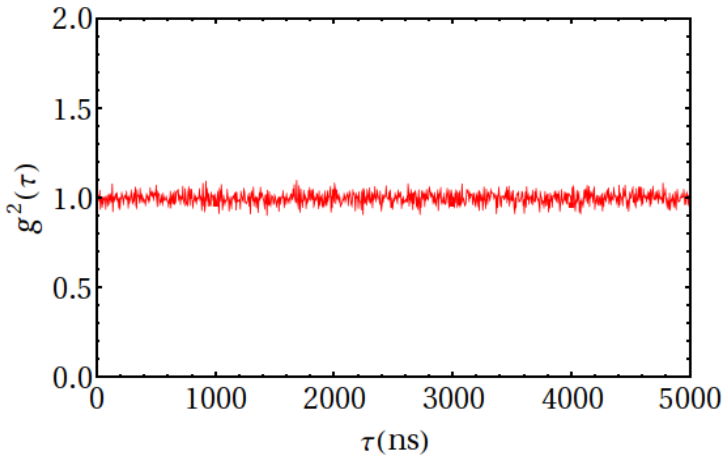

Figure 4.9: Figure shows the measured plot of second order correlation function $g^2(\tau)$ for attenuated laser beam.

delays ranging from tens of nanosecond to hundreds of millisecond and found to produce $g^2(\tau) = 1$ for all time delays as expected. The Fig. 4.9 shows the result for $g^2(\tau)$ measurement for laser. As one goes for lower coincidence time windows the event of photon occurrence in a time bin

reduces with increased fluctuation due to poissonian process of the detection itself and it requires longer observation time. For a minimum coincidence time window of 5 ns, it was observed that 8 hours of data is required to average out the random statistical fluctuations .

For chaotic light scattered from laser cooled atoms

The light coming from a thermal light source shows a bunching effect with second order correlation value 2 at zero time delay between the detectors. As the delay between the detectors, τ is increased, $g^{(2)}(\tau) \rightarrow 1$ for long time delays. Using our coincidence unit we have observed the bunching behaviour of the light emitted from laser cooled atoms in a magneto-optical-trap (Fig. 4.10). For such a light source the coherence time is of the order of few tens of nanoseconds. Therefore to get $g^{(2)}(0) = 2$, it is require to have a coincidence detection unit with coincidence detection window in few nanoseconds and with least dead time and data loss effects. It is clear from the results that the this device is very efficient for coincidence detection in nanoseconds time scales (multiples of 5 ns). Fig. 4.10 shows rapid damped oscillation around $\tau = 0$. This regime

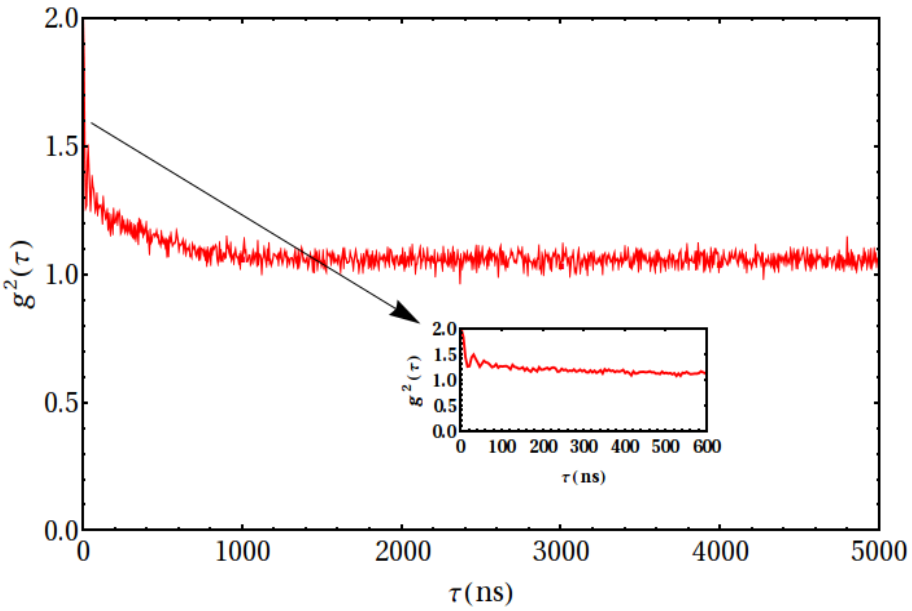

FIGURE 4.10: Figure shows the measured plot of second order correlation function $g^2(\tau)$ for the MOT fluorescence.

can be further explored to study the effect between the coherent Rayleigh scattering component

and the incoherent resonance fluorescence triplet from the cold atom sample.

Comparison of $g^2(\tau)$ for tailored light sources

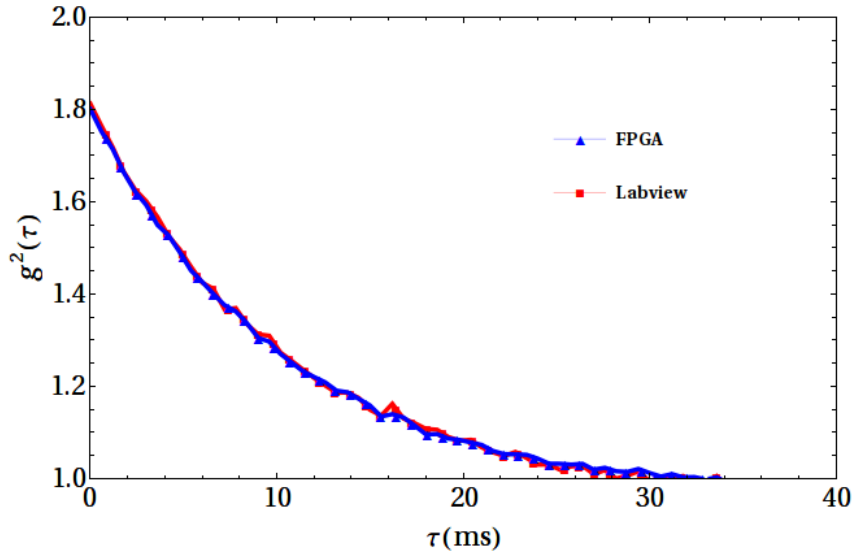

Figure 4.11: Figure shows a comparision of the second order correlation function $g^2(\tau)$ using Labview vs. FPGA.

In this part the unit is tested for longer coincidence time window in the time scales of milliseconds. We have used tailored light sources with known coherence properties (Chapter 1) and compared experimentally obtained $g^2(\tau)$ function values using Labview based counters against our coincidence detection unit. The results are shown in the Fig. 4.11. It shows that the unit works efficiently for millisecond time scales as well.

4.5 Conclusion

In this chapter the complete optical layout of the dipole trap setup and the imaging system with its efficiency and expected signal from the single atom trap is presented. A photon correlation measurement experiment to study second order correlation of different kind of light sources, is also presented. A full description of an FPGA based correlator is given which is built for coincidence

detection between two or more detectors. Finally measured $g^2(\tau)$ function for an attenuated coherent laser beam and for the fluorescence light coming from the MOT are given.

Setting up this kind of experiments aim towards study of the dynamics and various parameters of the trapped atom using photon correlation measurements. The non-classical states with tunable properties, as described in Chapter 1, may be generated and their interaction with a single trapped atom can be studied using high numerical aperture lens which can create a strong coupling between the photon and the atom.

5

Chapter 5

5.1 Conclusion and Future Prospects

A single atom that is cooled and trapped is an important controlled quantum system that enables a variety of applications and studies like, single photon generation, quantum information processing, study of controlled interaction between the atoms, study of atom-photon interaction in free space as well as in controlled environment. At the heart of all these is the atom-photon interaction at single atom and single photon level, and is the fundamental process behind the light-matter interaction.

This thesis sets a basic platform towards studying interaction between non-classical states of light and a single atom. The first part of the thesis that essentially deals with manipulation of coherent light motivates towards generation of tailored non-classical states of light using photon addition techniques on tailored classical states. These non-classical states in themselves, have

application in quantum information processing. At the same time a study between such photon states and a single trapped atom presents a lot of interesting problems.
Usually non-classical light generation suffers from large linewidths due to underlying non-linearities; and hence are expected to have limited direct application in atom-photon interactions. This limitation may be overcome by combining the technique with a cavity setup.

In the second part of the thesis a cold atom experiment setup with a single atom trap and photon correlation measurement setup are developed. While the single atom trap setup is completed and attempt to look for the signal of the trapped single atom is made, an unambiguous measurement could not be obtained till the time of writing this thesis. One of the obstacle has been the light scattered from the lens mount. A new lens mount was designed and built during the course of setting up this experiment. This can be used to greatly suppress the scattering of the MOT beams.

The existing MOT which is in a retro-reflected configuration, can be changed to a MOT with six independent beams. This provides an easy way of shifting the MOT position.

5.2 Future Prospects

A well stabilized and well controllable single trapped atom will provide the following possible experimental explorations-
1) Single photon generation:-
The fluorescence coming out of a single trapped atom shows anti-bunching behaviour indicating non-classical behaviour of the emitted photons. A single atom system can be used as a triggered single photon source.
2) Atom-photon interaction:-
The interaction between non-classical states of light and the single atom is useful in applications related to quantum meteorology. There, the quantum projection noise during an atom-photon interaction by a coherent laser, can be reduced by using non-classical states of light instead of a coherent state.
3) Controlled interaction between neutral atoms:-
A very well engineered neutral atom trap has application in studying the controlled interaction

between the atoms. Using a high numerical aperture lens multiple traps can be obtained and manipulated by changing the trapping beam parameters and sending multiple trapping beams with small inclination to one another.

6

Appendix: A

Photon creation and annihilation operation on a coherent state

Coherent state in the number state basis is

$$|\alpha\rangle = \exp\left(-\frac{|\alpha|^2}{2}\right) \Sigma_{n=0}^{\infty} \frac{\alpha^n}{\sqrt{n!}} |n\rangle \tag{6.1}$$

As described in the section 1.2.4 of this thesis, the operation of the photon creation operator $\hat{a}^\dagger$ and the photon annihilation operator $\hat{a}$, on a coherent state can be evaluated as follows.

The action of the annihilation operator on the coherent state is

$$\hat{a}|\alpha\rangle = \exp\left(-\frac{|\alpha|^2}{2}\right) \Sigma_{n=1}^{\infty} \frac{\alpha^{n-1}}{\sqrt{n-1!}} |n-1\rangle = \alpha|\alpha\rangle \tag{6.2}$$

The action of the creation operator on the coherent state has an important property

$$\hat{a}^{\dagger}|\alpha\rangle \exp\left(\frac{|\alpha|^2}{2}\right) = \frac{\partial}{\partial\alpha}(|\alpha\rangle e^{|\alpha|^2/2}) \tag{6.3}$$

This can be proved as follows.

$$\hat{a}^{\dagger}|\alpha\rangle = \exp\left(-\frac{|\alpha|^2}{2}\right) \Sigma_{n=0}^{\infty} \frac{\alpha^n\sqrt{n+1}}{\sqrt{n!}}|n+1\rangle \tag{6.4}$$

which can be written as follows

$$\hat{a}^{\dagger}|\alpha\rangle \exp\left(\frac{|\alpha|^2}{2}\right) = \Sigma_{n=1}^{\infty} \frac{\alpha^{n-1}\sqrt{n}}{\sqrt{(n-1)!}}|n+1\rangle \tag{6.5}$$

Now evaluating the following partial differential w.r.t. α we get

$$\frac{\partial}{\partial\alpha}(|\alpha\rangle e^{|\alpha|^2/2}) = \Sigma_{n=1}^{\infty} \frac{\alpha^{n-1}\sqrt{n}}{\sqrt{(n-1)!}}|n+1\rangle \tag{6.6}$$

Hence it follows that

$$\hat{a}^{\dagger}|\alpha\rangle \exp\left(\frac{|\alpha|^2}{2}\right) = \frac{\partial}{\partial\alpha}(|\alpha\rangle e^{|\alpha|^2/2}) \tag{6.7}$$

7

Appendix: B

Detectors used in the experiment

As described in the section 3.8 of this thesis, we have used two EMCCD cameras and avalanche photodiode based photon counting modules for the detection of fluorescence from laser cooled and trapped rubidium atoms. A brief specification regarding these detectors is presented below.

PI-ACTON EMCCD Camera

We are using an EMCCD camera, PhotonMax:512B, from Princeton Instruments, where EMCCD stands for electron multiplication charge coupled device. This camera has an extended serial register behind each pixel of a low noise cooled CCD. Electrons from pixel to pixel are accelerated in the serial register and causes gain by emission of secondary electrons on a silicon chip by impact

ionization. The multiplication gain can be controlled by controlling the clock voltages for the serial registers.

This camera has a pixel size of 16 μm $\times$ 16 μm with a resolution of 512$\times$512. This camera is used for fluoresence imaging in the diagnosis of magneto-optical-trap.

Andor ixon EMCCD Camera

This is also an EMCCD camera which is used for single atom fluorescence imaging of Rubidium atom. This camera is from Andor company.

Pixel size of 32 μm $\times$ 32μm with a resolution of 512$\times$512.

Single photon counting module

In the Chapter 1 and Chapter 4 of this thesis we have used avalanche photo diode (APD) based single photon counting modules (SPCMs) for weak light detection.The SPCM-AQR from Perkin Elmer is a self-contained module which detects single photons of light over the wavelength range from 400 nm to 1060 nm. This device uses a silicon avalanche photodiode. Its quantum efficiency exceeds 90 percent and the overall detection efficiency exceeds 70 percent at 650 nm. The photodiode is both thermoelectrically cooled and temperature controlled, ensuring stabilized performance despite changes in the ambient temperature. The SPCM-AQR module can count to speeds exceeding 10 million counts per second (Mc/s) for the SPCM-AQR-15. There is a "dead time" of 50 ns between pulses and single photon arrival can be measured with an accuracy of 350 ps FWHM. The dark counts are 50 cps.

This information is taken from Perkin ELmer website.

8

Appendix: C

Properties of Rubidium

As described in the Chapter 3 of this thesis, we have laser cooled and trapped the Rubidium atoms which are alkali atoms. In general alkali atoms have relatively simpler energy level structure and their strong D-lines are accessible using tunable didoe lasers. The hyperfine structure of D-lines provides closed transition which is required for laser cooling.

Rubidium has two stable isotopes ^{85}Rb (72.2 %) and ^{87}Rb (27.8 %). Some of the important physical and chemical properties of Rubidium are listed below.

Electronic Structure

Ground state electronic configuration of the rubidium atom is $1s^2\,2s^2 2p^6\,3s^2 3p^6 3d^{10}\,4s^2 4p^6\,5s^1$ or equivalently [Kr]$5s^1$. In general for laser cooling of rubidium atoms, the relevant transition of the outer most single valence electron is 5 S $\rightarrow$ 5 P. Due to spin-orbit (LS) coupling the 5 P state splits into D-line doublet with transition wavelengths of 794 nm of D_1 line ($5S_{\frac{1}{2}} \rightarrow 5P_{\frac{1}{2}}$) and 780 nm of D_2 line ($5S_{\frac{1}{2}} \rightarrow 5P_{\frac{3}{2}}$). The electrons total magnetic moment including spin, interacts with the total nuclear magnetic moment to create additional hyperfine splitting.

Table 8.1: Rubidium Data Sheet

Element	^{85}Rb	^{87}Rb
Melting Point	39.31^0C	39.31^0C
Boiling Point	343 K	343 K
Isospin I	5/2	7/2
Relative abundance	72.17%	27.83%
Saturation Intensity I_s	1.64 mW/cm^2	1.64 mW/cm^2
Doppler Limit v_D	11.85 cm/s (143.41 μK)	11.81 cm/s (146 μK)
Recoil Limit v_r	0.602 cm/s (0.370 μK)	0.588 cm/s (0.36195 μK)
D_2 Transition	^{85}Rb	^{87}Rb
Wavelength λ	780.2 nm	780.037 nm
Decay time τ	26.63 ns	26.24 ns

9

Appendix: D

Switching Circuit for the MOT experiment

The fast magnetic field switching with least transient response is required for MOT diagnostics. We have used IGBT based switching circuit for MOT coils. IGBT based system includes driver circuitry for IGBT, snubber circuit for protection purposes, and freewheeling circuitry for back emf suppressions.

Structure and operation of IGBT module

The IGBT, Insulated Gate Bipolar Transistor, is a switching transistor that is controlled by voltage applied to the gate terminal. Device operation and structure are similar to those of an Insulated Gate Field Effect Transistor, more commonly known as a MOSFET. The principal difference

between the two device types is that the IGBT uses conductivity modulation to reduce on-state conduction losses.

The npn BJT is a three junction device that requires a continuous current flowing into the base region to supply enough charges to allow the junctions to conduct current. Because the MOSFET and the IGBT are voltage-controlled devices, they only require voltage on the gate to maintain conduction through the device. The IGBT has one junction more than the MOSFET, and this junction allows higher blocking voltage and conductivity modulation during conduction. This additional junction in the IGBT does limit switching frequency.

IGBT CM-200DU-12F:

Mitsubishi IGBT modules are designed to be rugged, low loss and easy to use. They give low on-state saturation voltages while maintaining the high switching speed needed for 20 KHz operation. Each module consists of two IGBTs in a half bridge configuration with each transistor having a reverse-connected super-fast recovery free wheel diode. Specifications: Ic 200A, Vces-600v, Dual IGBT module and 250v Trench Gate

M57962L IGBT driver:

This is a Hybrid Gate Driver from Mitsubishi designed to convert logic level control signals (0 to 5V) into optimal IGBT gate driver (-12v to +15v). Input signals are isolated from the IGBT drive using high speed optocouplers with 15,000 V/ms common mode noise immunity. Mitsubishi IGBT drivers are designed to provide the pulse currents necessary for high performance switching applications and to maintain sufficient off bias to guarantee ruggedness. They also provide short-circuit protection. Depending on the gate input, when the gate is at +15v, IGBT is switched on and current flows through the Magnetic coil and IGBT. When gate is at 12v, IGBT is switched off. Also a clamp diode which is a fast recovery diode is connected across the coil, to maintain current flow in the magnetic coils when IGBT is switched off.

Snubber Circuit:

It is required for the following purposes:-

(i)**Turn-off surge voltage:** Turn-off surge voltage is the transient voltage that occurs when the current through the IGBT is interrupted at turn-off. A voltage (VS) equal to Lb x di/dt appears across Lb (Bus Inductance) in opposition to increasing current in the bus. The polarity of this voltage is such that it adds to the DC bus voltage and appears across the IGBT as a surge voltage. In extreme cases, the surge voltage can exceed the IGBTs VCES rating and cause it to fail. In a real application the parasitic inductance (Ls) is distributed throughout the power circuit but the effect is the same.

(ii)**Free-Wheel Diode Recovery Surge:** A surge voltage similar to the turn-off surge can occur when the free-wheel diode recovers. The parasitic bus inductance (Lb) develops a surge voltage equal to Lb x di/dt in op-position to the decreasing current. In this case, the di/dt is related to the recovery characteristic of the free-wheel diode. Some fast recovery diodes can develop extremely high recovery di/dt when they are hard recovered by the rapid turn on of the lower IGBT. This condition referred to as snappy recovery, can cause very high transient voltages.

IGBT DriverM57962LTTL I/PTo IGBT GateFault

Snubber circuits are usually used to control turn-off and free-wheel diode recovery surge voltages. In some applications snubber circuits are used to reduce switching losses in the power device. In our setup we use a RCD snubber across IGBTs.

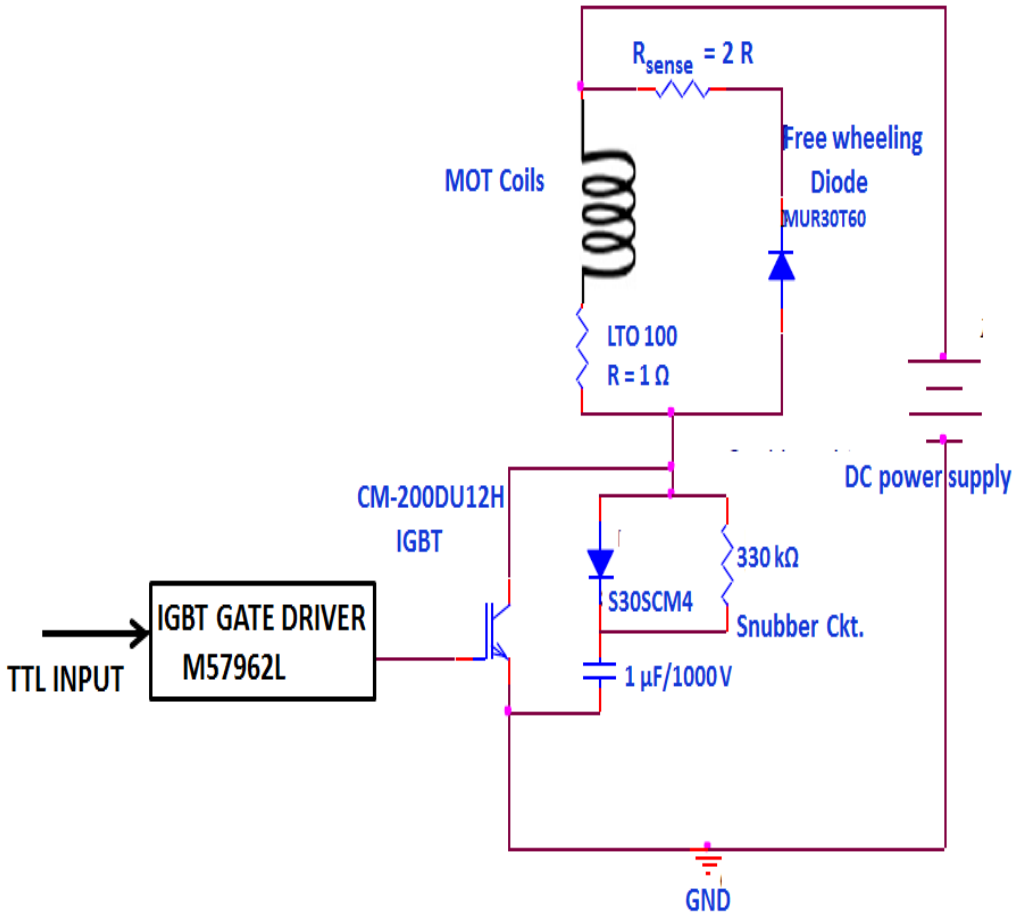

FIGURE 9.1: Figure shows the circuit diagram of the switching circuit which is used to on and off the MOT coils.

References

[1] B. Lounis and M. Orrit, Reports on Progress in Physics **68**, 1129 (2005).

[2] N. Satapathy *et al.*, EPL (Europhysics Letters) **97**, 50011 (2012).

[3] N. Schlosser, G. Reymond, and P. Grangier, Phys. Rev. Lett. **89**, 023005 (2002).

[4] R. J. Glauber, Phys. Rev. Lett. **10**, 84 (1963).

[5] E. C. G. Sudarshan, Phys. Rev. Lett. **10**, 277 (1963).

[6] E. Fermi, Rev. Mod. Phys. **4**, 87 (1932).

[7] R. J. Glauber, Phys. Rev. **131**, 2766 (1963).

[8] P. Kok *et al.*, Rev. Mod. Phys. **79**, 135 (2007).

[9] A. Valencia, G. Scarcelli, M. D'Angelo, and Y. Shih, Phys. Rev. Lett. **94**, 063601 (2005).

[10] D. Zhang, Y.-H. Zhai, L.-A. Wu, and X.-H. Chen, Opt. Lett. **30**, 2354 (2005).

[11] F. Ferri *et al.*, Phys. Rev. Lett. **94**, 183602 (2005).

[12] A. Gatti *et al.*, Journal of Modern Optics **53**, 739 (2006).

[13] A. Martin *et al.*, EPL (Europhysics Letters) **97**, 10003 (2012).

[14] A. Zavatta, V. Parigi, and M. Bellini, Phys. Rev. A **75**, 052106 (2007).

[15] V. Parigi, A. Zavatta, and M. Bellini, Journal of Physics B: Atomic, Molecular and Optical Physics **42**, 114005 (2009).

[16] T. Kiesel, W. Vogel, M. Bellini, and A. Zavatta, Phys. Rev. A **83**, 032116 (2011).

[17] C. Xie, G. Klimeck, and D. S. Elliott, Phys. Rev. A **41**, 6376 (1990).

[18] N. Satapathy, D. Pandey, S. Banerjee, and H. Ramachandran, Journal of the Optical Society of America A **30**, 910 (2013).

[19] D. Pandey, N. Satapathy, M. S. Meena, and H. Ramachandran, Phys. Rev. A **84**, 042322 (2011).

[20] W. Martienseen and E. Spiller, Am. J. Phy. **32**, 919 (1964).

[21] F. T. Arecchi, Phys. Rev. Lett. **15**, 912 (1965).

[22] G. S. Agarwal and K. Tara, Phys. Rev. A **43**, 492 (1991).

[23] A. Ourjoumtsev, R. Tualle-Brouri, J. Laurant, and P. Grangier, Science **312**, 1890 (2007).

[24] K. K. Sabapathy, J. S. Ivan, and R. Simon, Phys. Rev. Lett. **107**, 130501 (2011).

[25] F. Dell'Anno, S. De Siena, L. Albano, and F. Illuminati, Phys. Rev. A **76**, 022301 (2007).

[26] F. Dell'Anno, S. De Siena, L. Albano Farias, and F. Illuminati, The European Physical Journal Special Topics **160**, 115 (2008).

[27] W. Demtroder, *Laser Spectroscopy*, 3 ed. (Springer, New Delhi, 2004).

[28] L. Mandel and E. Wolf, *Optical Coherence and Quantum Optics* (Cambridge University Press, Oxford, 1995).

[29] R. H. Brown and R. Q. Twiss, Nature **177**, 27 (1956).

[30] H. Bøggild *et al.*, Physics Letters B **302**, 510 (1993).

[31] D. H. Boal, C.-K. Gelbke, and B. K. Jennings, Rev. Mod. Phys. **62**, 553 (1990).

[32] J. Barrette *et al.*, Nuclear Physics A **610**, 227 (1996).

[33] M. Schubert *et al.*, Phys. Rev. Lett. **68**, 3016 (1992).

[34] M. Weber *et al.*, Phys. Rev. A **73**, 043406 (2006).

[35] M. Yasuda and F. Shimizu, Phys. Rev. Lett. **77**, 3090 (1996).

[36] M.-O. Mewes *et al.*, Phys. Rev. Lett. **78**, 582 (1997).

[37] D. Snoke, J. P. Wolfe, and A. Mysyrowicz, Phys. Rev. Lett. **59**, 827 (1987).

[38] C. Jurczak *et al.*, Phys. Rev. Lett. **77**, 1727 (1996).

[39] N. Lütkenhaus and S. M. Barnett, Phys. Rev. A **51**, 3340 (1995).

[40] G. S. Agarwal and K. Tara, Phys. Rev. A **43**, 492 (1991).

[41] L. Mandel, Opt. Lett. **4**, 205 (1979).

[42] J. Ivan, M. Kumar, and R. Simon, Quantum Information Processing **11**, 853 (2012).

[43] Y. Aharonov, D. Falkoff, E. Lerner, and H. Pendleton, Annals of Physics **39**, 498 (1966).

[44] M. S. Kim, W. Son, V. Bužek, and P. L. Knight, Phys. Rev. A **65**, 032323 (2002).

[45] R. Simon, Phys. Rev. Lett. **84**, 2726 (2000).

[46] J. Ivan, N. Mukunda, and R. Simon, Quantum Information Processing **11**, 873 (2012).

[47] P. Mehta, J. Samuel, and S. Sinha, Phys. Rev. A **82**, 034102 (2010).

[48] D. V. Strekalov, M. C. Stowe, M. V. Chekova, and J. P. Dowling, J. Mod. Opt. **49**, 2349 (2002).

[49] B. E. Saleh, A. F. Abouraddy, A. V. Sergienko, and M. C. Teich, Phys. Rev. A **62**, 043816 (2000).

[50] T. Pittmann, Y. Shih, D. Strekalov, and S. A.V., Phys. Rev. A **52**, R3429 (1995).

[51] H. Eisenberg, J. Hodelin, G. Khoury, and D. Bouwmeester, Phys. Rev. Lett. **94**, 090502 (2005).

[52] Y. Shih, *An Introduction to Quantum Optics : Photon and Biphoton Physics* (CRC Press (U.S.), Taylor & Francis, Boca Raton, FL, 2011).

[53] S. Bennick, R., J. Bentley, S., and W. Boyd, R., Phys. Rev. Lett. **89**, 113601 (2002).

[54] A. Abouraddy, B. Saleh, A. Sergienko, and M. Teich, Phys. Rev. Lett. **87**, 123602 (2001).

[55] B. E. A. Saleh and M. C. Teich, in *Advances in Information Optics and Photonics*, edited by A. T. Friberg and R. Dändliker (Society of Photo-Optical Instrumentation Engineers, Bellingham, Washington, USA, 2008), p. 423.

[56] B. I. Erkmen and J. H. Shapiro, Adv. in Optics and Photonics **2**, 405 (2010).

[57] D. Klyshko, Phys. Lett. A **146**, 93 (1990).

[58] V. Burlakov, A. *et al.*, Laser Phys. **12**, 1 (2002).

[59] Y. Shih, Rep. Prog. Phys. **66**, 1009 (2003).

[60] G. Scarcelli, A. Valencia, and Y. Shih, EPL **68**, 618 (2004).

[61] S. Karmakar, Y. Zhai, H. Chen, and Y. Shih, *Quantum Electronics and Laser Science Conference.* (Optical Society of America, Baltimore, Maryland United States, 2011), p. QFD3.

[62] P. Mehta, J. Samuel, and S. Sinha, Phys. Rev. A **82**, 034102 (2010).

[63] S. Pancharatnam, Proc. Ind. Acad. Sci. **A44**, 247 (1956).

[64] Y. Ben-Aryeh, Journal of Optics B: Quantum and Semiclassical Optics **6**, R1 (2004).

[65] P. Samuelsson, E. V. Sukhorukov, and M. Büttiker, Phys. Rev. Lett. **92**, 026805 (2004).

[66] I. Neder *et al.*, Nature **448**, 333 (2007).

[67] Y. Aharonov and D. Bohm, Phys. Rev. **115**, 485 (1959).

[68] R. G. Chambers, Phys. Rev. Lett. **5**, 3 (1960).

[69] M. Peshkin and H. J. Lipkin, Phys. Rev. Lett. **74**, 2847 (1995).

[70] M. Büttiker, Phys. Rev. Lett. **68**, 843 (1992).

[71] M. V. Berry, Proc. Roy. Soc. Lond. **A392**, 45 (1984).

[72] S. Ramaseshan and R. Nityananda, Curr. Sci. **55**, 1225 (1986).

[73] D. Pandey, N. Satapathy, M. S. Meena, and H. Ramachandran, Phys. Rev. A **84**, 042322 (2011).

[74] R. Loudon, American Journal of Physics **42**, 1041 (1974).

[75] G. Baym, Acta Physica Polonica B **29**, 1839 (1998).

[76] H. Paul, Reviews of Modern Physics **54**, 1061 (1982).

[77] A. Martin *et al.*, EPL (Europhysics Letters) **97**, 10003 (2012).

[78] J. Brendel, W. Dultz, and W. Martienssen, Phys. Rev. A **52**, 2551 (1995).

[79] T. Maiman, Nature**187**, 493 (1960).

[80] A. L. Schawlow and C. H. Townes, Phys. Rev. **112**, 1940 (1958).

[81] T. W. Hansch and A. L. Schawlow, Optics Communications **13**, 68 (1975).

[82] S. Chu *et al.*, Phys. Rev. Lett. **55**, 48 (1985).

[83] S. Chu, J. E. Bjorkholm, A. Ashkin, and A. Cable, Phys. Rev. Lett. **57**, 314 (1986).

[84] A. Ashkin, Phys. Rev. Lett. **24**, 156 (1970).

[85] E. L. Raab *et al.*, Phys. Rev. Lett. **59**, 2631 (1987).

[86] Y. Castin, H. Wallis, and J. Dalibard, J. Opt. Soc. Am. B **6**, 2046 (1989).

[87] P. D. Lett *et al.*, Phys. Rev. Lett. **61**, 169 (1988).

[88] J. Dalibard and C. Cohen-Tannoudji, J. Opt. Soc. Am. B **6**, 2023 (1989).

[89] P. J. Ungar, D. S. Weiss, E. Riis, and S. Chu, J. Opt. Soc. Am. B **6**, 2058 (1989).

[90] R. Grimm, M. Weidemuller, and Y. B. Ovchinnikov, Ad. At. Mol. Opt. Phys. **42**, 95 (1985).

[91] J. J. Sakurai and R. L. Liboff, American Journal of Physics **54**, 668 (1986).

[92] C. Cohen-Tannoudji, J. Dupont-Roc, G. Grynberg, and T. A. B. Kennedy, American Journal of Physics **61**, 572 (1993).

[93] S. J. M. Kuppens *et al.*, Phys. Rev. A **62**, 013406 (2000).

[94] N. Schlosser, G. Reymond, I. Protsenko, and P. Grangier, Nature**411**, 1024 (2001).

[95] C. Wieman, G. Flowers, and S. Gilbert, Am. J. Phys. **63**, 317 (1995).

[96] P. Kohns *et al.*, EPL (Europhysics Letters) **22**, 517 (1993).

[97] C. Wilson, Philos Trans. R. Soc. London **189**, 265 (1987).

[98] H. Dehmelt, Adv. At. Mol. Opt. Phys. **3**, 53 (1967).

[99] W. Neuhauser, M. Hohenstatt, P. Toschek, and H. Dehmelt, Phys. Rev. Lett. **41**, 233 (1978).

[100] S. Kuhr *et al.*, Science **293**, 278 (2001).

[101] Z. Hu and H. J. Kimble, Opt. Lett. **19**, 1888 (1994).

[102] D. Haubrich *et al.*, EPL (Europhysics Letters) **34**, 663 (1996).

[103] I. Dotsenko *et al.*, Phys. Rev. Lett. **95**, 033002 (2005).

[104] T. Wilk *et al.*, Phys. Rev. Lett. **104**, 010502 (2010).

[105] L. Isenhower *et al.*, Phys. Rev. Lett. **104**, 010503 (2010).

[106] Y. Miroshnychenko *et al.*, Phys. Rev. A **82**, 013405 (2010).

[107] M. Karski *et al.*, Science **325**, 174 (2009).

[108] Y. R. P. Sortais *et al.*, Phys. Rev. A **75**, 013406 (2007).

[109] A. Fuhrmanek, Y. R. P. Sortais, P. Grangier, and A. Browaeys, Phys. Rev. A **82**, 023623 (2010).

[110] A. Fuhrmanek *et al.*, New Journal of Physics **12**, 053028 (2010).

[111] W. Alt, Optik **113**, 142 (2002).

[112] M. K. Tey *et al.*, Nat Phys **4**, 924 (2008).

[113] S. A. Aljunid *et al.*, Phys. Rev. Lett. **103**, 153601 (2009).

[114] M. Weber *et al.*, Phys. Rev. A **73**, 043406 (2006).

[115] V. Gomer *et al.*, Phys. Rev. A **58**, R1657 (1998).

[116] D. Walls and G. J. Milburn, *Quantum Optics*, 2 ed. (Springer, New York, NY 10036, 2008).